Reference Interferometry Techniques for Nanodetection and Biosensing

by

Steven Herchak
B.Sc., University of Victoria, 2010

A Thesis Submitted in Partial Fulfillment of the
Requirements for the Degree of

MASTER OF APPLIED SCIENCE

in the Department of Electrical and Computer Engineering

Reference Interferometry Techniques for Nanodetection and Biosensing

by

Steven Herchak
B.Sc., University of Victoria, 2010

Supervisory Committee

Dr. Tao Lu, Supervisor
(Department of Electrical and Computer Engineering)

Dr. Wu-Sheng Lu, Departmental Member
(Department of Electrical and Computer Engineering)

Dr. Slim Ibrahim, Outside Member
(Department of Mathematics and Statistics)

Supervisory Committee

Dr. Tao Lu, Supervisor
(Department of Electrical and Computer Engineering)

Dr. Wu-Sheng Lu, Departmental Member
(Department of Electrical and Computer Engineering)

Dr. Slim Ibrahim, Outside Member
(Department of Mathematics and Statistics)

ABSTRACT

Three reference interferometry techniques which overcome the effects of laser jitter noise in sensitive nanodetection experiments are presented. Experiments performed with a Mach-Zehnder interferometer in parallel with an ultrahigh-Q microresonator for nanodetection of a record polystyrene particle size down to 12.5 nm radius are described. The first interferometry technique employed in this work sees the implementation of a Mach-Zehnder interferometer in parallel with a microsphere to show the versatility of these devices across detection systems. Using a least squares fitting method on simulated results, it is shown that the parallel Mach-Zehnder can detect resonant wavelength shifts of the microcavity down to hundreds of attometers, provided sufficient system stability. Furthermore, a cavity resonant wavelength shift detection sensitivity of 0.14 femtometers is observed experimentally with a loaded microsphere Q of 2.0×10^8 in a buffer solution.

For experiments which require high optical intensities, splitting off part of the optical power for use in an interferometer may reduce the dynamic range of power sensitive measurements. To rectify this problem, two in-line systems are investigated: the serial connected Mach-Zehnder and Fabry-Pérot interferometers. According to simulation, the use of a Mach-Zehnder interferometer is not suitable for serial interferometry. In light of this problem, a serial Fabry-Pérot interferometer is proposed. It is shown that with a least squares fitting method to fit experimental data the inline Fabry-Pérot interferometer can measure resonant wavelength shifts down to a few femtometers, again provided sufficient system stability. Experimental results show a cavity resonant wavelength shift detection sensitivity of 0.5 femtometers observed with a microsphere Q of 2.1×10^7 in a buffer solution.

Contents

List of Tables

List of Figures

List of Abbreviations

am	Attometers
BPD	Balanced photodetector
CCW	Counter-clockwise
CW	Clockwise
FC/APC	Fiber connector with angled physical contact
FC/PC	Fiber connector with physical contact
fm	Femtometers
FPI	Fabry-Pérot interferometer
FSR	Free spectral range
HWHM	Half width at half maximum
LSF	Least squares fit
MZI	Mach-Zehnder interferometer
PD	Photodetector
PSD	Power spectral density
Q	Quality factor
SPR	Surface plasmon resonance
WGM	Whispering gallery mode

ACKNOWLEDGEMENTS

I would like to thank:

My family, friends, and partner, for their support and confidence in me, making my education possible.

Professor Wu-Sheng Lu, for help with the least squares fitting.

My supervisor Tao Lu, and fellow students Xuan Du, Wenyan Yu,

Zhuang Zhuang (Jimmy) Tian and Amin Cheraghi Shirazi, for support, encouragement, patience, and friendship.

My friend Steph Dahl, for our trips to the Gulf Islands and help with the editing.

We are all inventors, each sailing out on a voyage of discovery, guided each by a private chart, of which there is no duplicate. The world is all gates, all opportunities.
Ralph Waldo Emerson

DEDICATION

I would like to dedicate my thesis to my family: Grandma, Grandpa, Mom, Dad, Aunt Verna and Nikki.

Chapter 1

Introduction

Nanodetection is an exciting technology with a plethora of important applications. In the emerging field of label-free nanodetection there are multiple techniques being investigated, including whispering-gallery mode (WGM) microcavities, surface plasmon resonance (SPR) devices and even combinations of the two [2–8]. Nanodetection devices are not limited to these techniques, however SPR and WGM topics are currently trending. These instruments have been used for the studies of individual nanoparticles and molecules [1, 8–29], including trapping, detection, and also sizing. With uses in the areas of biology, chemistry, as well as physics, it is of little wonder why these incredibly sensitive detectors are receiving an increased amount of attention. Here is a brief introduction on how WGM and SPR work with a list of some recent publishings, followed by motivation and an outline for the rest of this work.

WGM structures function through the coupling of an external light source, by means of an optical fiber taper [30–34], angle polished fiber [35, 36], prism [37, 38], or other device. The coupled light recirculates throughout the resonator many times before leaving the device [39]. By monitoring the effect the resonator has on the output transmission of the external light source, there exists the possibility for the detection of minute changes in the resonant wavelength of the microcavity. This change in wavelength is due to a change in the index of refraction of the surrounding media, corresponding to the binding events of nanoparticles. Recent work in this field includes measuring thermal deformation in microelectromechanical systems with microdiscs [40], probing microspheres with a dual comb interferometry set-up for sensing [41], theory of nanoparticle sensing with WGM resonators for both plasmonic and Rayleigh scatterers [42], and single virus detection with both microspheres [43] and microtoroids [1].

One way SPR can be used to detect molecular adsorption is by reflecting light off of a metal to dielectric interface and noting the angle at which the occurrence of surface plasmons is at a maximum [44]. A change in this angle occurs due to the change of the local refractive index at the dielectric interface corresponding to the molecular adsorption. By monitoring this adsorption it is possible to quantize reaction rates, and also to monitor reactivity between molecules. Recent work in this field includes research on receptor-ligand interaction [45], triangular silver nanoparticle detection [46], the limits of SPR sensors [47], the imaging of local electrochemical current [48], increasing detection sensitivity by using a chalcogenide prism [49], the use of long range surface plasmons [50], detecting early stage prostate cancer [29], and detection of non-absorbing molecules [28].

It has been claimed that due to optical recirculation the sensitivities of WGM resonators will exceed those obtained with SPR methods [51]. Much work in the form of optimization of fabrication techniques has gone into enhancing the quality factor (Q), the figure of merit for microresonators. A common element to all WGM devices is a rotational axis of symmetry, as the operating principle requires light to circulate through the structure many times. For example, the types of WGM geometries being researched are rings, disks, toroids, spheres, pillars, capillaries, and bottles [18, 52–56]. The structure that provides the highest Q-factor in water (a convenient medium for detection) is the microtoroid, with values reported well above 10^8 [1]. However, even with a large enough Q, known to define how well the microcavity will work, there is another limitation to the sensitivity: the noise in which each measurement is made. This noise may be internal due to the equipment, or externally from the environment. Regardless of where the noise comes from, it must be reduced in order resolve the small (fractions of a femtometer for 12.5 nm radii particles [1]) changes to the resonant wavelength of microcavities.

The work of this thesis is to build upon the parallel interferometry technique used in [1] by showing its versatility with a different microcavity system. Furthermore, this work introduces two types of in-line (to be referred to as serial) interferometry techniques that can also be utilised in order to reduce the effects of noise from both the experimental environment and equipment to make nanodetection experiments more sensitive. The two interferometers used are known as Mach-Zehnder and Fabry-Pérot interferometers (MZI and FPI respectively). The MZI works by splitting light into two paths with a differential phase delay, and then recombining the light to exhibit interference. The FPI works by reflecting light through a cavity, which causes the transmission to be a superposition of light waves which have travelled a different optical path length. As the name nanodetection implies, all measurements are on the nanometer scale and at this scale even dust or vibrations that cannot be seen with the human eye will have an effect on the results. The effect of decreasing the effects of the noise of the system will allow for enhanced signal to noise ratio, and hence an increase in the sensitivity of WGM based nanodetection.

1.1 Thesis Framework

Chapter Two establishes an understanding of concepts relevant to both microresonant structures and nanodetection. It introduces both methods of nanodetection with and without the use of an interferometer to reduce the effects of laser jitter. Furthermore, the approach used to fabricate the structures utilised in this work will be outlined, and a brief description of least squares fitting (LSF) follows. This chapter serves to develop motivation, and introduce terminology for the devices and methods described in the remaining chapters.

Chapter Three is devoted to the theory behind optical coupling, and interferometry. It begins by developing the equations pertaining to a system consisting of a fiber optic line coupled to a microcavity by means of an optical fiber taper. The next two sections cover the theory for both types of interferometers, MZI, and FPI. An interferometer is a device which uses the superposition of light to produce a meaningful output. In this case the optical signals from the interferometer serve as a reference to distinguish between microcavity wavelength shifts under a noisy environment caused by laser jitter.

Chapter Four explains how the free spectral ranges, the characterizing parameter of the interferometers, are obtained. It begins by introducing the power spectral density of the interferometer noise components, and the method of determining the free spectral range is shown graphically with an experimentally obtained data trace. The processed results of an experiment are both displayed, and used to characterize the MZI and FPI used in this work.

Chapter Five is about parallel interferometry. It begins by detailing the first nanodetection experiment to use a reference interferometer, found in [1], which happened to be a MZI in parallel with a microtoroid. Both the experiment and its results are detailed. In the second section it will be shown that the reference interferometry method is versatile by employing a parallel MZI with the use of a microsphere to detect resonant wavelength shifts. The parallel MZI is simulated and LSFs are performed on simulated data to determine its performance. In order to prevent a large amount of manual calculations, these fits are to be performed on the experimental data. This is very important because to successfully monitor the shifts of the resonant wavelength, the transmission spectrum must be sampled thousands of times. Finally experimental results are presented, followed by a discussion.

Chapter Six further advances the applications of a reference interferometer by introducing the idea of a serial connection. The first section starts by describing the experimental set-up for a serial MZI. Then, simulation and LSF equations are developed and used with each other to find the limitations of the LSF. In this section we will see that the serial MZI will cause a loss of data, which will subsequently result in a larger error in the fitted wavelength shift. This motivates the need of an interferometer with a transmission spectrum that does not go to zero, a condition which is fulfilled by the FPI. The experimental set-up is described for a serial FPI system, simulation and LSF equations are developed and the results are displayed. Finally experimental results are included, and a discussion of the performance of the serial FPI versus both configurations of the MZI is covered.

Chapter Seven summarizes all the methods covered and their results. Lastly there will be a discussion on methods of improvement and possible future initiatives including cascaded interferometers for possible detection of different particle sizes.

Chapter 2

Background and Motivation

When it comes to detecting the presence of single nanoparticles or molecules there is a push for the achievement of smaller and smaller detection sizes. However, as is easy to imagine, there is a limit to the detection size inherent to every detection apparatus. This limit may be a result of sources of noise including but not limited to electro-mechanical conversions, mechanical vibrations and thermal instabilities either created by, or intrinsic to, the experimental equipment. If the apparatus is operating with sufficiently low noise, there exists a more fundamental and final limit to detection determined by the physical properties of the detector, in this case a microcavity. In this chapter the background of the physical properties of microcavities will be covered, along with an introduction to nanosensing techniques, fabrication of nanodetection equipment, and LSF techniques which will be used later in this work for simulation and data processing.

2.1 Microcavities

One method for single nanoparticle detection is to take advantage of microscale axi-symmetric structures known as microcavities for their optical WGM [57, 58]. Whispering-gallery structures confine light at specific resonant wavelengths about their circular perimeter, and this light propagates around the boundary recirculating many times through the process of total internal reflection [59]. The figures of merit for a WGM microresonator are the Q-factor and mode volume. The Q-factor is a measure of temporal confinement of the light propagating in WGMs and is directly related to the ratio of the energy stored to energy dissipated per resonant cycle. The expression for Q is written

$$Q = 2\pi \frac{Energy\, stored}{Energy\, dissipated\, per\, cycle} = \frac{\nu_R}{\Delta\nu} = 2\pi\nu_R\tau_L \tag{2.1}$$

where ν_R is the resonant frequency, $\Delta\nu = \frac{1}{2\pi\tau_L}$ is the resonant linewidth, and τ_L is the photon lifetime. For a typical microsphere of 100μm and Q of 10^8 at a resonant wavelength of 635nm, the photon lifetime is 33.7 ns. To put this into perspective, this translates to roughly a photon travel distance of 6.74 meters, or 21,446 trips around the microsphere.

The mode volume, V_{eff} is a measure of spatial confinement of the light propagating in WGMs and is defined as [60]:

$$V_{eff} = \frac{\int_V \epsilon(\mathbf{r})|\mathbf{E}(\mathbf{r})|^2 \, \mathrm{d}^3\mathbf{r}}{max[\epsilon(\mathbf{r})|\mathbf{E}(\mathbf{r})|^2]}. \tag{2.2}$$

Where $\epsilon(\mathbf{r})$ is the dielectric constant, $\mathbf{E}(\mathbf{r})$ is the optical field, and V is a volume sufficient to contain all the optical field of light travelling in a WGM.

2.2 Nanodetection

The resonant wavelengths that travel around the microcavity are extremely sensitive to things like the microcavity size, as well as index of refraction, both of which change with temperature. This sensitivity to index of refraction is the property exploited to detect the presence of nanoparticles that have attached to the surface of the microresonator. To reiterate, the presence of a nanoparticle modifies the optical properties of the microresonator, resulting in an observable change to the resonant wavelength (see Appendix A for the derivation). This wavelength shift can be obtained from the frequency shift, denoted α, given by Equation 2.3, where ω_0 is the central frequency, $\delta\epsilon_r(\vec{r})$ is the perturbing permittivity, $\epsilon_r^0(\vec{r})$ is the bulk permittivity, and $\vec{e_\pm}(\vec{r})$ is the mode profile of the clockwise (CW) or counter-clockwise (CCW) modes [61].

$$\alpha = \frac{\omega_0}{2} \frac{\int \delta\epsilon_r(\vec{r})|\vec{e_\pm}(\vec{r})|^2 \, \mathrm{d}V}{\int \epsilon_r^0(\vec{r})|\vec{e_\pm}(\vec{r})|^2 \, \mathrm{d}V}. \tag{2.3}$$

The fundamental size of particle that can be detected by the microcavity is limited by the optimum resolution between resonant wavelength shifts, which is determined by the Q-factor of the microcavity [52]. Currently crystalline CaF_2 resonators can be made to have Q above the order of 10^{10} [62]. With such a high Q other sources of noise come to dominate, mainly the instability caused by the laser used to feed light to the microcavity [63, 64]. The dominant instability (to be referred to as laser jitter) may be a result of intrinsic laser noise, error in conversion of modulation voltage to frequency, and inaccuracies in the mechanical scanning mechanisms [65]. Intrinsic frequency jitter typically arises from fluctuations in the length of the laser cavity, namely: mechanical vibrations and thermal expansion. Even lasers with high frequency purity experience jitter due to the quantum noise fluctuations caused by spontaneous emission of photons by atoms in the active laser medium [65]. These quantum fluctuations are described by the Schawlow-Townes formula [66], and more detail into semi-conductor laser noise statistics is achieved by considering Langevin forces, as in [67, 68]. Further analysis of optical frequency noise in fiber-optic systems can be found in [69].

There are three different methods that have been used to overcome this laser jitter noise. The first method is to use a laser that has low frequency noise, as was accomplished with a modified distributed feedback laser [14]. The second method is to monitor the shifts of the relative separation between the split frequencies induced by mode coupling [1, 27, 61], denoted β, as given in Equation 2.4 (see Appendix A for derivation).

$$\beta = \frac{\omega_0}{2} \frac{\int \delta\epsilon_r(\vec{r}) \vec{e_+}(\vec{r}) \vec{e_-}(\vec{r})^* \, \mathrm{d}V}{\int \epsilon_r^0(\vec{r}) |\vec{e_-}(\vec{r})|^2 \, \mathrm{d}V} \tag{2.4}$$

Here ω_0 is the central frequency, $\delta\epsilon_r(\vec{r})$ is the perturbing permittivity, $\epsilon_r^0(\vec{r})$ is the bulk permittivity, $\vec{e_+}(\vec{r})$ is the mode profile of the clockwise mode, and $\vec{e_-}(\vec{r})$ is the mode profile of the CCW mode. This effectively cancels out any laser jitter, as has been demonstrated [14].

The third method, and the one focused on in this work, is to develop a reference system that follows the noise of the laser so that one knows when a wavelength shift has truly been caused by the binding event of a nanoparticle, and not the laser jitter. This has been achieved with what has come to be called a reference interferometer [1]. Interferometry is a technique which utilizes the wave nature of light by superimposing two or more separate instances to create a new instance that is dependent on the amount of interference that takes place between the original sources. This same technique which was famously used to detect the now debunked “ether wind” [70] is also used to increase the angular resolution of telescopes looking at astral bodies [71], and now even finds use in the area of nanodetection.

2.2.1 The Conventional Method for Measuring Resonant Wavelength Shifts

The conventional method for determining resonant wavelength shifts due to nanoparticle binding events as seen in [20], is as follows. It is noted that this method uses no techniques to minimize or correct for the laser jitter noise. First the voltage of the laser's scanning waveform is obtained at the location of the microcavity's resonant dip (V_R, in units of volts). This voltage is then converted to a frequency value by multiplying it by the voltage scan rate, $S_{\nu V}$, in units of Hertz per volt. The scan rate of the laser (S_ν with units of Hertz per second) can be obtained from parameters given in the specifications of the laser being used, and this scan rate can be converted to the voltage scan rate by simply dividing it by the slope of the scanning waveform (m_{SWF} with units of Volts per second):

$$S_{\nu V} = \frac{S_\nu}{m_{SWF}}. \tag{2.5}$$

So that the change in resonant wavelength location is given by:

$$\Delta\lambda_R = -\frac{\lambda_R^2}{c}\Delta\nu_R = -\frac{\lambda_R^2}{c}S_{\nu V}\Delta V_R. \tag{2.6}$$

The process of determining change in resonant wavelength by monitoring a change of the voltage at the resonant dip is illustrated in Figure 2.1.

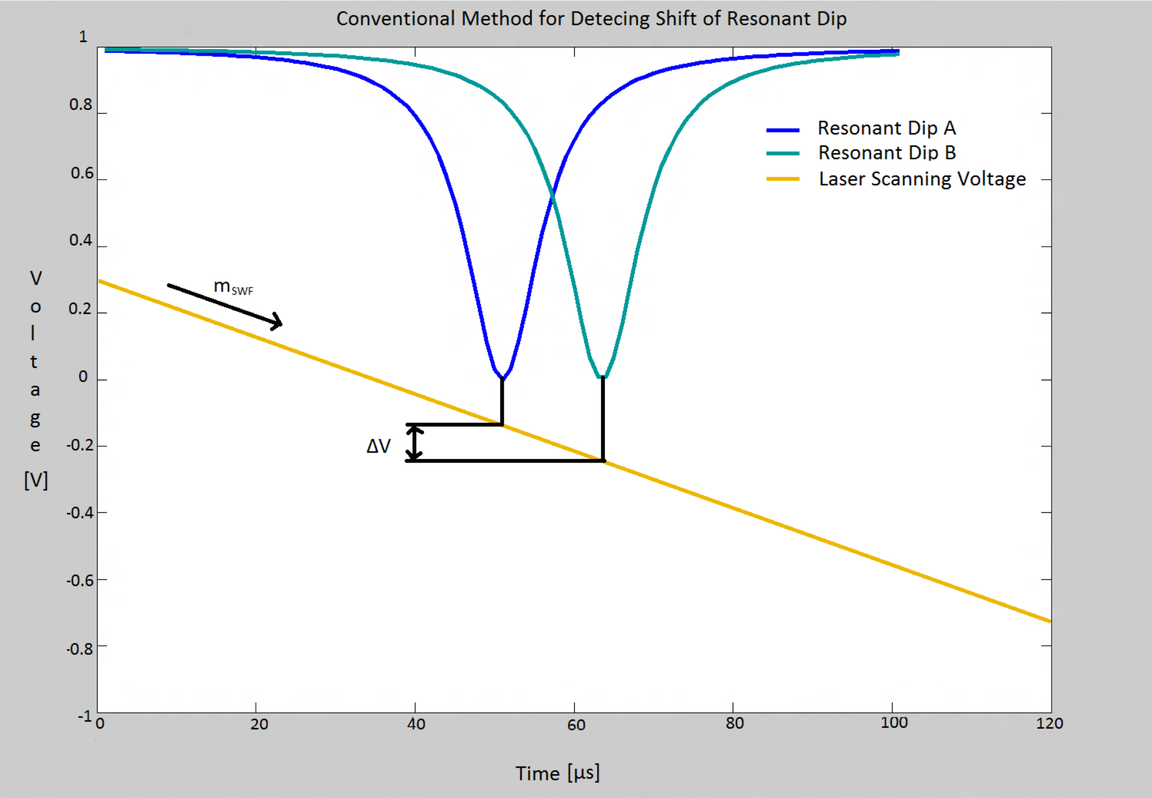

Figure 2.1: Overview of the conventional method for determining shift of resonant wavelength.

2.2.2 The Interferometer Method for Measuring Resonant Wavelength Shifts

The interferometer method for determining resonant wavelength shifts due to nanoparticle binding events as seen in [1], is as follows. The time difference between the sequential locations of the resonant dips is calculated, using the interferometer as a reference. Using this method, the effects of laser jitter are cancelled because both the reference interferometer signal and resonant dip will jitter together. This time difference is then converted to a frequency value by multiplying it by the voltage scan rate, S_ν, in units of Hertz per second. The scan rate of the laser, S_ν can be obtained from parameters given in the specifications of the laser being used. The change in resonant wavelength location can be obtained from the change in the resonant frequency, which is described by:

$$\Delta\lambda_R = -\frac{\lambda_R^2}{c}\Delta\nu_R = -\frac{\lambda_R^2}{c}S_\nu\Delta t. \tag{2.7}$$

This process is illustrated in Figure 2.2.

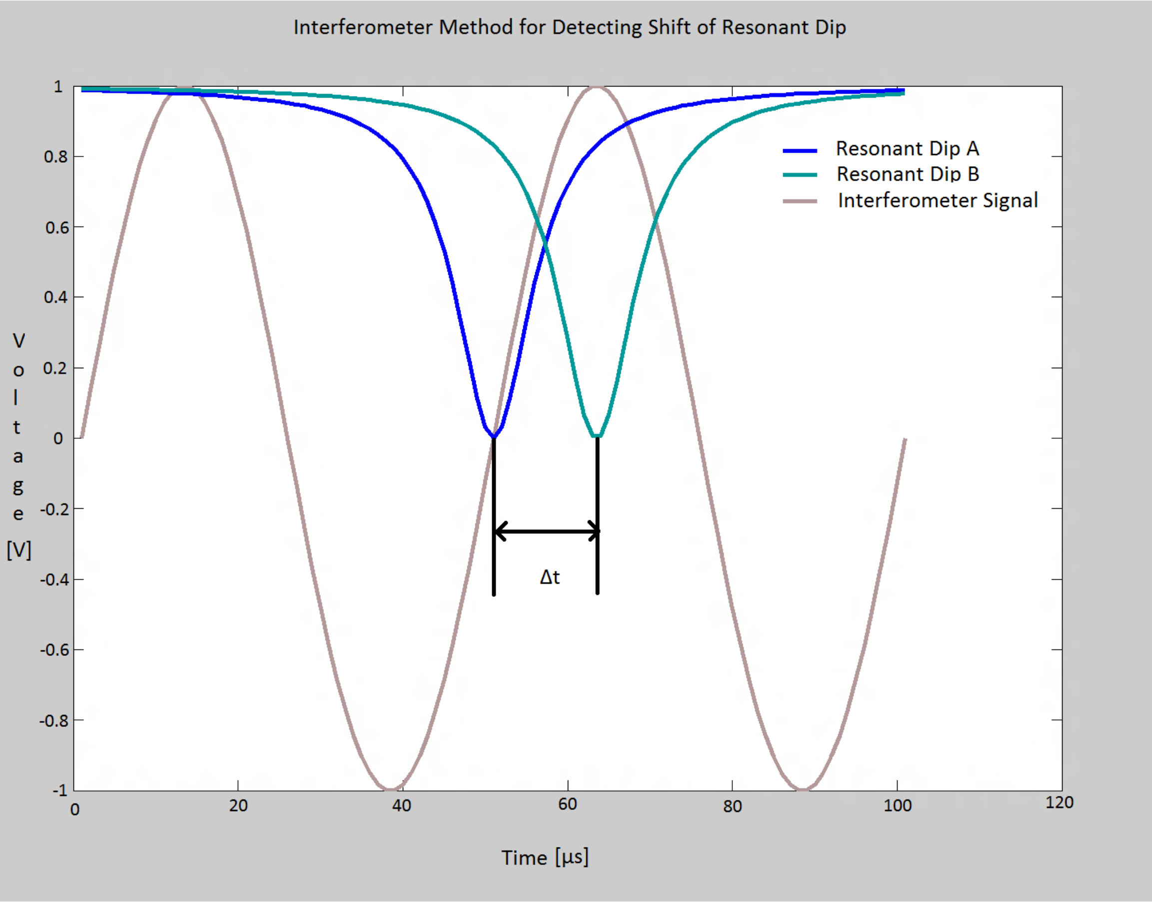

Figure 2.2: Overview of the interferometer method for determining shift of resonant wavelength.

2.3 Fabrication Techniques of Nanodetection Equipment

In this section the fabrication process for equipment made in-house will be covered. This includes fabrication of fiber tapers, and microspheres. A micrograph of a microsphere coupled to a optical fiber taper is shown in Figure 2.3.

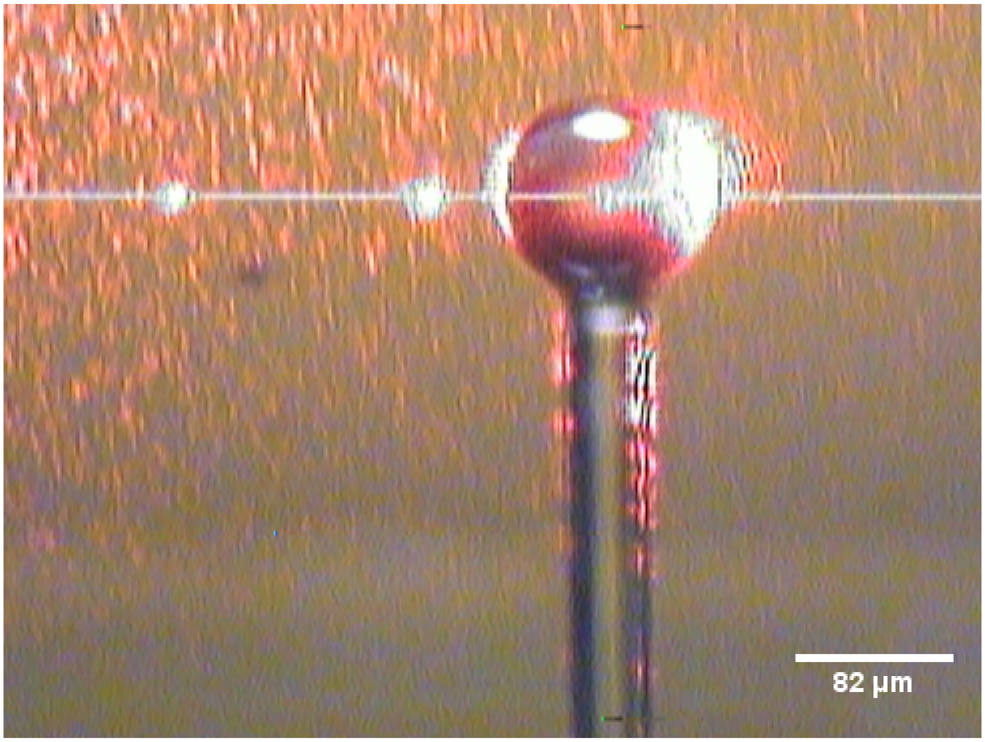

Figure 2.3: Micrograph of a fiber optical taper coupled to a microsphere.

2.3.1 Optical Fiber Taper

A tapered fiber optic cable used for the coupling of light to a microcavity is a delicate piece of apparatus, with the smallest fiber diameter approaching just microns in diameter [72]. At such a small diameter the fiber taper is extremely fragile and is even sensitive to air currents and dust particles landing on it. The fiber taper is made in-house using two stepper motors to pull a jacket-removed optical fiber suspended over a hydrogen torch. The set-up used in this work is shown in Figure 2.4. If this process is done while monitoring laser power through the fiber, one can observe the transmitted signal develop a sinusoidal signal of increasing frequency. This occurs because as the fiber is stretched into a taper the change in fiber diameter results in a loss of the conditions required to maintain single-mode [73]. While the fiber is multi-mode the superposition of the extra modes with the fundamental mode results in interference, and as the distribution of power in the various modes change this manifests as oscillation of the photodetected power. As the fiber is stretched further the frequency of interference increases until the taper is once again single-mode, a condition required for effective coupling to the microcavity.

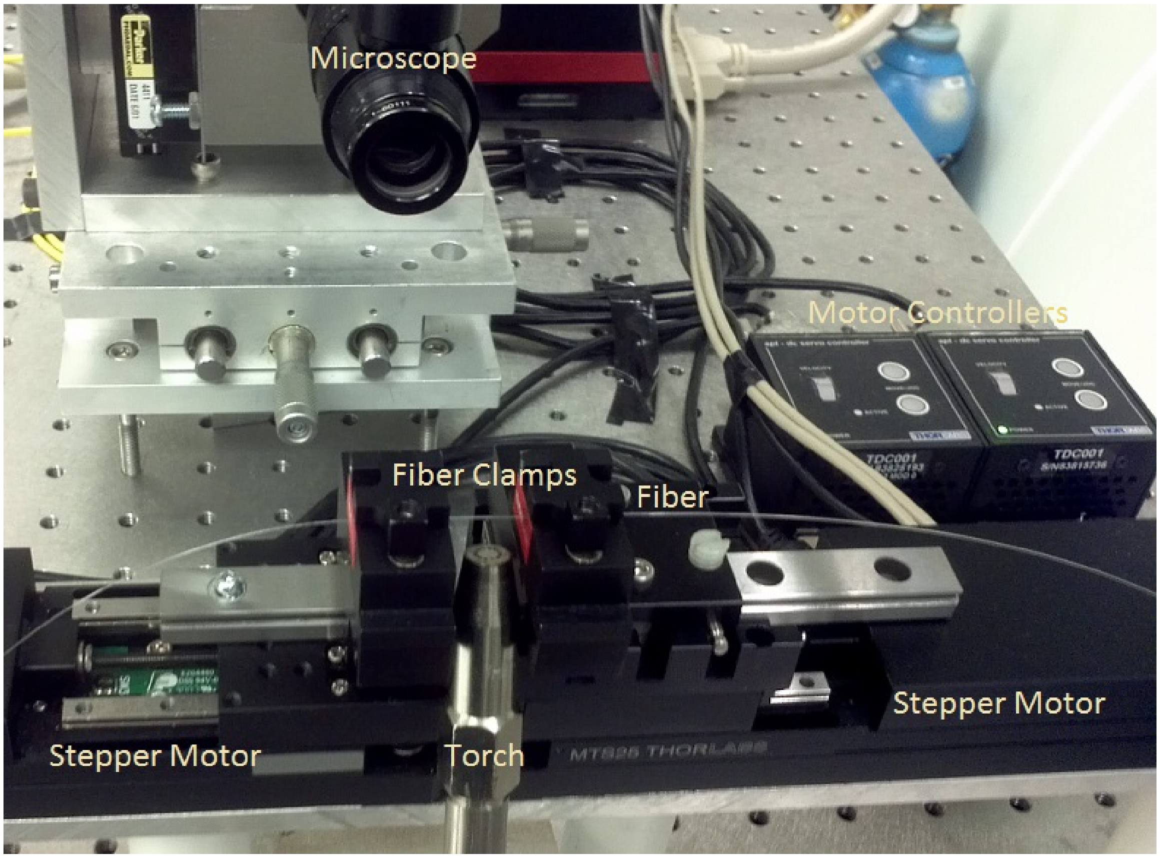

Figure 2.4: Set-up of the fiber pulling system.

2.3.2 Optical Fiber Based Microsphere

For the experiments performed in this work a spherical shaped microcavity known as a microsphere is used. The fabrication process for a microsphere requires only a few pieces of equipment: a high power laser operating at a wavelength that is absorbed by fused silica, and a beam focusing set-up. The process involved in creating the spherical shape requires the pulse of a CO_2 laser focused to effectively melt or reflow the tip of a jacket-removed optical fiber. The surface tension of the liquid silica causes the droplet to take on a spherical shape and it cools very rapidly (in a matter of seconds). Typical microspheres used in this work had an intrinsic Q between 1 and 3×10^8 in air at a wavelength of 635 nm.

2.4 Least Squares Fitting

Here, a LSF is implemented to determine the resonant wavelength for all data traces obtained. The method of least squares is a fitting algorithm, credited to Gauss, which minimizes the squares of the residuals (the difference between a fitted point and the data value at that point). The method uses a modelling function with unknown coefficients supplied with or without a guess for the coefficients. The algorithm can be used for solving both linear and non-linear functions, and in this work only non-linear equations are considered. In the case of non-linear equations an initial guess is used and then the algorithm iteratively refines the fitting coefficients. This is done by finding adjustments to all the coefficients which satisfy a gradient equation to minimize the residuals. The interested reader can learn more from [74].

Chapter 3

Relevant Theoretical Concepts

In order to understand how interferometers can be used to increase the sensitivity of WGM based microcavities, both the concepts of optical coupling to the microcavity, and interferometry must be understood. This chapter is devoted to the theoretical concepts relevant to this work. The topic of light transmission through an optical fiber coupled to a microcavity, and the theory of both Mach-Zehnder and Fabry-Pérot interferometers will be covered. In order to simplify the theory throughout this thesis, the electric fields, $\vec{E}_i(\vec{r},t) = E_i(t)\vec{e}_i(\vec{r})$, will be written in terms of their amplitudes, $E_i(t)$, which are normalized such that $P_i(t) = |\vec{E}_i(\vec{r},t)|^2$.

3.1 Transmission of Light through an Optical Fiber Coupled to a Microcavity

Following the theory in [75], light is coupled from an optical fiber both into and out of a microresonator. At a time t, the circulating light in the microresonator is a sum of the light that is coupled into the resonator and the light that remains from previous coupling. Denote the incoming light from the waveguide as E_{in}, the outgoing light as E_{out}, the resonator circulating light as E_c, and the transmission and reflection coefficients from the waveguide to the resonator as t_E and r_E respectively. This is displayed in Figure 3.1. Let it subsequently be known that this theory is greatly simplified because it is justly assumed that the incoming light is single-mode, and therefore multiple modes do not need to be distinguished.

In mathematical terms we can describe the circulating light of wavelength λ in

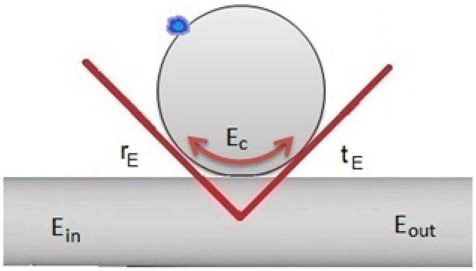

Figure 3.1: Coupling of light from a fiber taper to microresonator.

the resonator as

$$E_c(t) = jt_E E_{in}(t) + r_E E_c(t - \tau_0) e^{\left(\frac{j2\pi n_s L}{\lambda} - \frac{\alpha L}{2}\right)}. \tag{3.1}$$

Here $\tau_0 = \frac{n_s L}{c}$ is the time for one circulation around the resonator of path length L, material loss is denoted by α, n_s is refractive index, and speed of light is c. The output light of the waveguide is given as

$$E_{out}(t) = r_E E_{in}(t) + jt_E E_c(t). \tag{3.2}$$

Using $E_c(t - \tau_0) = E_c(t) - \tau_0 \frac{dE_c}{dt}$ while noting $\omega_0 = \frac{2\pi}{\tau_0}$ and $n_s L = m\lambda_R$ where m is an integer, and λ_R is the resonant wavelength, one can arrive at the following equation by substituting into Equation 3.1:

$$\frac{dE_c}{dt} + \left(\frac{\alpha c}{2n_s} + \frac{1 - r_E}{r_E \tau_0} + j\Delta\omega\right) E_c = j\frac{t_E E_{in}(t)}{\tau_0}. \tag{3.3}$$

Here $\Delta\omega$ describes the difference between the incoming light's frequency, and the resonant frequency of the cavity. The steady state of this equation is

$$E_c(t) = j\frac{t_E}{\tau_0}\frac{E_{in}(t)}{\delta_0 + \delta_c + j\Delta\omega}, \tag{3.4}$$

where it is defined that $\delta_0 = \frac{\alpha c}{2n_s}$ is the internal loss parameter and $\delta_c = \frac{t_E^2}{2\tau_0}$ is the coupling loss parameter. For clarity it is noted that this equation isn't truly steady state, as it depends on the time varying input electric field. The equation is referred to as steady state because the cavity electric field reaches equilibrium in a time much shorter than the timescale on which the input electric field changes.

Substituting the steady state solution, Equation 3.4 back into Equation 3.2 yields the following (it is noted here that $r_E = 1 - t_E^2/2 \approx 1$):

$$E_{out}(t) = E_{in}(t)\left(1 - \frac{2\delta_c}{\delta_0 + \delta_c + j\Delta\omega}\right). \tag{3.5}$$

To get the output power from the waveguide, the magnitude square of E_{out} is the desired quantity. After multiplying E_{out} with its complex conjugate and then proceeding to manipulate the terms one can arrive at the following result:

$$P_{out} = P_{in}\frac{(\delta_0 - \delta_c)^2 + \Delta\omega^2}{(\delta_0 + \delta_c)^2 + \Delta\omega^2}. \tag{3.6}$$

This equation describes the output power in terms of the original input power, and how the frequency of the laser light relative to the resonant frequency of the resonator affects the amplitude. Upon investigation, one finds that the transmission as a function of laser frequency exhibits a Lorentzian style curve. It is insightful to express the loss parameters in terms of their associated quality factors where $Q_i = \frac{\omega}{2\delta_i}$. In terms of the coupling parameter $K = \frac{Q_0}{Q_c}$, input optical power $P_{in}(t)$, laser frequency ν_L, and resonant frequency ν_R the output power of a coupled microcavity becomes

$$P_{out}(t) = P_{in}(t)\left(1 - \frac{4K}{(1+K)^2 + \frac{2Q_0}{\nu_L^2}(\nu_R - \nu_L)^2}\right). \tag{3.7}$$

3.2 The Mach-Zehnder Interferometer

The first interferometer to be analyzed is a typical MZI [76, 77] consisting of a 3-dB coupler which splits the signal and sends it through two separate optical lines with a differential phase delay of $\Delta\varphi$. The signal is then recombined at another 3-dB coupler from where it is sent to a balanced photodetector. The overall scheme of this interferometer can be seen in Figure 3.2.

To obtain the transmission equation, the scattering matrix method is invoked. With this method one must simply multiply the scattering matrices of each component of the optical system. The scattering matrix for a 3-dB coupler is

$$M_{3-dBcoupler} = \frac{1}{\sqrt{2}}\begin{bmatrix} 1 & j \\ j & 1 \end{bmatrix}. \tag{3.8}$$

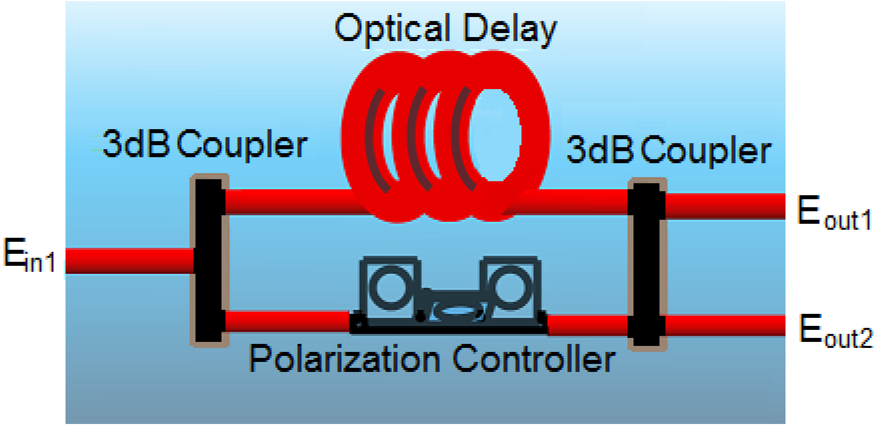

Figure 3.2: MZI configuration. Image included and subsequently modified from [1] with permission from Tao Lu and Xuan Du.

The scattering matrix for a differential phase delay line of refractive index n_s and length ΔL is

$$M_{\Delta\varphi} = \begin{bmatrix} e^{j\frac{\pi\nu_L n_s \Delta L}{c}} & 0 \\ 0 & e^{-j\frac{\pi\nu_L n_s \Delta L}{c}} \end{bmatrix}. \tag{3.9}$$

The output electric field from the interferometer is given by the following equation:

$$\begin{bmatrix} \mathbf{E}_{out1} \\ \mathbf{E}_{out2} \end{bmatrix} = M_{3-dBcoupler} M_{\Delta\varphi} M_{3-dBcoupler} \begin{bmatrix} \mathbf{E}_{in1} \\ \mathbf{E}_{in2} \end{bmatrix}. \tag{3.10}$$

Upon substitution of the defined matrices, Equations 3.8 and 3.9, the output electric field can be written as

$$\begin{bmatrix} \mathbf{E}_{out1} \\ \mathbf{E}_{out2} \end{bmatrix} = \frac{1}{2} \begin{bmatrix} 1 & j \\ j & 1 \end{bmatrix} \begin{bmatrix} e^{j\frac{\pi\nu_L n_s \Delta L}{c}} & 0 \\ 0 & e^{-j\frac{\pi\nu_L n_s \Delta L}{c}} \end{bmatrix} \begin{bmatrix} 1 & j \\ j & 1 \end{bmatrix} \begin{bmatrix} \mathbf{E}_{in1} \\ \mathbf{E}_{in2} \end{bmatrix}. \tag{3.11}$$

When expanded and simplified, it is found that the output electric fields of the interferometer system is given by

$$\begin{bmatrix} \mathbf{E}_{out1} \\ \mathbf{E}_{out2} \end{bmatrix} = j \begin{bmatrix} sin\left(\frac{\pi\nu_L n_s \Delta L}{c}\right) & cos\left(\frac{\pi\nu_L n_s \Delta L}{c}\right) \\ cos\left(\frac{\pi\nu_L n_s \Delta L}{c}\right) & -sin\left(\frac{\pi\nu_L n_s \Delta L}{c}\right) \end{bmatrix} \begin{bmatrix} \mathbf{E}_{in1} \\ \mathbf{E}_{in2} \end{bmatrix}. \tag{3.12}$$

For experiments with a single input, $\mathbf{E}_{in2}$ is zero, and the following result is obtained:

$$\mathbf{E}_{out1} = j\mathbf{E}_{in1} sin\left(\frac{\pi\nu_L n_s \Delta L}{c}\right)$$
$$\mathbf{E}_{out2} = j\mathbf{E}_{in1} cos\left(\frac{\pi\nu_L n_s \Delta L}{c}\right). \tag{3.13}$$

To make this equation useful, it must be written in terms of the optical power. As was mentioned, the electric field amplitudes are normalized such that $P_j(t) = |\vec{E}_j(\vec{r}, t)|^2$. Hence the output power of the two ports of the MZI is given by the following:

$$P_{out1} = P_{in1} sin^2\left(\frac{\pi\nu_L}{\Delta\nu_{FSR}}\right)$$
$$P_{out2} = P_{in1} cos^2\left(\frac{\pi\nu_L}{\Delta\nu_{FSR}}\right) \tag{3.14}$$

Where

$$\Delta\nu_{FSR} = \frac{c}{n_s \Delta L} \tag{3.15}$$

is the free spectral range (FSR) of this interferometer, defined as the separation between two successive peaks of transmitted intensity. Here it is found that the output power of the interferometer is proportional to the input power, and the two out of phase outputs vary with laser frequency in the form of sinusoids.

3.3 The Fabry-Pérot Interferometer

A FPI consists simply of a cavity where light is reflected between two interfaces repeatedly, as depicted in Figure 3.3. For illustrative purposes the light is shown to enter the cavity at an angle with a slight deviation from the normal.

To derive the transmission equations and FSR of such a cavity, first consider what happens as light encounters both the air to silica, and silica to air interfaces. For simplification of the math this work will deal with the light traveling at normal incidence, which is justified because the experiment is dealing only with the fundamental mode. Let the transmission of the first wave through the first interface of the Fabry Pérot cavity be denoted as $t_E E_{in}$ and the reflected light as $r_E E_{in}$, where t_E and r_E are the electric field amplitudes of transmission and reflection from air to silica, respectively.

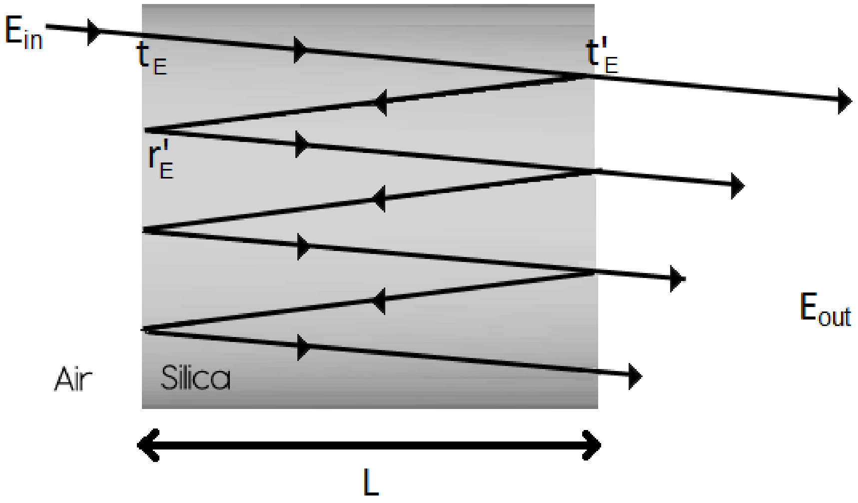

Figure 3.3: Serial FPI configuration.

Furthermore, the amplitudes of transmission and reflection for the silica to air interface will be denoted as t'_E and r'_E, respectively. The output through the cavity can be expressed as an infinite sum starting with the light that is transmitted by the first interface, attains a phase of δ (defined below), and is transmitted through the second interface. Each subsequent term of the expansion includes an additional phase of $e^{j2\delta}$ and two reflections, r'^2_E. The first transmitted light is given by $t_E t'_E E_{in} e^{j\delta}$, and the second is given by $t_E t'_E E_{in} e^{j\delta}(r'^2_E e^{2j\delta})$. A formula for the n^{th} transmitted beam is then $t_E t'_E E_{in} e^{j\delta}(r'^2_E e^{2j\delta})^n$. The total transmission of the waves through the cavity is given by the following geometric series:

$$E_{out} = t_E t'_E E_{in} e^{j\delta} \sum_{n=0}^{\infty} (r'^2_E e^{2j\delta})^n. \tag{3.16}$$

The closed form solution is, because $|r'^2_E e^{2j\delta}|$ is strictly less than one, give by:

$$E_{out} = \frac{t_E t'_E E_{in} e^{j\delta}}{1 - r'^2_E e^{2j\delta}}. \tag{3.17}$$

Where δ, the additional phase attained by light travelling through the Fabry-Pérot cavity of length L and refractive index n_s is defined as

$$\delta = \frac{2\pi \nu_L}{c} n_s L. \tag{3.18}$$

The output power transmission is obtained by multiplying the output electric field by its complex conjugate. The result is simplified as follows:

$$\begin{aligned} P_{out} &= E_{out}E^{*}_{out} = \frac{P_{in}|t_E|^2|t'_E|^2}{(1-|r'_E|^2e^{2j(\delta+\phi_{r'})})(1-|r'_E|^2e^{-2j(\delta+\phi_{r'})})} \\ &= \frac{P_{in}|t_E|^2|t'_E|^2}{(1-|r'_E|^2)^2+4|r'_E|^2sin^2(\delta+\phi_{r'})}. \end{aligned} \tag{3.19}$$

Here $\phi_{r'}$ is the phase of the reflection coefficient from the silica to air interface.

If the power reflectivity is defined as $R = R' = |r'_E|^2$, and the materials are approximated as optically lossless, $|r_E|^2+|t_E|^2 = |r'_E|^2+|t'_E|^2 = 1$, the above equation can be simplified to

$$P_{out} = \frac{P_{in}(1-R)^2}{(1-R)^2+4Rsin^2(\delta+\phi_{r'})} = \frac{P_{in}}{1+Fsin^2(\frac{\pi\nu_L}{\Delta\nu_{FSR}}+\phi_{r'})}, \tag{3.20}$$

where

$$F = \frac{4R}{(1-R)^2} \tag{3.21}$$

is the coefficient of finesse, and $\Delta\nu_{FSR}$ is the FSR of the FPI. Due to the functional form of the FPI transmission, the FSR is half of the oscillation period of the sinusoidal term, given by the following formula:

$$\Delta\nu_{FSR} = \frac{c}{2n_sL}. \tag{3.22}$$

Here it is seen that the output power (dependent on input laser frequency) is governed by an Airy function, whose characteristics are completely governed by both the power reflectivity between interfaces of the cavity, and the FSR which is dependent on the optical path length of the laser.

Chapter 4

Free Spectral Range Determination

4.1 Power Spectral Method of Free Spectral Range Determination

To determine the FSR of the MZI and FPI used in this work the periods of these interferometers were directly compared to the period of a third interferometer whose FSR was already determined. The interferometer which is used as a reference is a MZI, and by using a balanced photodetector and a real time spectrum analyser, the power spectral density (PSD) of the noise components of the laser was obtained in order to accurately yield the FSR. The theory for this is now briefly described. By the Wiener-Khinchin theorem, the power spectral density of the balanced photodetected MZI output is the Fourier transform of the autocorrelation of the output. From [69], the autocorrelation is a triangle function with a slope determined by the FSR of the MZI, whose Fourier transform is the sinc function. The PSD in terms of the FSR is given by:

$$S(\nu) \approx Csinc^2\left(\frac{\pi\nu}{\Delta\nu_{FSR}}\right), \tag{4.1}$$

where $S(\nu)$ is the PSD, ν is frequency, C is a constant, and $\Delta\nu_{FSR}$ is the FSR of the MZI.

4.2 Experimental Results

The PSD of the MZI was recorded over a period of two days, and an example of a single data trace is portrayed in Figure 4.1. A spectrogram of all the PSD measurement data is portrayed in Figure 4.2. In this plot each horizontal line represents a single PSD measurement, so that the all of the data can easily be visualized. The processed results are displayed in Figure 4.3 in terms of the FSR which yielded a reference value of 4.836±0.002 MHz. These PSD measurements were made with a resolution bandwidth of 1 kHz.

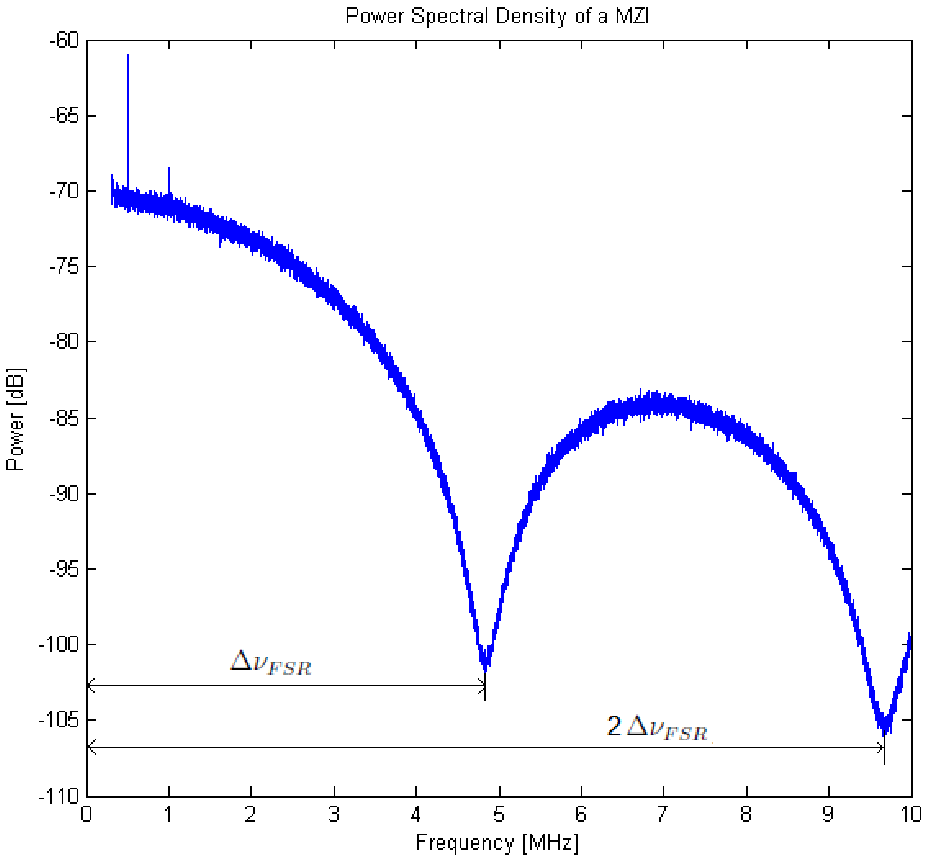

Figure 4.1: PSD measurement of MZI Noise Components.

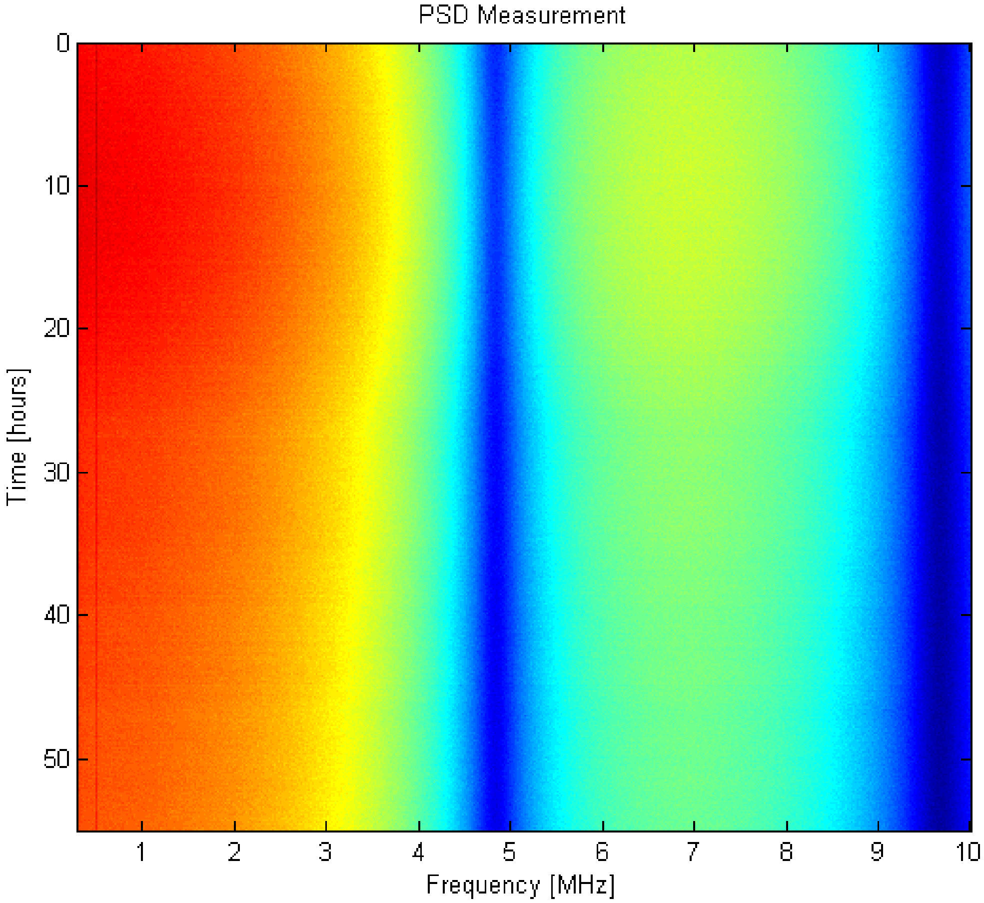

Figure 4.2: Spectrograph of PSD Measurement.

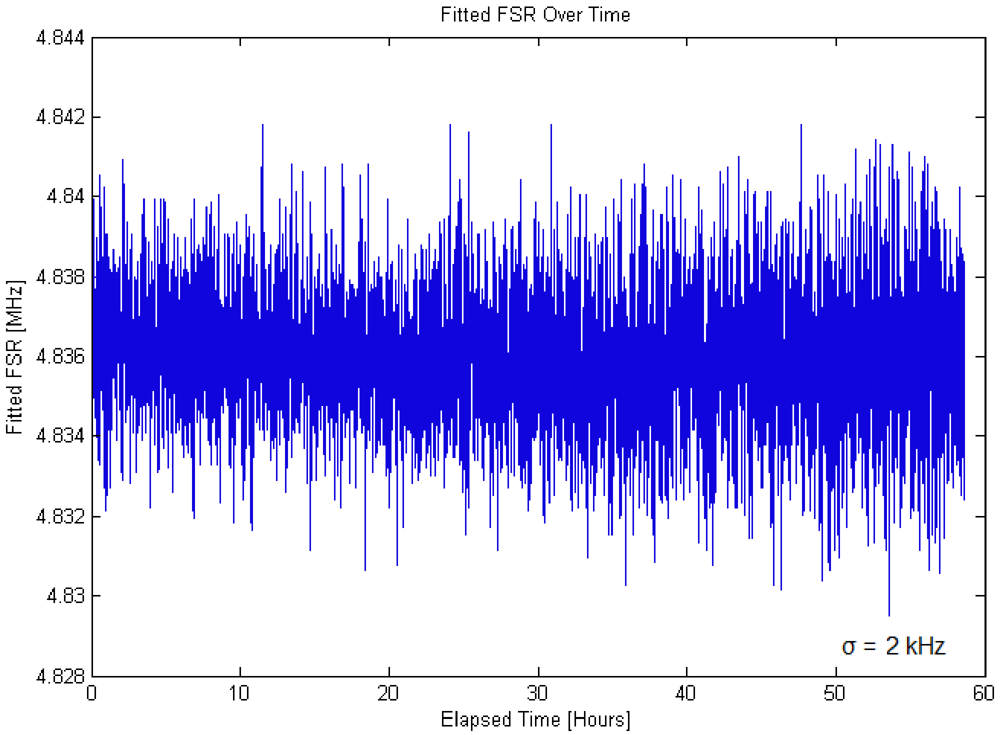

Figure 4.3: FSR measurement of a MZI.

By comparing the period of the parallel connected MZI and serial connected FPI to the reference MZI for over 8000 samples of data, the FSRs of the parallel connected MZI and serial connected FPI were determined. The experimental set-up for this is shown in Figure 4.4. The results are displayed in Table 4.2.

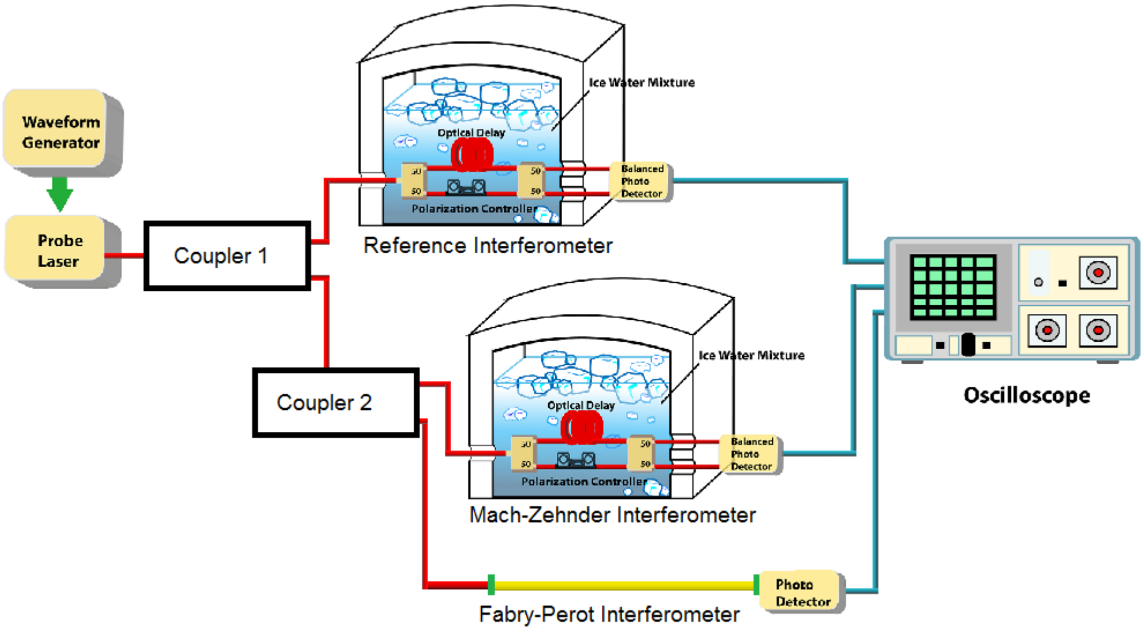

Figure 4.4: Experimental set-up for comparing interferometer signals.

Parameter	Value
Parallel connected MZI	36.6±0.1 MHz
Serial connected FPI	49.8±0.2 MHz

Table 4.1: FSR values of interferometers used in this work.

Chapter 5

Parallel Interferometry Techniques for Nanodetection

This chapter begins with an overview of previous research which utilized a parallel reference interferometer with a microtoroid based detection system. The experimental set-up, as well as the published achievements, are detailed. The work in the following section shows the versatility of this reference interferometer by using it with a microsphere based detection system. The experimental set-up, the analytical expressions of the optical transmission of the system, and simulation of the analytical expressions are covered. From the analytical expressions the LSF modelling equations and coefficients are obtained. This section also includes fitting results, experimental results, and it is concluded with a discussion.

5.1 Parallel Reference Interferometry with a Microtoroid

In previous research, a MZI was used in parallel with a microtoroid for nanodetection experiments [1]. The set-up used for this experiment is described as follows. On the left hand side of Figure 5.1 a 630 nm central wavelength probing laser is fed with a frequency modulating ramp signal from a waveform generator. The probing laser is sent via single-mode fiber optical cables through a polarization controller and then split by a directional coupler with part of the power fed to a thermally and mechanically stabilized MZI. The two output ports of the interferometer are detected by a balanced amplified photodetector upon being monitored by an oscilloscope. The

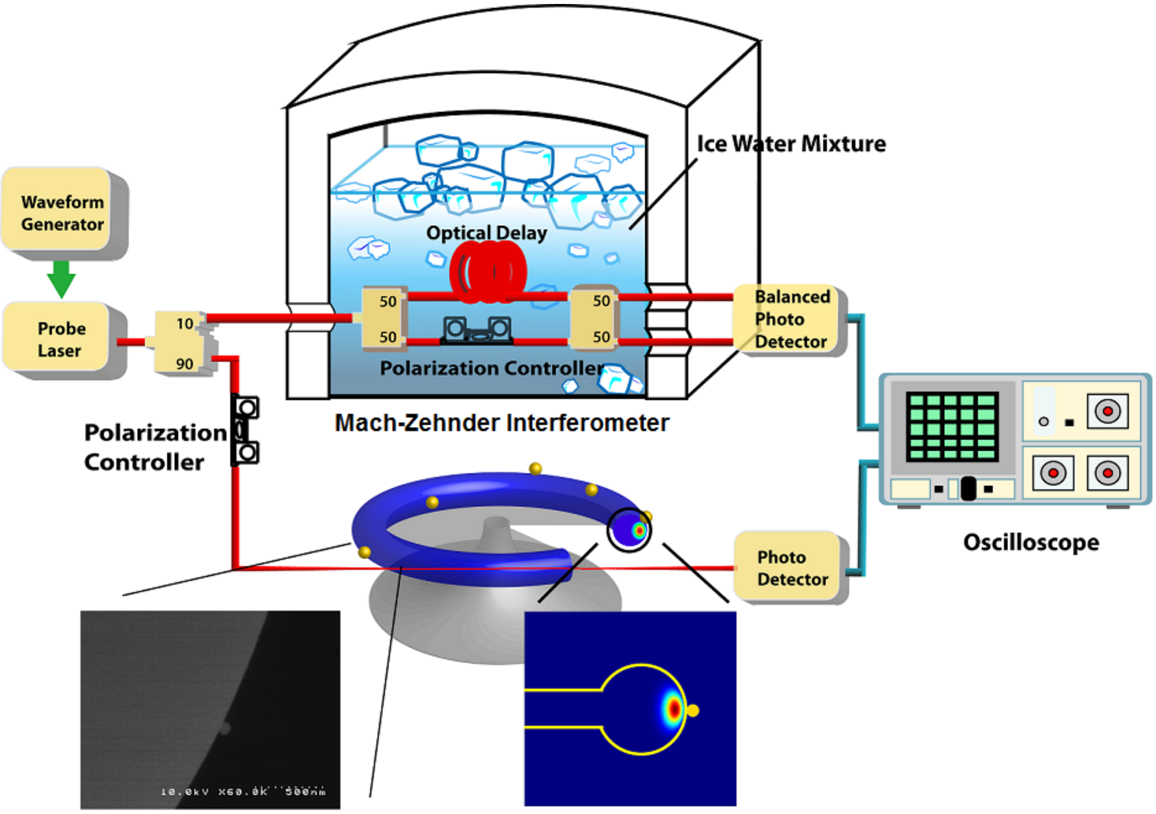

Figure 5.1: Parallel connected MZI set-up with a microtoroid from [1]. Reproduced here with permission from Tao Lu, and Xuan Du.

second part of the power from the laser is sent through a polarization controller and then enters a region of fiber optic taper. In the tapered region of the optical fiber a microtoroid is brought into proximity with a piezoelectric nanopositioning device so optical coupling occurs. The optical transmission spectrum from the coupled microcavity is photodetected, and the electrical signal is monitored on an oscilloscope.

The achievements of the parallel reference interferometer displayed in Figure 5.1 include permitting the detection of polystyrene nanobeads down to a radius of 12.5 nm, as well as detection of Influenza A with a greatly enhanced signal-to-noise ratio (SNR) over previous measurements [20]. With a push for detection of smaller and smaller particle sizes, this reference interferometer method could serve as an important component for nanodetection experimentalists.

5.2 Parallel Reference Interferometry with a Microsphere

To show that the reference interferometry method proposed in [1] can be used across different detection platforms with various microresonators, nanodetection experiments are carried out with the use of a microsphere. This section is separated into subsections devoted to the experimental set-up, analytic expressions of the system transmission, LSF equations and coefficients, simulation and fitting results, experimental results, and a discussion.

5.2.1 Experimental Set-up

The set-up for experiments with a MZI in parallel with a fiber taper coupled to a microsphere is depicted in Figure 5.2. The details of the set-up are identical to the experiment performed in [1], save for the use of a microsphere in place of a microtoroid. A 630 nm central wavelength probing laser is modulated with a frequency ramp signal from a waveform generator. After passing through a polarization controller, part of the optical power travels through the MZI before being photodetected by a balanced photodetector (BPD) . The remaining power is coupled to a microsphere through an optical taper before being detected by a photodetector (PD).

5.2.2 Analytic Equations of the System Output for Simulation of Experimental Data

The equations governing the components of the system, namely the coupled microcavity and the MZI, have both been detailed in the previous chapter. The analytic equations for the total output power from the coupled microsphere, and from the MZI are given by Equations 3.7 and 3.14, respectively. The next step is to consider what takes place in order to effectively monitor the transmission from both the MZI and the coupled microcavity.

The monitoring of each system happens on an oscilloscope, which requires the optical power transmissions from both the coupled microsphere and the MZI to first be converted to an electrical signal. For the case of the MZI, the conversion is accomplished using a dual input BPD which takes both outputs from the MZI and produces a current proportional to the difference between the two optical powers. The benefits

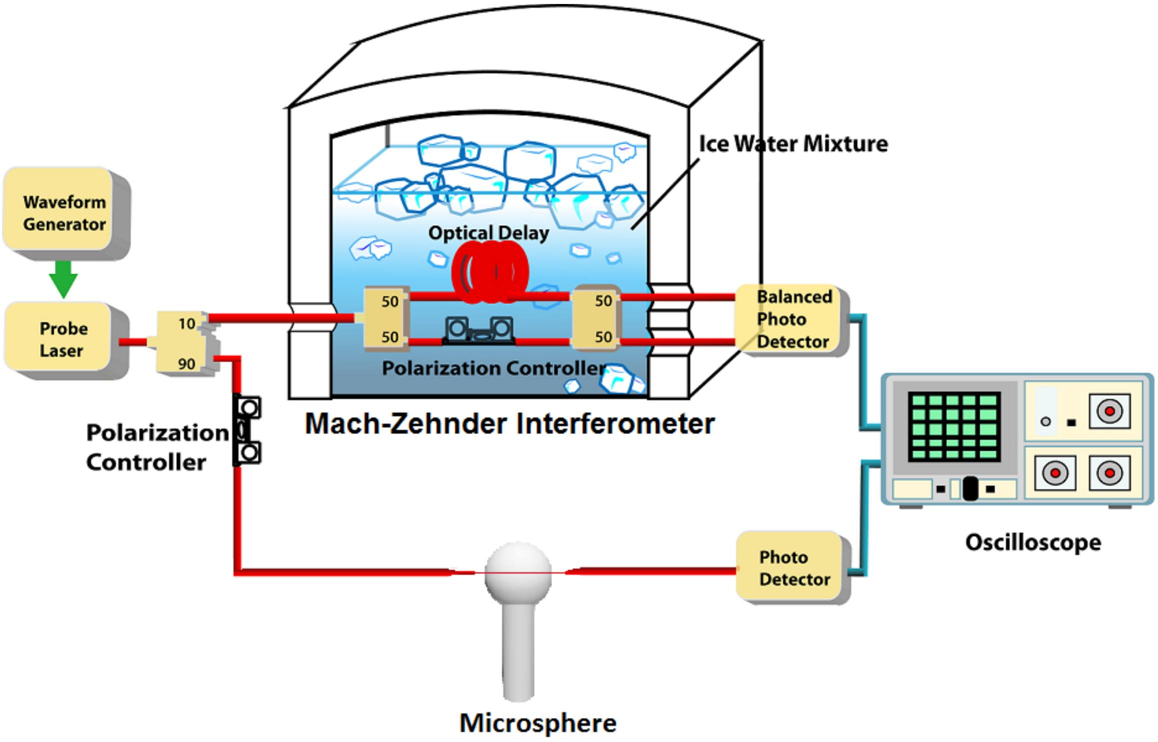

Figure 5.2: Parallel connected MZI set-up with a microsphere. Modified from [1] with permission from Tao Lu, and Xuan Du.

of using a BPD with both channels, as opposed to using a single output with a single input PD is that there is a reduction in common mode noise from the laser. For the case of the power from the coupled microsphere a PD is used which creates a current. The currents from both PDs are converted to a voltage which can be monitored on an oscilloscope. The output voltages for the MZI and coupled microsphere are, respectively:

$$V_{out,\,MZI}(\nu_L) = G_{BPD}\mathscr{R}_{BPD}(P_{out2,\,MZI}(\nu_L) - P_{out1,\,MZI}(\nu_L)). \tag{5.1}$$

$$V_{out,\,\mu sphere}(\nu_L) = G_{PD}\mathscr{R}_{PD}P_{out,\,\mu sphere}(\nu_L). \tag{5.2}$$

Here G_{BPD} and G_{PD} are the transimpedance amplifier gain of the BPD and PD in volts per Ampére, $\mathscr{R}_{BPD}$ and $\mathscr{R}_{PD}$ are the responsivities of the BPD and PD in units of Ampéres per Watt, and $P_{out,\,MZI}$ and $P_{out,\,\mu sphere}$ are the output powers from the interferometer and coupled microsphere components of the system with units of Watts.

By substituting both terms from Equation 3.14 as $P_{out1,\,MZI}$ and $P_{out2,\,MZI}$, the output powers from the MZI, and Equation 3.7 as $P_{out,\,\mu sphere}$, the output power from the microsphere, the above equations become:

$$V_{out,\,MZI}(\nu_L) = V_{MZI}cos\left(\frac{2\pi\nu_L}{\Delta\nu_{FSR}}\right) \tag{5.3}$$

$$V_{out,\,\mu sphere}(\nu_L) = V_{\mu sphere}\left(1 - \frac{4K}{(1+K)^2 + \frac{2Q_0}{\nu_L^2}(\nu_R - \nu_L)^2}\right). \tag{5.4}$$

Where

$$V_{MZI} = G_{BPD}\mathscr{R}_{BPD}P_{in,\,MZI} \tag{5.5}$$

and

$$V_{\mu sphere} = G_{PD}\mathscr{R}_{PD}P_{in,\,\mu sphere} \tag{5.6}$$

are the voltage amplitudes from the MZI and microsphere in terms of the input powers to the MZI and microsphere, respectively.

When the transmission is measured on an oscilloscope the dependent variable is time. In order to achieve this with the analytical equations, one must consider the intricacies of the experimental set-up. The pump laser is swept with a frequency modulating voltage signal to achieve a laser frequency that changes linearly over time. The exact conversion factor is dependent on the laser, and it will be referred to as the laser scan rate, S_ν, which has units of Hertz per second. To make Equations 5.3 and 5.4 into time dependent signals, they must be made to incorporate the laser scan rate. This is done by changing the parameters involving the laser frequency, as follows: replace the laser frequency ν_L with $\nu_L = S_\nu(t - t_0) + \nu_{L0}$, where S_ν is the scan rate, t_0 is the zero point of the frequency modulation, and ν_{L0} is the central operating frequency of the laser. In this case, the output voltages for the parallel reference interferometry system become:

$$V_{out,\,MZI}(t) = V_{MZI}cos\left(\frac{2\pi(S_\nu(t - t_0) + \nu_{L0})}{\Delta\nu_{FSR}}\right) \tag{5.7}$$

$$V_{out,\,\mu sphere}(t) \quad = \quad V_{\mu sphere}\left(1 - \frac{4K}{(1+K)^2 + \frac{2Q_0(S_\nu(t-t_0)+\nu_{L0}-\nu_R)^2}{(S_\nu(t-t_0)+\nu_{L0})^2}}\right). \tag{5.8}$$

An example of simulation results obtained with these equations is plotted in Figures 5.3 and 5.4 with parameters given in Table 5.2.4.

5.2.3 Least Squares Fit

The task, now that the simulation equations have been outlined, is to develop modelling equations for the LSFs of Equations 5.7 and 5.8. The modelling equations will consist of functional forms as found in the simulation equations, with various coefficients to be optimized by the fitting algorithm. To follow is an outline of the modelling equations where the coefficients are introduced and written in terms of the physical properties of each system. The significance of the coefficients in terms of their impact on the fitting curve is explained, and signal processing methods are developed to automatically generate initial guess values. An important part of performing a LSF is to provide the fit an initial guess for all of the coefficients, as this guess serves as a starting point for the procedure. By choosing an appropriate starting point the time required for the fit to be completed can be kept to a minimum. Finally some fits are performed on simulation data, and their produced wavelength errors are examined in order to understand the limits of the fitting procedure when it is used to measure wavelength shifts.

Modelling Equation and Coefficients

The equations used to perform the LSF on the MZI system are given by

$$V_{model,\,MZI}(t) = V_{01}cos(b(t-c)) \tag{5.9}$$

and

$$V_{model,\,\mu sphere}(t) = V_{02}\left(1 - \frac{I\gamma^2}{\gamma^2 + (t-d)^2}\right). \tag{5.10}$$

The coefficients, by matching Equation 5.7 to Equation 5.9 and Equation 5.8 to Equation 5.10 can be expressed in terms of the physical parameters as follows:

$$V_{01} = V_{MZI}, \tag{5.11}$$

$$V_{02} = V_{\mu sphere}, \tag{5.12}$$

$$b = \frac{2\pi S_\nu}{\Delta\nu_{FSR}}, \tag{5.13}$$

$$c = t_0 - \frac{\nu_{L0}}{S_\nu}, \tag{5.14}$$

$$I = \frac{4K}{(1+K)^2}, \tag{5.15}$$

$$\gamma = \frac{\nu_{L0}(1+K)}{2Q_0 S_\nu}, \tag{5.16}$$

and

$$d = t_0 + \frac{\nu_R - \nu_{L0}}{S_\nu}. \tag{5.17}$$

How the Coefficients determine the shape of the Curve, and Signal Processing Techniques for Automatic Coefficient Guessing

By inspecting Equations 5.9 and 5.10 one can arrive at the following conclusions about the fitting coefficients. The amplitude of the sinusoidal and Lorentzian signals are coefficients 'V_{01}' and 'V_{02}', respectively, and coefficients 'b' and 'c' respectively describe the frequency of oscillation and phase of the sinusoid. Coefficient 'I' is the amplitude of the dip of the Lorentzian signal, and lastly coefficients 'γ' and 'd' correspond to the half width at half maximum (HWHM) and location of the Lorentzian dip, again in their respective order. These coefficients are plotted in Figures 5.3 and 5.4 in context of simulated data.

The start point coefficients are generated as follows. For the sinusoidal fit, $V_{model,\,MZI}$, the amplitude, coefficient 'V_{01}', is taken to be half of the difference between the $V_{out,\,MZI}(t)$ maximum and minimum. Coefficient 'b', the frequency, is obtained by finding the relative time difference between the first two points where $V_{model,\,MZI}(t)$ approaches zero. When the signal is noisy, there is likely to be many zero crossings around the point the sinusoid goes to zero. To get around this, the signal is smoothed with a moving average. The time difference between two zero

Parameter	Value
Resolution	20 ns
Total Q	5×10^7
Resonant Wavelength	635.5 nm
FSR	36.1 MHz
Signal Amplitude	1 V
Scan Rate	1.0×10^{12} Hz/s
SNR	25

Table 5.1: Parallel MZI simulation parameters.

crossings of the smoothed signal corresponds to half of the period, which in turn, yields the frequency. In order to find the frequency normalized phase shift, coefficient 'c', the first crossing in time where the smoothed signal goes from being a negative to positive value is determined. The signal follows a cosine function, so this crossing corresponds to a $\frac{\pi}{2}$ phase advance. The coefficient can thus be approximated as the time of the crossings advanced by $\frac{\pi}{2b}$ and delayed by half the time range.

In order to determine the start point for coefficients of the function fitting the Lorentzian signal, $V_{out,\,\mu sphere}$, the following method is employed. Coefficient 'V_{02}' is found by finding the maximum of $V_{out,\,\mu sphere}$. Coefficient 'I', the amplitude of the Lorentzian dip, can be obtained by subtracting the ratio of the minimum of $V_{out,\,\mu sphere}(t)$ to the maximum of $V_{out,\,\mu sphere}(t)$ from one. The HWHM of the Lorentzian signal, coefficient 'γ', is approximated by finding half of the time difference between the consecutive zero points of half of the $V_{out,\,\mu sphere}(t)$ maximum subtracted from $V_{out,\,\mu sphere}(t)$. Lastly, to determine the time location of the Lorentzian dip, coefficient 'd', the minimum of $V_{out,\,\mu sphere}(t)$ is found.

5.2.4 Simulation and LSF Results and Fit Error Determination for Finding the Sensing Limitations Imposed by the LSF Method

LSFs were performed on data simulated with Equations 5.7 and 5.8 using the physical parameters listed in Table 6.1.3. The fits are compared to simulated data in Figures 5.3 and 5.4, and the resonant wavelength error for fits performed on data simulated with the resonant frequency spanning a full FSR is displayed in Figure 5.5. In figure 5.5, and subsequently in this work the units of 'am' refer to attometers, or 10^{-18} meters.

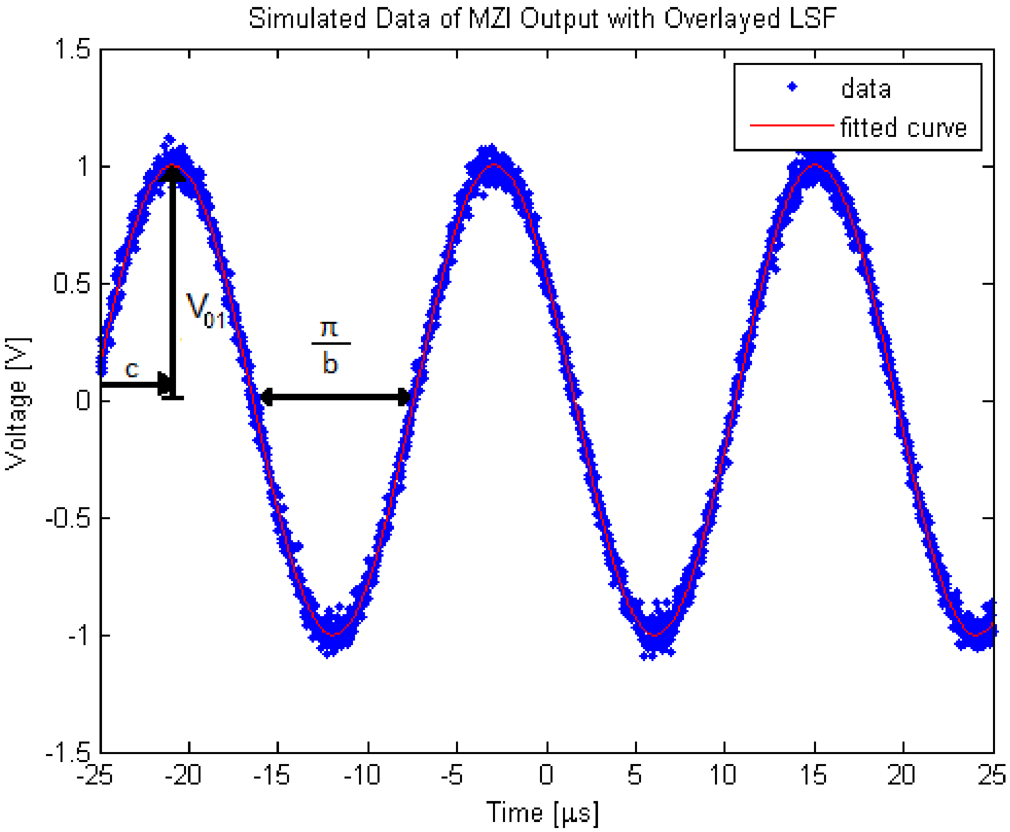

Figure 5.3: Parallel MZI simulation and LSF results: interferometer transmission.

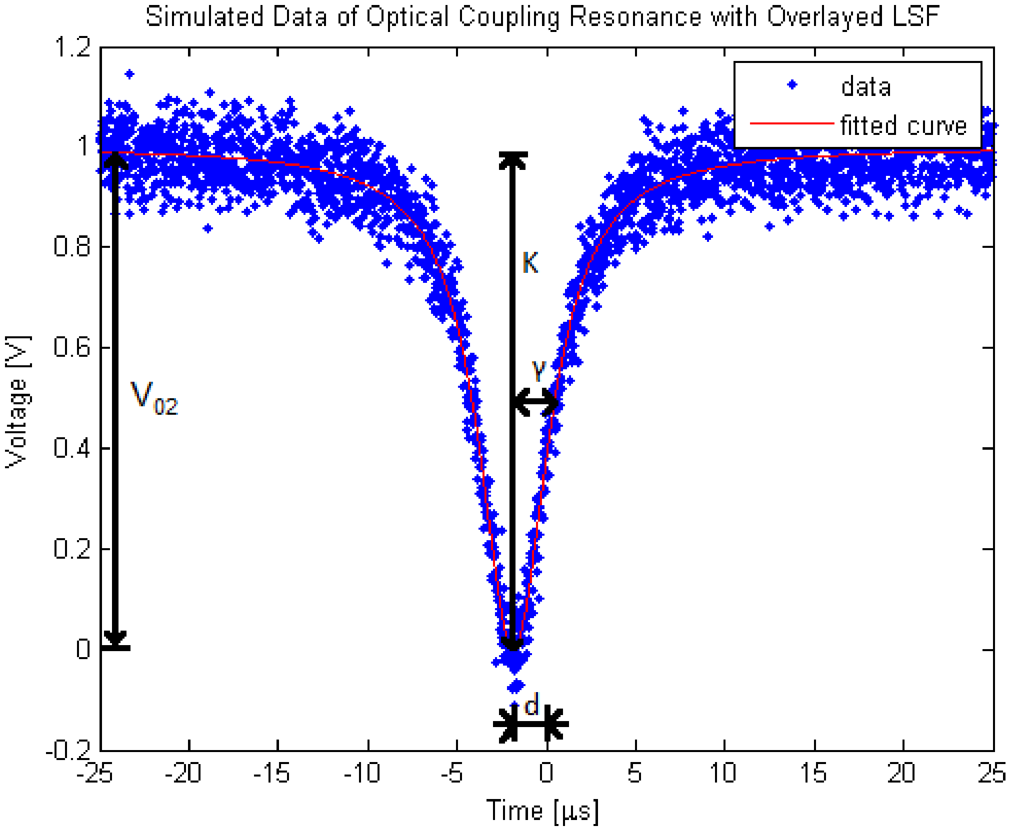

Figure 5.4: Parallel MZI simulation and LSF results: coupling transmission.

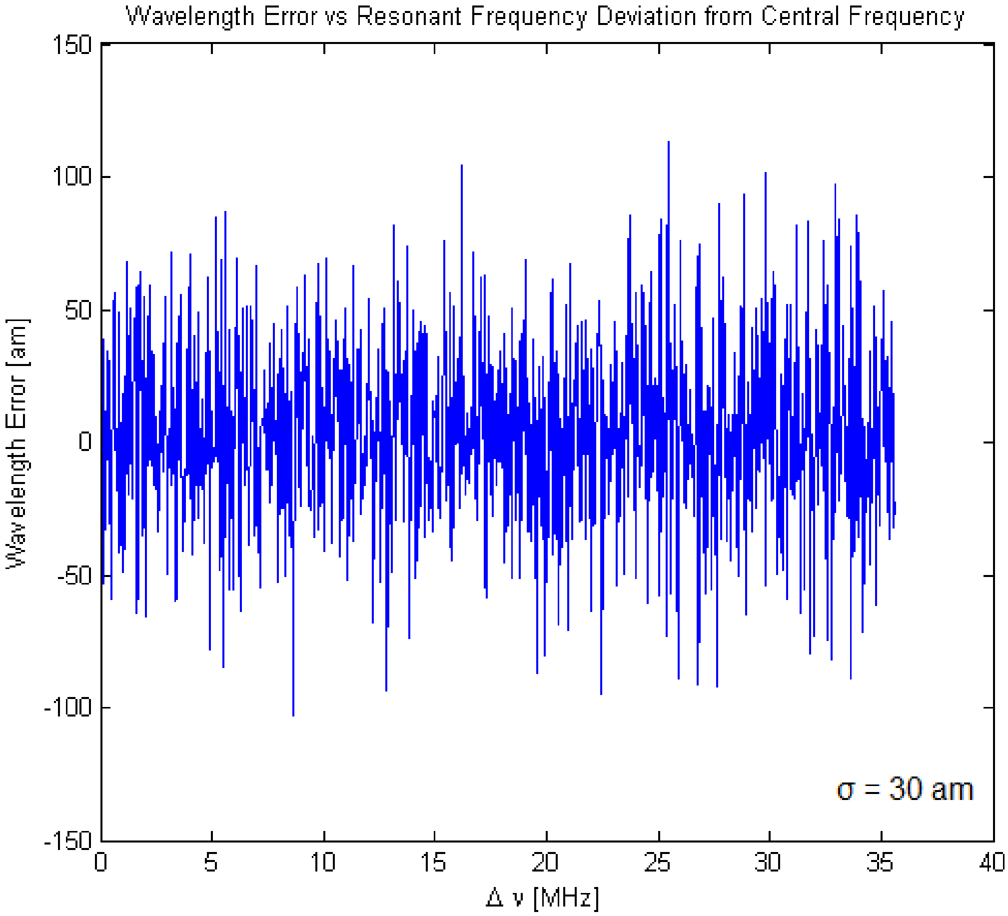

Figure 5.5: Parallel MZI simulation resonant wavelength error.

To show how the SNR of the system output effects the returned wavelength error, the wavelength error is plotted as a function of SNR in Figure 5.6. Here the resonant wavelength is fixed, and the only thing that varies is the SNR. The data is generated using the physical parameters given in Table 5.2.4. Because the noise is randomly generated, 20 data points are plotted for each SNR with a 3σ envelope shown in red.

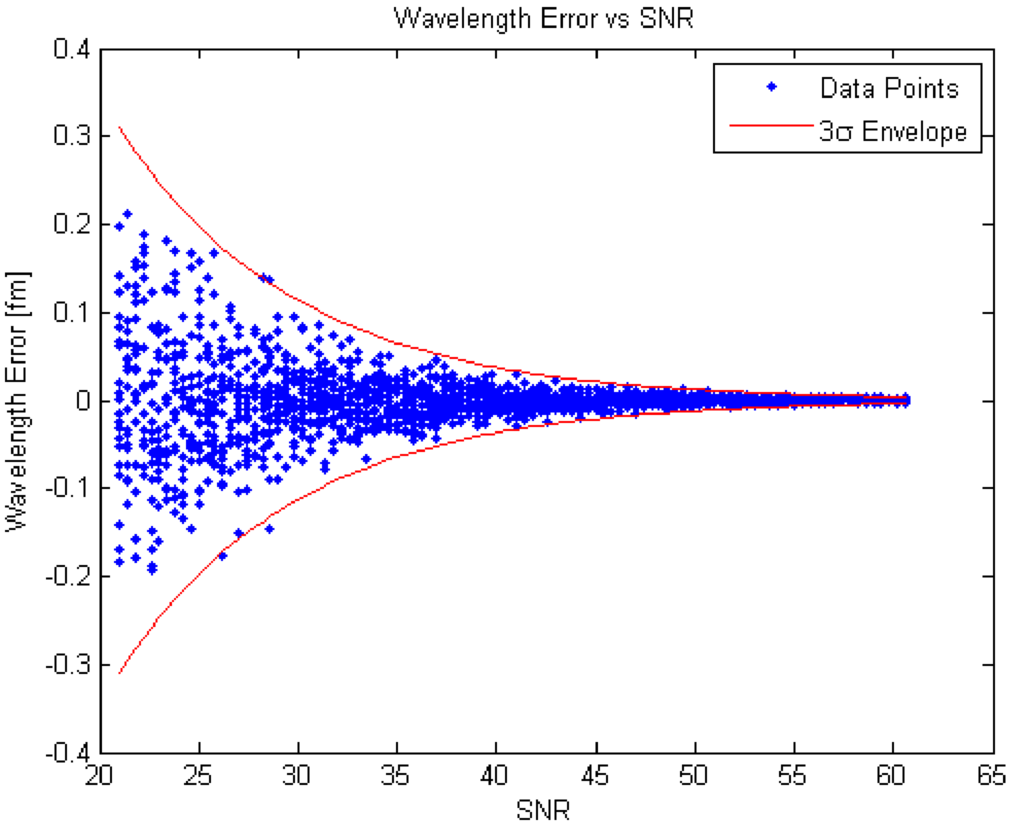

Figure 5.6: Parallel MZI simulation of resonant wavelength error vs SNR.

5.2.5 Experimental Results

To begin the preparation for the experiment, a new fiber optical taper is pulled to minimize any contamination from dust that may be on an older taper. Once this is completed work is carried out to set up a new microsphere sample. To begin the experiment, the microsphere is brought into proximity to the fiber taper. The fiber taper is then brought into nanoscale proximity to couple it to the microsphere using a piezo-electric nanopositioner. Using the nanopositioner, next step is to find an optimum coupling position between the taper and the microsphere by monitoring the transmission dip on an oscilloscope. This is typically a trade-off between signal stability and Q, with the less stable undercoupled regime typically has a higher Q than the more stable undercoupled regime.

Once a sufficiently stable resonant transmission dip with high enough Q is observed on the oscilloscope, the first data capture is ready to take place. The traces from the oscilloscope are captured at a sampling rate of 10 milliseconds using a LabView driving program. To allow comparison of the interferometer method with the conventional method for resonant wavelength shift detection the voltage ramp corresponding to the frequency modulation used to scan the laser is also captured simultaneously with the signals from the interferometer.

For experiments performed in buffer, the fiber taper and microsphere are uncoupled and removed from each other. Buffer solution is carefully injected onto the microsphere sample. Then the fiber taper is brought into the buffer solution and into proximity to the microsphere. Once the taper has been successfully brought into the buffer, the degassed buffer is injected, while removing the excess. Again, an optimum resonant dip is achieved, and data is collected as described above.

The results of the LSF performed on experimental data are plotted in Figures 5.7 and 5.8.

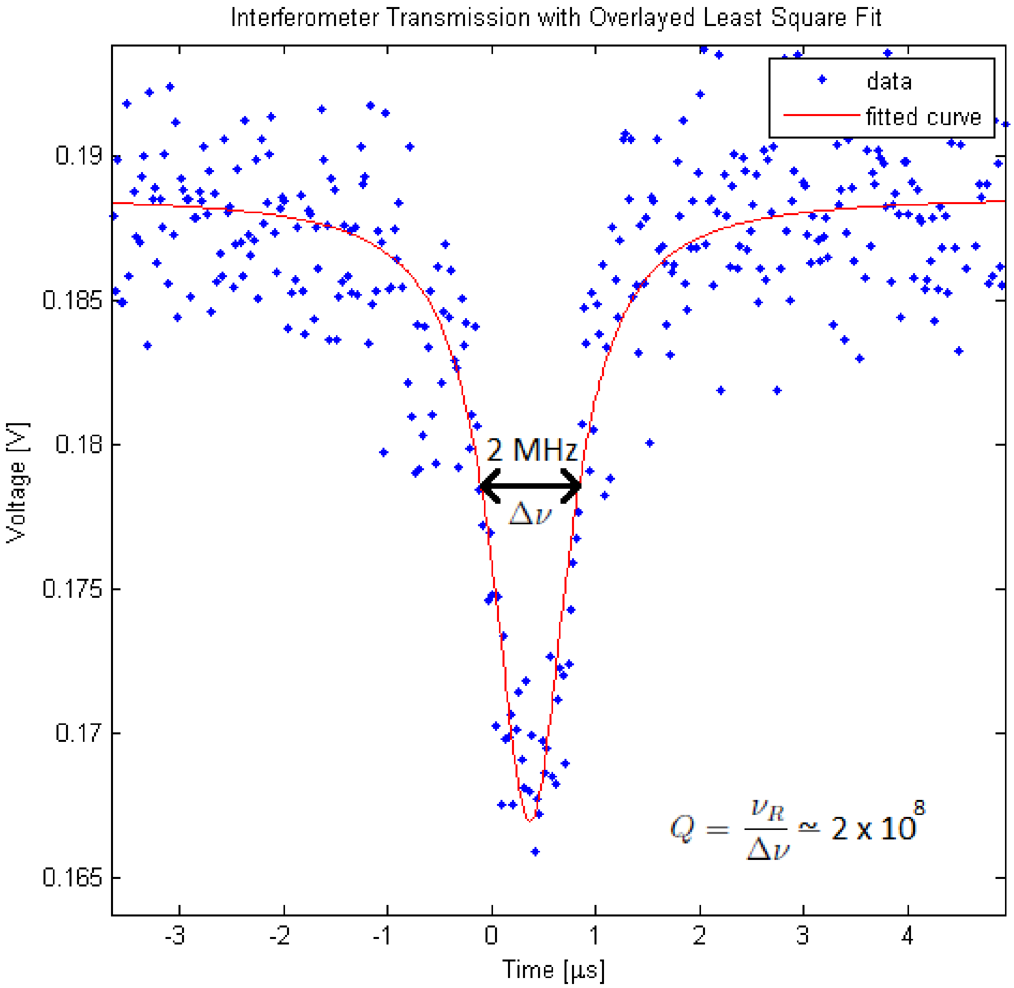

Figure 5.7: Parallel MZI experimental data with fitting results: coupling transmission.

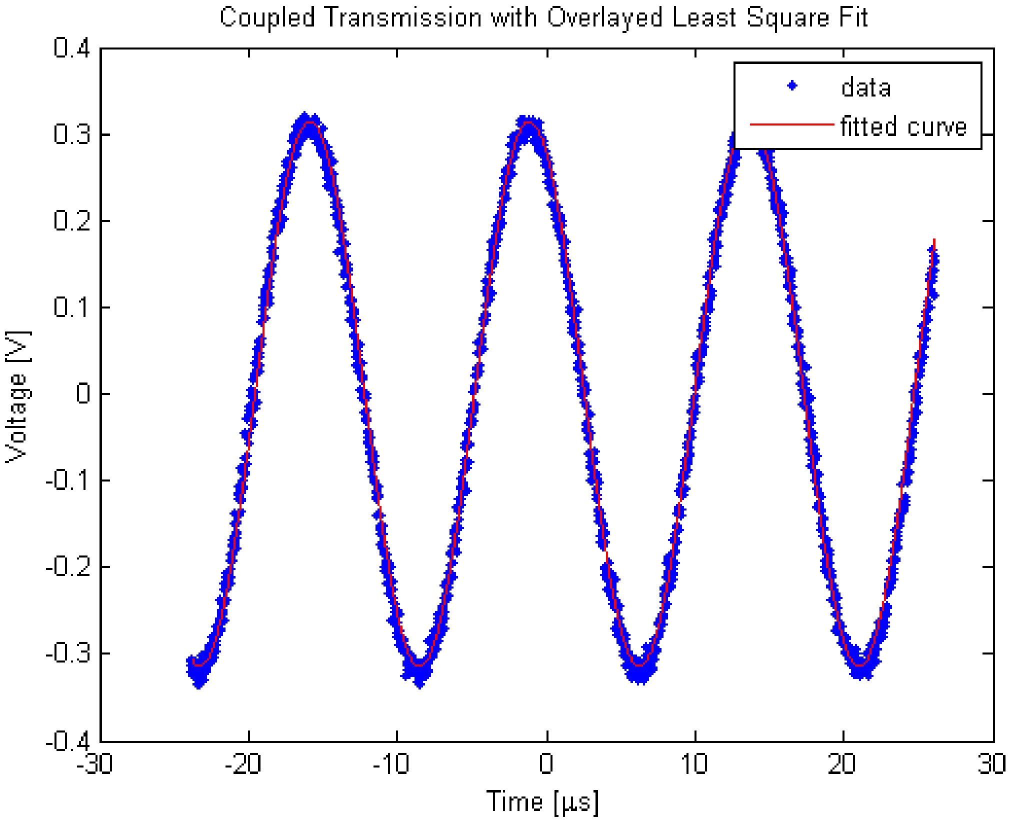

Figure 5.8: Parallel MZI experimental data with fitting results: interferometer transmission.

An experiment was performed in a buffer solution to show the merits in correcting for the frequency jitter, it is displayed in Figure 5.9. Plots illustrating the LSF performed on the experimental data are shown in Figures 5.7 and 5.8. For Figure 5.9 the blue trace corresponds to the resonant wavelength returned by the LSF after it has been corrected for laser jitter, and the grey trace indicates the resonant wavelength returned by the conventional method. In order to demonstrate the improvement on sensitivity for wavelength step detection, the variance of ten data points before and after each data point is obtained, added together, and turned into a standard deviation. This represents the uncertainty in wavelength if a step had occured at each data point. Before the variance is calculated, a three point average is taken over all the data. A plot of this experimental sensitivity is produced in Figure 5.10 for the conventional (grey) and interferometer method (blue). The experimental sensitivity of the fitted and jitter corrected resonant wavelength is 0.14 ± 0.09 fm, and the sensitivity of the resonant wavelength found with the conventional method is 2.1 ±

Parameter	Value
Resolution	25 ns
Total Q	$(2.0 \pm 0.1) \times 10^8$
Resonant Wavelength	635.9 ± 0.1 nm
FSR	36.6 ± 0.1 MHz
Laser Power	9.0 ± 0.1 mW
Scan Rate	$(4.0 \pm 0.1) \times 10^{12}$ Hz/s
SNR	28

Table 5.2: Parallel MZI experimental physical parameters.

0.5 fm. The physical parameters of this experiment are given in Table 5.2.5.

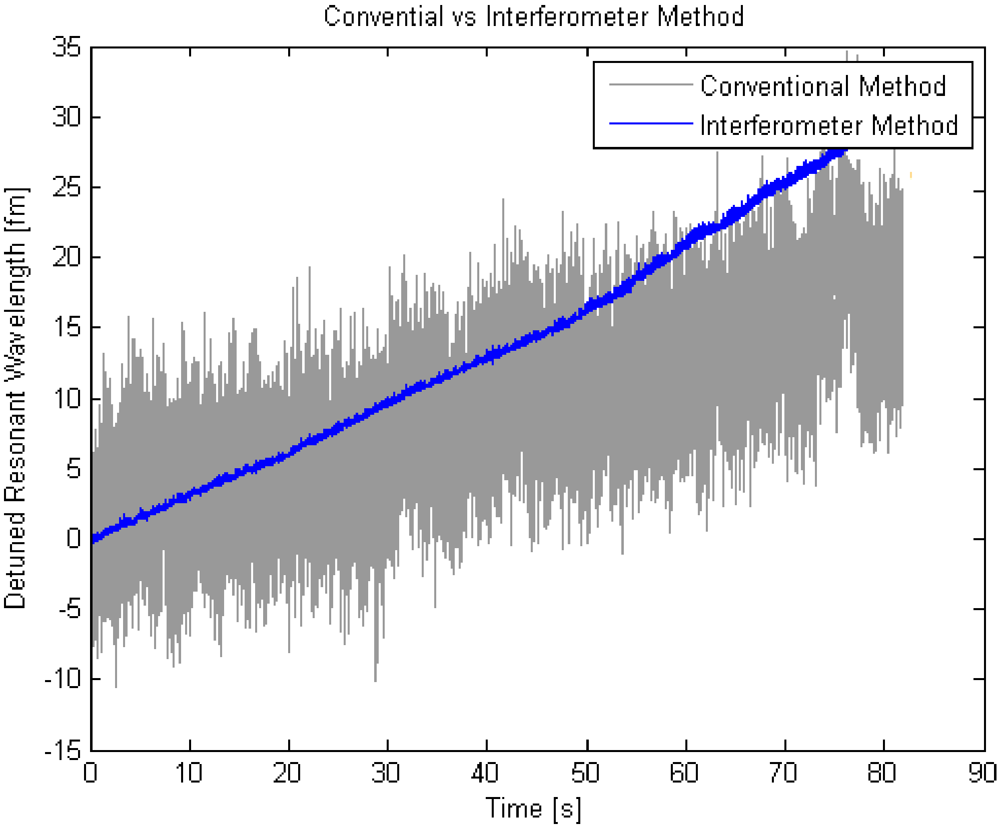

Figure 5.9: Parallel MZI experimental results in buffer.

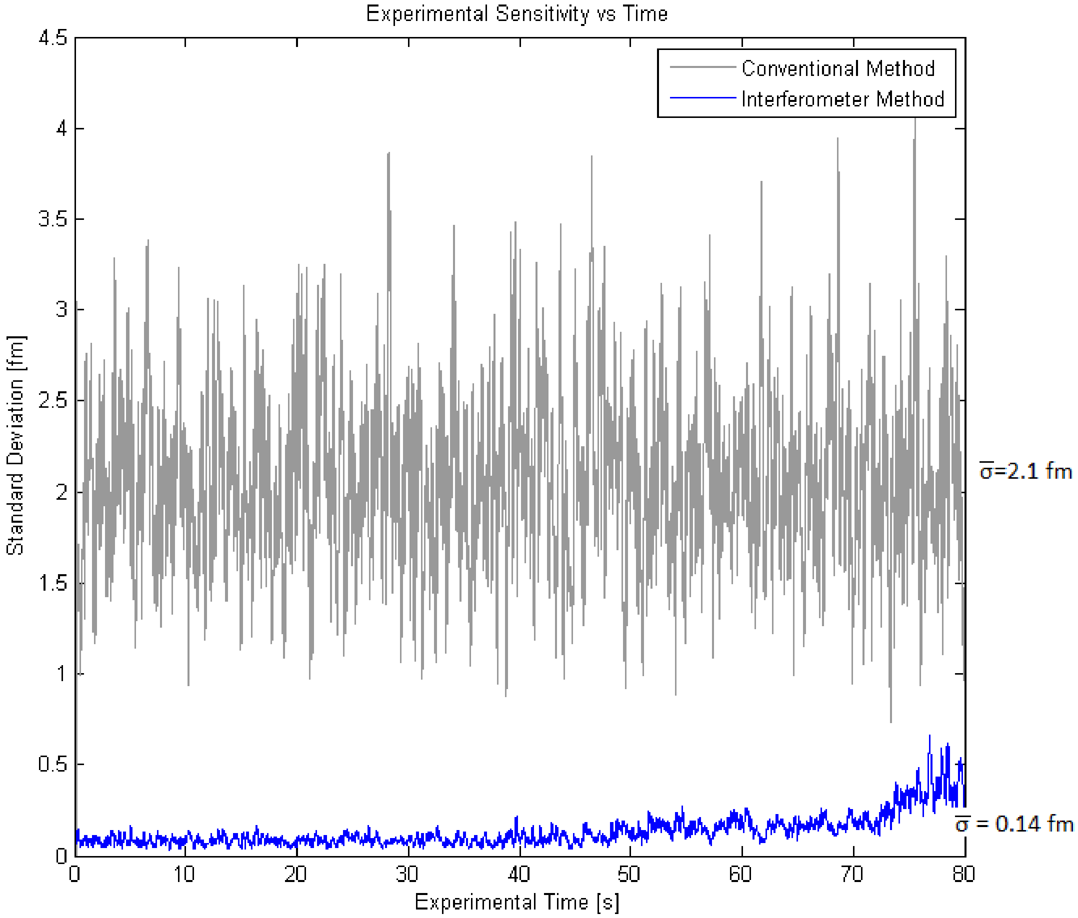

Figure 5.10: Parallel MZI experimental sensitivity in buffer.

In order to demonstrate the effectiveness of the LSF performed on the buffer experiment, a comparison of the spectrograms of the experimental data and data fits is depicted in Figures 5.11 and 5.12. Each horizontal line in the spectrogram corresponds to one trace from the oscilloscope. Both axes correspond to time, the horizontal axis is the time corresponding to the oscilloscope trace, and the vertical axis corresponds to the experimental time, in other words, the relative time the trace was obtained. Furthermore, the effects of correcting for the laser jitter are demonstrated in Figure 5.13. In these images, each fitted data trace (or horizontal line) is shifted to keep the phase of the interferometer constant. By doing this, the jitter is effectively removed. Also included in Figure 5.14 is a spectrogram of the scanning voltage, which as used to determine resonant wavelength the curve for the conventional method. This figure shows that the scanning voltage is increasing with time, due to laser drift.

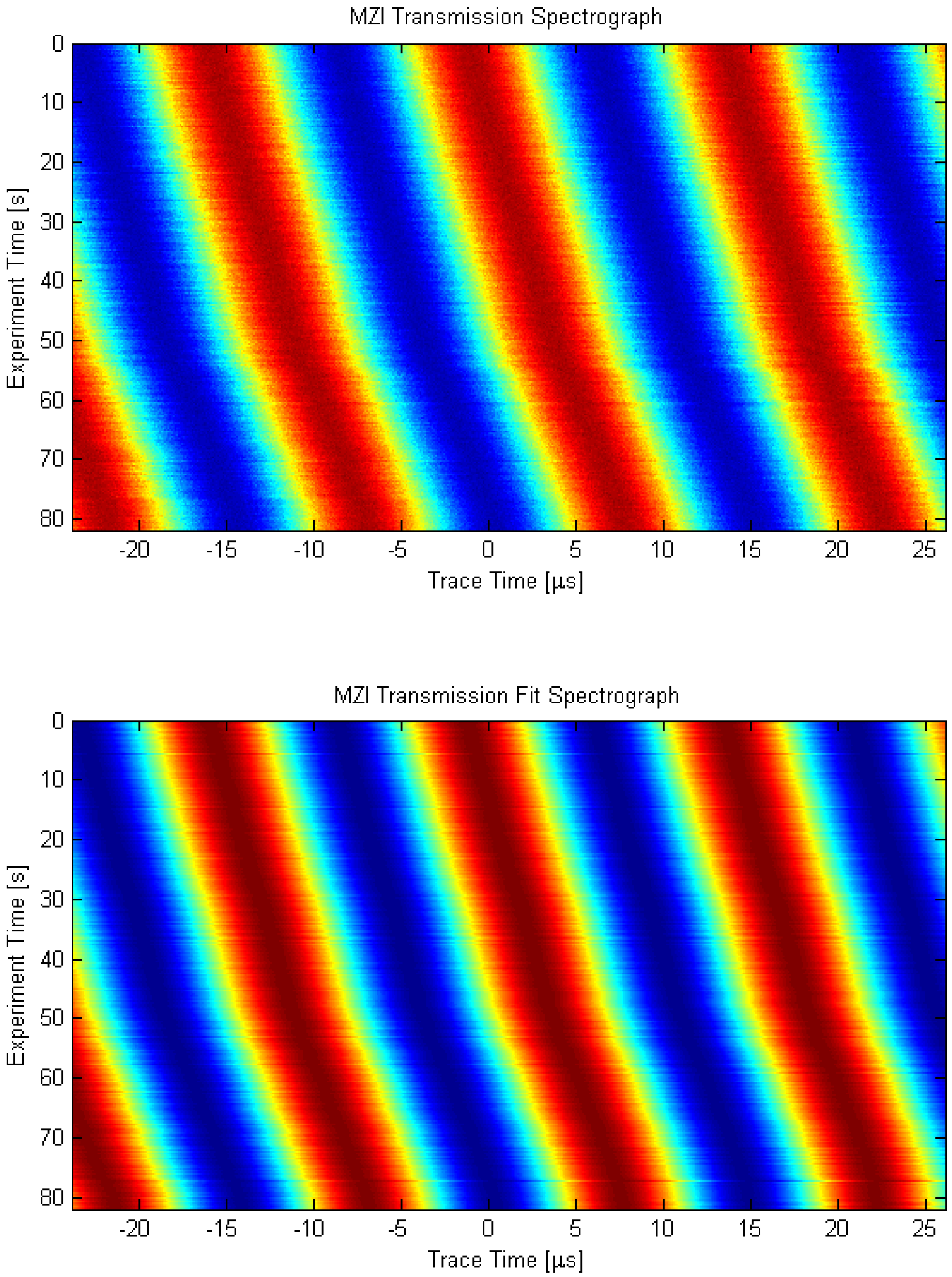

Figure 5.11: Parallel MZI spectrograms of experimental data and fitting results: interferometer transmission.

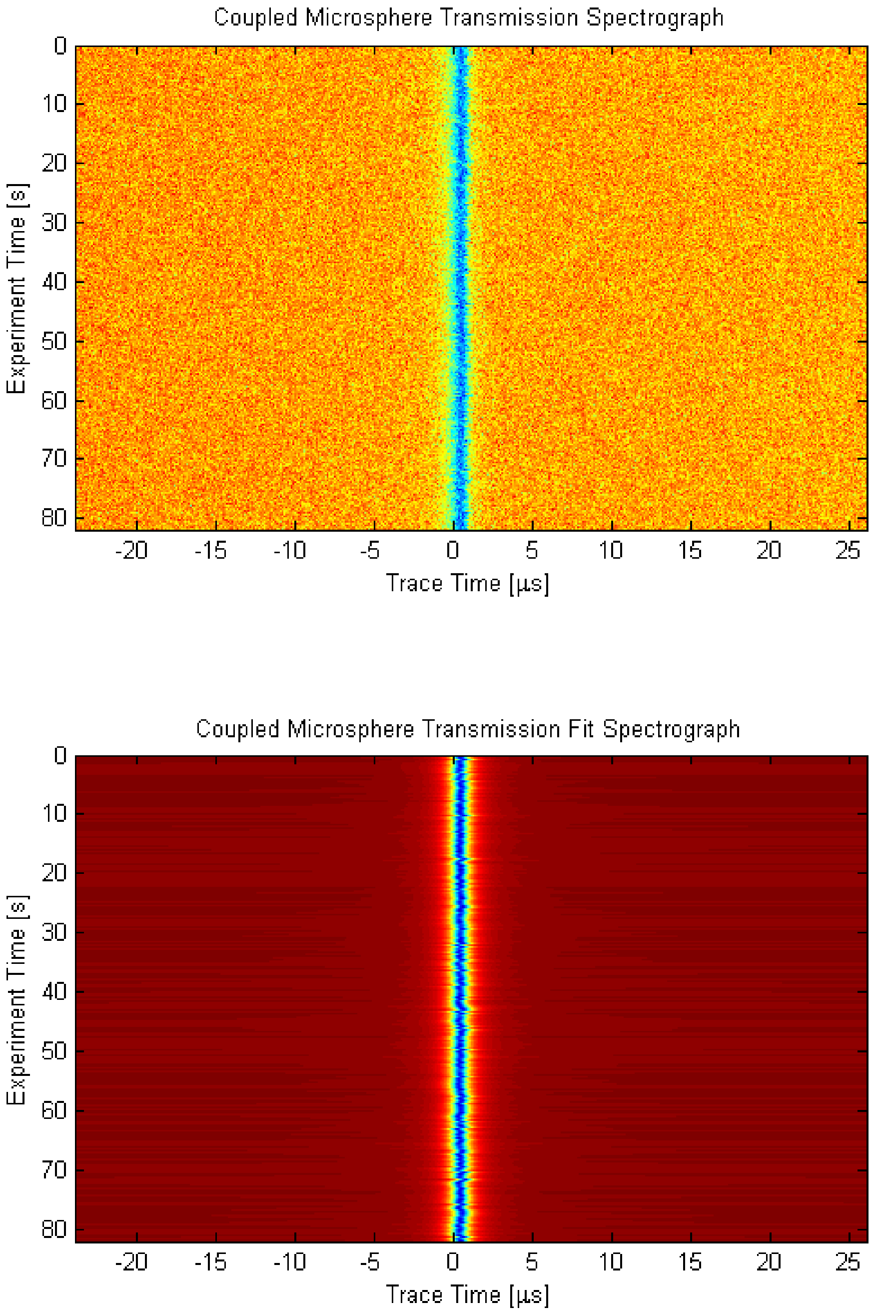

Figure 5.12: Parallel MZI spectrograms of experimental data and fitting results: coupling transmission.

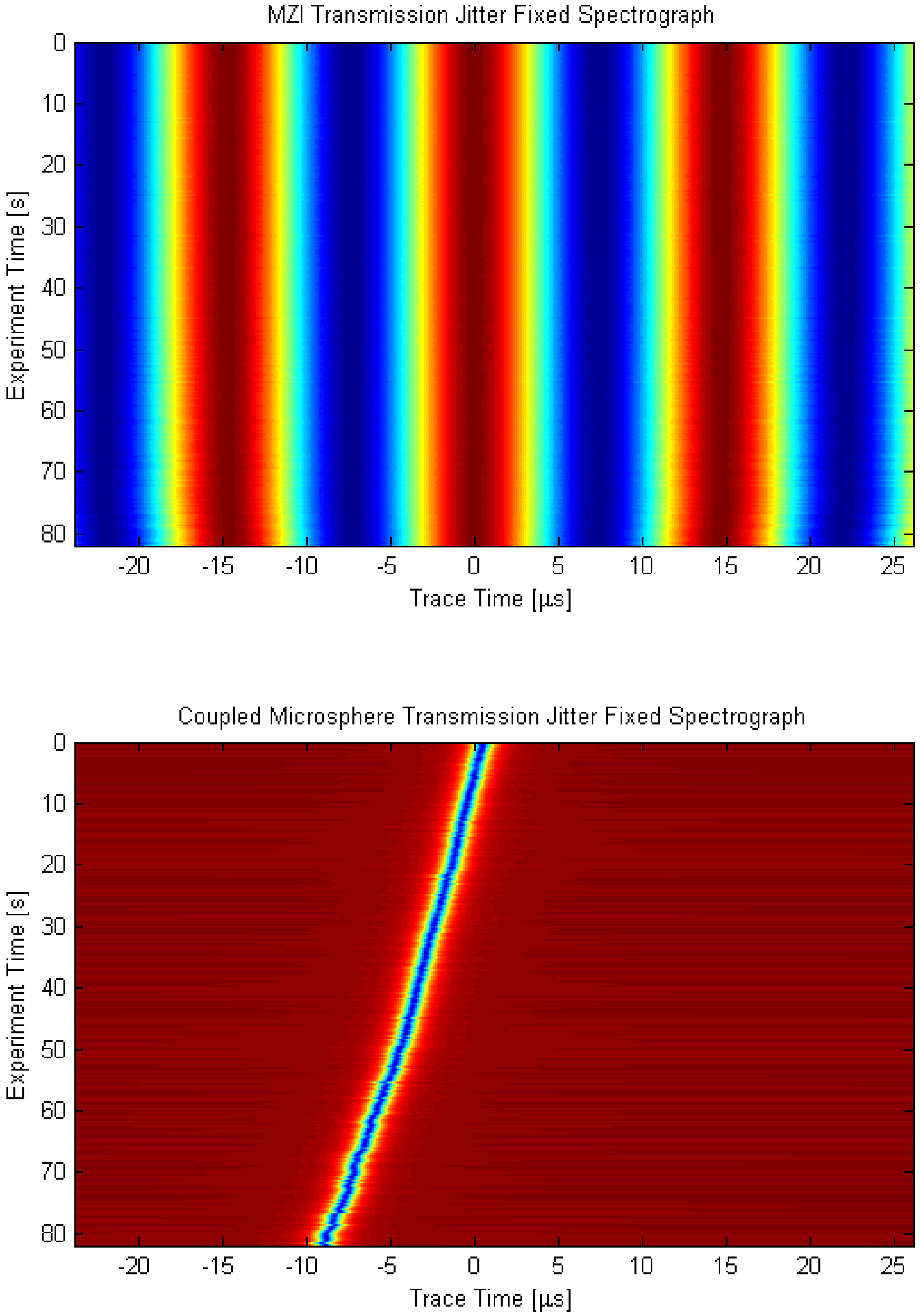

Figure 5.13: Parallel MZI spectrograms of fitted experimental data corrected for laser jitter.

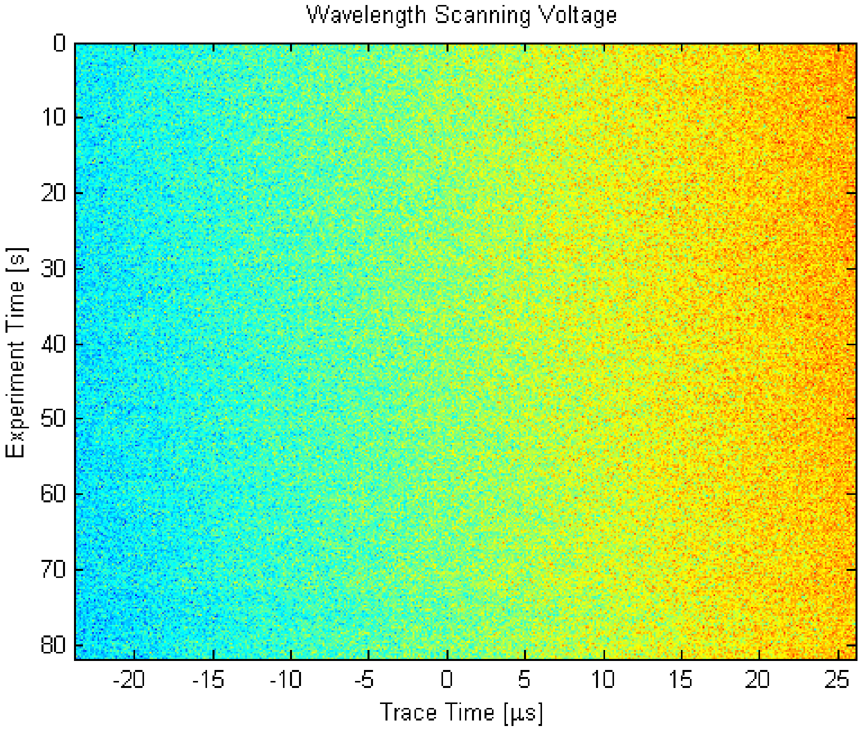

Figure 5.14: Parallel MZI spectrogram of experimental data: scanning voltage used for conventional method.

To ensure that the LSF is properly working and not returning meaningless data, a temperature ramp is applied to the microresonator via a lamp. It is noted that this experiment is performed in air. The heating of the microsphere changes its resonant wavelength, and this can clearly be seen in Figure 5.15. Each data point represents the resonant wavelength of a single instance in time. The experiments collected 8192 data points with a ten millisecond sampling rate. The blue trace corresponds to the resonant wavelength returned by the LSF after it has been corrected for laser jitter. The grey trace indicates the resonant wavelength returned by the conventional method. An exponential fit was performed on the data collected after the heating lamp was turned off, as depicted in Figure 5.16. The fitted curve yielded a time constant, τ_T, as described in Appendix B. The value of the experimental time constant, 1.19±0.06 s, is in direct agreement with the accepted time constant for fused silica, 1.18 s.

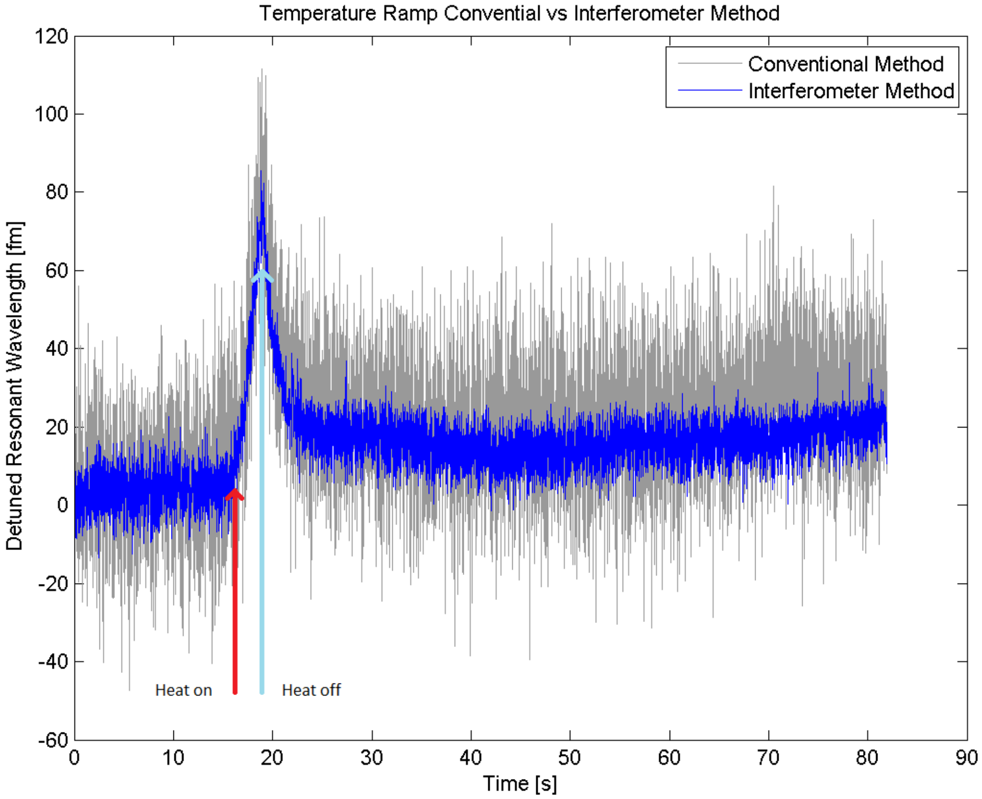

Figure 5.15: Parallel MZI experimental results in air with a temperature ramp.

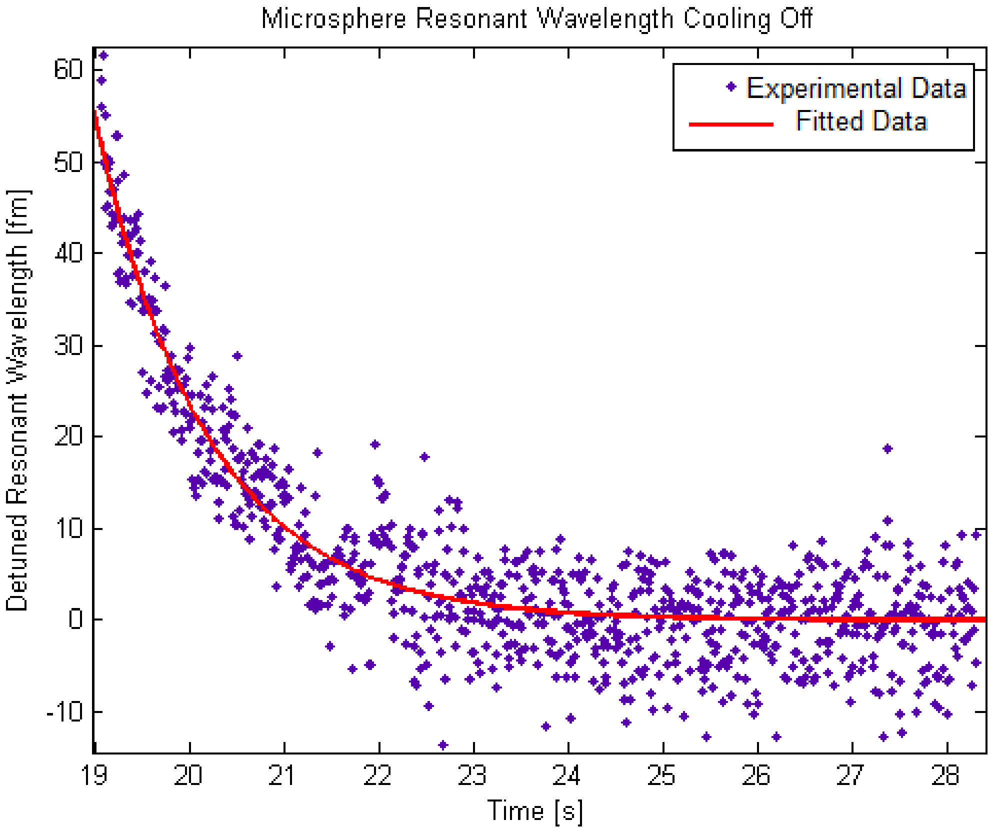

Figure 5.16: Parallel MZI experimental results in air with a temperature ramp.

5.2.6 Discussion

Not only does simulation provide insight into what the transmission of light coupled to a microcavity and passed through an interferometer should look like for various physical parameters, it also serves another purpose in this work. When the transmission spectrum is sampled during attempts to detect binding events of nanoparticles, thousands of data samples are taken. Monitoring wavelength shifts between these samples would be a very tedious job; to make it easier, LSFs are made on the sampled data. The resonant wavelength of each transmission spectrum is obtained by an algorithm using the coefficients from the LSF, and then plotted as a function of the time the sample was taken. A LSF is never perfect as there is an error in the resonant wavelength it returns, and to characterize this error the LSFs can be performed on simulated data. By using simulated data, the resonant wavelength reported by the LSF can be directly compared to the resonant wavelength used in the simulation.

By characterizing the error of the returned resonant wavelength, the limits are to be determined for whether the LSF method of processing the data will be sufficient to distinguish individual binding events.

In order to find the limitations of the LSF method the minimum detectable resonant wavelength shift must be ascertained. The minimum detectable shift should be greater than three times the maximum error (for 3σ certainty) between the real resonant wavelength and the resonant wavelength the LSF fit returns. A convenient way to find this limit is to perform LSFs on simulated data with resonant frequencies that span a range that will result in their associated transmission dips to move over one full FSR, as was done in Figure 5.5. It is noted that the limit imposed by the LSF method depends on the physical parameters of the system, namely: the resolution between data points, and the systems SNR, the FSR and total Q. The physical parameters of the system were chosen to reflect the physical parameters obtained in experiments performed with the interferometer. The simulations also take into consideration the signal noise and the random fluctuations due to the laser jitter to as closely approximate a real experiment as possible.

From Figure 5.5 the maximum error of the fitted resonant wavelength is 0.1 fm. Using standard 3σ uncertainty for experiments, this means that the parallel reference interferometer can be used with a microsphere with experimental conditions similar to those given in Table 5.2.4 to detect binding events that create resonant wavelength shifts down to fractions of a femtometer.

Characterizing the system by heating up the microsphere is an effective and simple method to test for predicted phenomenon and ensure the LSF method is working. By looking at the experimental results in Figure 5.15, there is indication that the LSF is performing as would be expected. The resonant wavelength of the microsphere clearly increases as it is heated up, and it exhibits an exponential return as it is cooling off, a phenomenon explained in in Appendix B. The variance of the interferometer is relatively large for this experiment due to system instabilities, likely from a flaccid fiber taper.

To further illustrate the improvement of performance, an experiment measuring the resonant wavelength of the microsphere in buffer was performed, and the results are displayed in Figure 5.9. A microcavity loaded Q of 2.0×10^8 was observed in buffer. It is noted that these measurements were taken in the undercoupled regime, such that the loaded Q was close to the intrinsic Q of the microcavity. Furthermore, the measurements were performed on the upscan of the laser so it is possible that thermal broadening effects on the microcavity transmission are present. With experimental sensitivity for the conventional method at 2.1 fm and the parallel MZI method at 0.14 fm, the standard deviation of the resonant wavelength is reduced by a factor of 15 by correcting for the laser frequency jitter. It is noted that this sensitivity is for an experiment performed in buffer. An experiment with the presence of nanoparticles will have a decreased sensitivity due to the binding of particles to off equator locations resulting in increased resonant wavelength noise.

Discrepancies between the resonant wavelength signal from the interferometry method and conventional method could be due to a number of effects, possibly the wavelength drift of the laser, or changes to the optical path length of the interferometer. The drift only has an effect on the conventional method because the interferometer method does not use the scanning voltage as a reference, and changes to the interferometer path length would only effect measurements referencing the interferometer.

Chapter 6

Serial Reference Interferometry with a Microsphere

The next chapter further expands on interferometer experiments performed in [1] by introducing two different schemes which simplify the experimental set-up while maintaining an effective reference interferometer signal. Not only is the layout of the system more simple, but the power of these systems does not get split off. This is of benefit for experiments that require a large amount of optical power, including those on microcavity lasing [78–80] or thermo-optical broadening [81]. The first scheme, covered in the first section, is to have a serial MZI which reduces the set-up by a few components and prevents the laser signal from being split. The second scheme, covered in the second section, further simplifies the experimental set-up by replacing the MZI with a FPI which consists only of a fiber connector with physical contact (FC/PC) connectorized patch cord. It is noted here that all other connections besides those to the FPI are made with fiber connectors with angled physical contact (FC/APC).

In each section the experimental set-up is explained, and then the analytic equations of the system, in terms of voltage as would be seen on an oscilloscope, are derived. Next the modelling equation will be outlined for the LSF, with explicit expressions and initial guess determination procedure outlined for the fit coefficients. This is followed by simulation and fitting results, including a figure depicting the resonant wavelength fit error as the resonant wavelength of the simulated data is increased over one FSR of the interferometers. Each section includes a discussion on the results, and in the discussion of the serial MZI the result of a loss of information due to the specifics of the interferometer signal will be covered. This loss of information serves as motivation for the serial FPI, which has an interference signal which is more suited to serial configuration than that of the MZI. Because of the loss of data experienced with the serial MZI, no experiments are carried out. Instead experimental results are obtained and discussed for the serial FPI case only.

6.1 Serial Mach-Zehnder Interferometer

6.1.1 Experimental Set-up

The set-up for the parallel MZI is depicted in 6.1 and a discussion follows. A waveform generator is used to scan a probe laser around 630 nm. The laser output travels via single-mode fiber through a polarization controller to a tapered location where the microsphere is positioned. Upon being coupled to a microsphere, the light is sent through the MZI, after which the light is detected by a BPD.

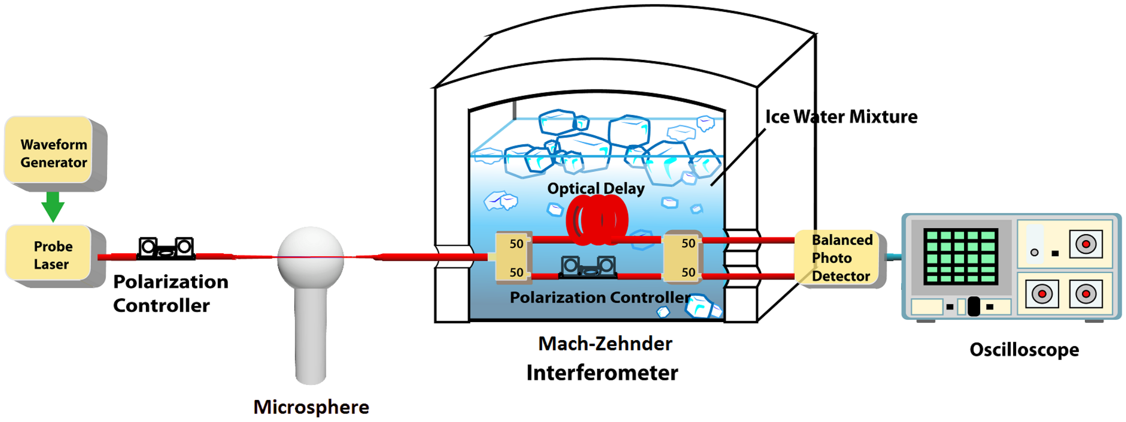

Figure 6.1: Serial MZI experimental set-up.

6.1.2 Analytic Equations of the System Output for Simulation of Experimental Data

The monitoring of each system happens on an oscilloscope, which requires the optical power transmission to first be converted to an electrical signal. To find the two port output powers of the coupled microcavity with serial interferometer, first consider the eletric field outputs of the MZI, as given in Equation 3.13, where the input electric field is the output electric field from the coupled microsphere, given in Equation 3.5:

$$\begin{aligned} E_{out1}(\nu_L) &= jE_{in}\left(1 - \frac{2\delta_c}{\delta_0 + \delta_c + j\Delta\omega}\right) sin\left(\frac{\pi\nu_L}{\Delta\nu_{FSR}}\right) \\ E_{out2}(\nu_L) &= jE_{in}\left(1 - \frac{2\delta_c}{\delta_0 + \delta_c + j\Delta\omega}\right) cos\left(\frac{\pi\nu_L}{\Delta\nu_{FSR}}\right). \end{aligned} \tag{6.1}$$

The output powers are the complex conjugate of the above fields:

$$\begin{aligned} P_{out1}(\nu_L) &= P_{in}\left(1 - \frac{4K}{(1+K)^2 + \frac{2Q_0}{\nu_L^2}(\nu_R - \nu_L)^2}\right) sin^2\left(\frac{\pi\nu_L}{\Delta\nu_{FSR}}\right) \\ P_{out2}(\nu_L) &= P_{in}\left(1 - \frac{4K}{(1+K)^2 + \frac{2Q_0}{\nu_L^2}(\nu_R - \nu_L)^2}\right) cos^2\left(\frac{\pi\nu_L}{\Delta\nu_{FSR}}\right), \end{aligned} \tag{6.2}$$

where P_{in} is the input power from the laser. Furthermore, in order to measure the optical signal on the oscilloscope, it must be converted to an electrical signal using a two port BPD. The BPD subtracts one output signal from the other, which has the benefit of reducing noise from the laser. The subtracted outputs are then converted to a voltage by the BPD. The output voltage for this system will be given by the following, where G_{BPD} is the transimpedance amplifier gain of the BPD in volts per Ampére, and $\mathscr{R}_{BPD}$ is noted as being the responsivity of the BPD with units of Ampéres per Watt:

$$V_{out}(\nu_L) = G_{BPD}\mathscr{R}_{BPD}(P_{out2}(\nu_L) - P_{out2}(\nu_L)). \tag{6.3}$$

Defining the serial MZI output voltage amplitude,

$$V_{MZI} = G_{BPD}\mathscr{R}_{BPD}P_{in}, \tag{6.4}$$

the output voltage can be expressed as

$$V_{out}(\nu_L) = V_{MZI}\left(1 - \frac{4K}{(1+K)^2 + \frac{2Q_0}{\nu_L^2}(\nu_R - \nu_L)^2}\right) cos\left(\frac{2\pi\nu_L}{\Delta\nu_{FSR}}\right). \tag{6.5}$$

This expression is the governing equation for the trace that is obtained with an oscilloscope from a serial MZI with coupled microcavity. It is a Lorentzian dip enveloping a sinusoidal function. If the FSR of the interferometer and the Q-factor of the microcavity are sufficiently large, the Lorentzian dip should easily be observable. However, there is a problem inherent to using this interferometer due to the zero value of the sinusoid. If the Lorentzian dip occurs at or around these zero points, there is a loss of information. The results of this will be apparent in the results of the simulation. See Figure 6.2 for a plot of data simulated with this expression.

When the transmission is measured on an oscilloscope the dependent variable is time. In order to achieve this with the analytical equations, one must consider the intricacies of the experimental set-up. The pump laser is swept with a frequency modulating voltage signal to achieve a laser frequency that changes linearly over time. The exact conversion factor is dependent on the laser, and it will be referred to as the laser scan rate, S_ν, which has units of Hertz per second. To make Equation 6.5 into a time dependent signal, it must be made to incorporate the laser scan rate. This is done by changing the parameters involving the laser frequency, as follows: replace the laser frequency ν_L with $\nu_L = S_\nu(t - t_0) + \nu_{L0}$, where S_ν is the scan rate, t_0 is the zero point of the frequency modulation, and ν_{L0} is the central operating frequency of the laser. In the case of the serial MZI Equation 6.5 becomes:

$$\begin{aligned} V_{out}(t) &= V_{MZI}\left(1 - \frac{4K}{(1+K)^2 + \frac{2Q_0}{(S_\nu(t-t_0)+\nu_{L0})^2}(S_\nu(t-t_0)+\nu_{L0}-\nu_R)^2}\right)\ldots \\ &\ldots\ cos\left(\frac{2\pi(S_\nu(t-t_0)+\nu_{L0})}{\Delta\nu_{FSR}}\right). \end{aligned} \tag{6.6}$$

6.1.3 Least Squares Fit

The task, now that the simulation equation has been outlined, is to develop a modelling equation for a LSF. The modelling equation will consist of the functional form as found in Equation 6.6, with various coefficients to be optimized by the fitting algorithm. In the following subsections there will be an outline of the modelling equation where the coefficients are introduced and written in terms of the physical properties of the system. The significance of the coefficients in terms of their impact on the fitting curve is explained, and signal processing methods are developed to automatically generate initial guess values for the coefficients. An important part of performing a LSF is to provide the fit an initial guess for all of the coefficients, as this guess serves as a starting point for the procedure. By choosing an appropriate starting point the time required for the fit to be completed can be kept to a minimum. Finally some fits are performed on simulated data, and their errors are examined. From the results it will be seen that the MZI is not a good choice for a serial connected interferometer.

Modelling Equation and Coefficients

The equation used to perform the LSF on the MZI system is given by

$$V_{out}(t) = V_0 \left(1 - \frac{I\gamma^2}{\gamma^2 + (t-d)^2}\right) cos(b(t-c)). \tag{6.7}$$

The coefficients, by matching Equation 6.6 to Equation 6.7, can be expressed in terms of the physical parameters as follows:

$$V_0 = V_{MZI}, \tag{6.8}$$

$$b = \frac{2\pi S_\nu}{\Delta\nu_{FSR}}, \tag{6.9}$$

$$c = t_0 - \frac{\nu_{L0}}{S_\nu}, \tag{6.10}$$

$$I = \frac{4K}{(1+K)^2}, \tag{6.11}$$

$$\gamma = \frac{\nu_{L0}(1+K)}{2Q_0 S_\nu}, \tag{6.12}$$

and

$$d = t_0 + \frac{\nu_R - \nu_{L0}}{S_\nu}. \tag{6.13}$$

How the Coefficients determine the shape of the Curve, and Signal Processing Techniques for Automatic Coefficient Guessing

By inspecting Equation 6.7 one can arrive at the following conclusions about the fitting coefficients. The amplitude of the sinusoidal signal is coefficient ‘V_0’, coefficients ‘b’ and ‘c’ describe the frequency of oscillation and phase of the sinusoid, respectively. Coefficient ‘I’ is the amplitude of the Lorentzian dip, and lastly coefficients ‘γ’ and ‘d’ correspond to the HWHM and location of the Lorentzian dip, again in their respective order. These coefficients are plotted in Figures 5.3 and 5.4 in context of simulated data for the case of the parallel MZI. The only difference between the serial and parallel coefficients is that the amplitude coefficient of the serial interferometer is a combination of both amplitudes in the parallel case.

The start point coefficients are generated as follows. The amplitude, coefficient 'V_0', is taken to be half of the difference between the voltage signal maximum and minimum. Coefficient 'b', the frequency, is obtained by finding the relative time difference between the first two points where the signal approaches zero. When the signal is noisy there is likely to be many zero crossings around the point the sinusoid goes to zero. To get around this, the signal is smoothed with a moving average. The time difference between two zero crossings of the smoothed signal corresponds to half of the period, which in turn, yields the frequency. In order to find the frequency normalized phase shift, coefficient 'c', the first crossing in time where the smoothed signal goes from being a negative to positive value is determined. $V_{out}(t)$ follows a cosine function, so this crossing corresponds to a $\frac{\pi}{2}$ phase advance. The coefficient can thus be approximated as the time of the crossing advanced by $\frac{\pi}{2b}$ and delayed by half the time range.

In order to determine the remaining coefficients, a difference signal is constructed by finding the difference between each point of the smoothed voltage signal. The index location of the Lorentzian dip is obtained by finding the zero point of the difference signal which has the minimum voltage magnitude. Coefficient 'I', the amplitude of the Lorentzian dip, can be obtained by finding the ratio of the voltage at the Lorentzian dip point to the maximum voltage. The HWHM of the Lorentzian signal, coefficient 'γ', is approximated by finding half of the time difference between the consecutive zero points of the difference signal about the Lorentzian dip location. Lastly, to determine the time location of the Lorentzian dip, coefficient 'd', the index location of the zero point of the difference signal which has the minimum voltage magnitude is converted to a time value.

To further enhance the accuracy of the LSF, three fits are performed. The first fit has a reduced time span focusing on the first part of the signal which is dominated by the sinusoid. This allows for an accurate sinusoidal amplitude, frequency, and phase to be determined. The second fit uses the coefficients from the first fit as an initial guess, but uses a full time span to also fit the Lorentzian part of the signal. The third fit again uses a reduced time span that is centered around the time value of coefficient 'd' calculated from the second fit. The time span is chosen to adequately focus in the Lorentzian dip area so an accurate value of the resonant location, width,

Parameter	Value
Resolution	40 ns
Total Q	5×10^7
Resonant Wavelength	635.5 nm
FSR	36.1 MHz
Signal Amplitude	1 V
Scan Rate	1.0×10^{12} Hz/s
SNR	25

Table 6.1: Serial MZI simulation parameters.

and amplitude can be obtained. The coefficients used for calculating the resonant shift is an amalgamation of the coefficients determined from the various fits in order to obtain the most accurate result.

Simulation and Fitting Results

The LSF was performed on data simulated with Equation 6.6 using the physical parameters listed in Table 6.1.3. The fit is compared to simulated data in Figure 6.2, and the resonant wavelength error is displayed in Figure 6.3

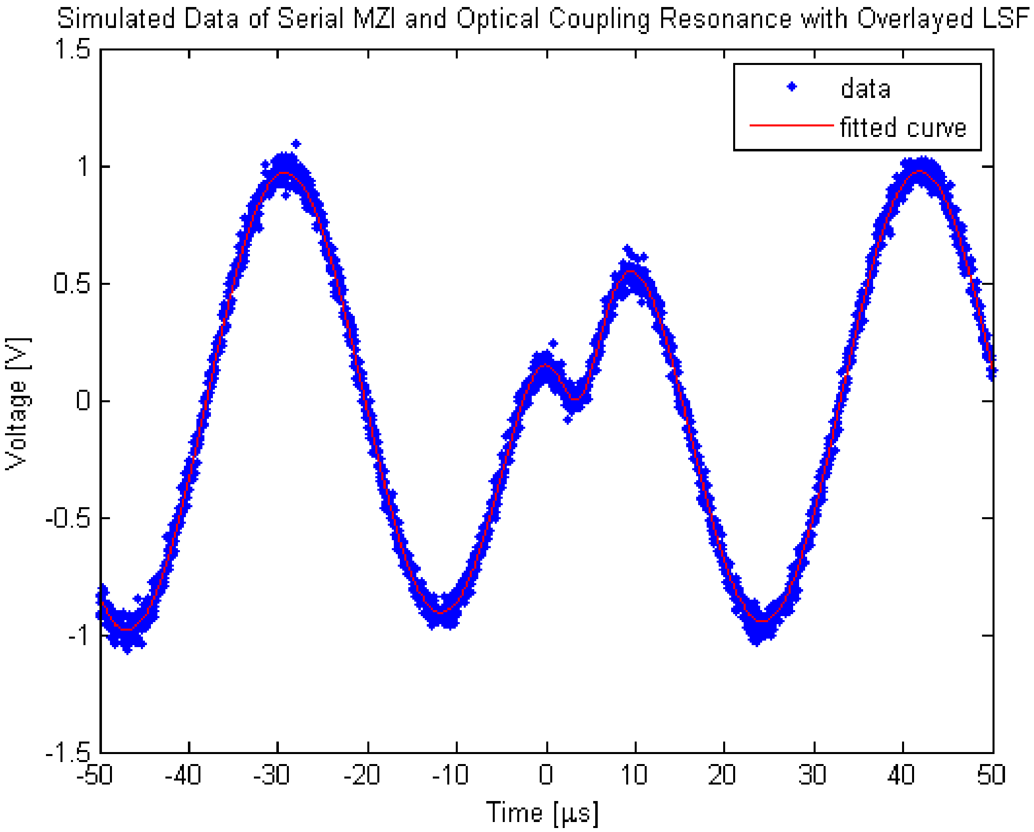

Figure 6.2: Serial MZI simulation and LSF results.

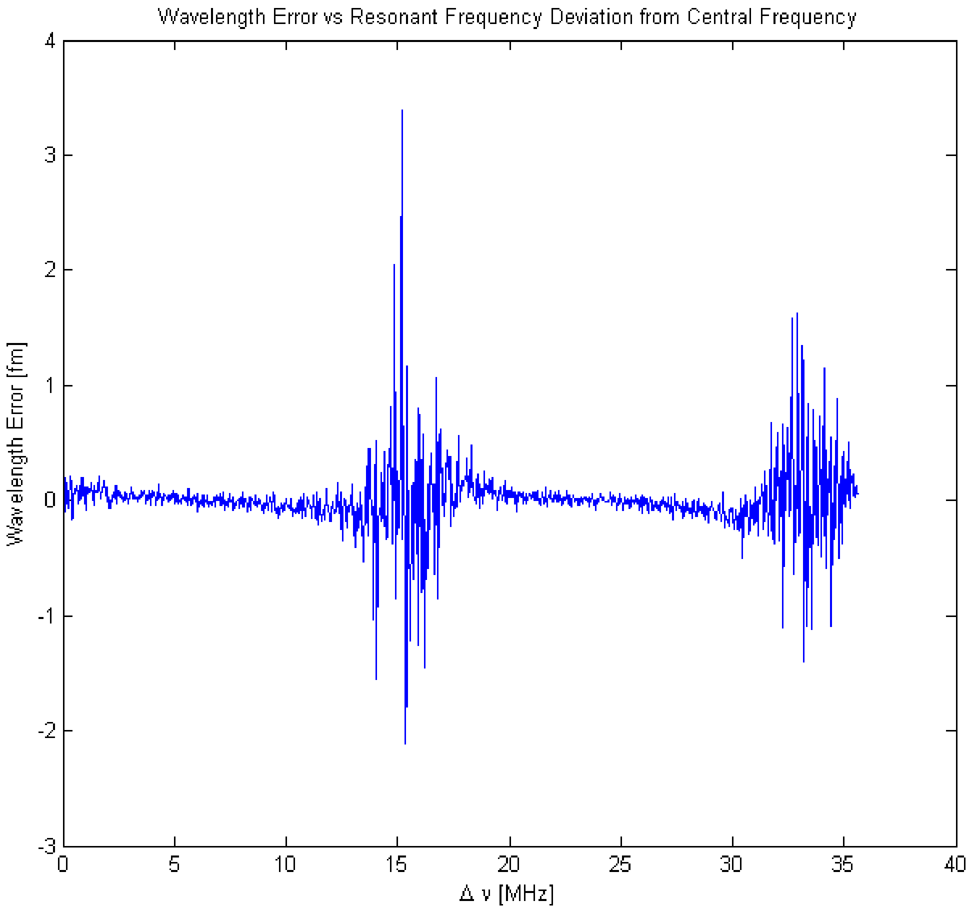

Figure 6.3: Serial MZI simulation resonant wavelength error.

To show how the SNR of the system output effects the returned wavelength error, the wavelength error is plotted as a function of SNR in Figure 6.4. Here the resonant wavelength is fixed, and the only thing that varies is the SNR. The data is generated using the physical parameters given in Table 6.1.3. Because the noise is randomly generated, 20 data points are plotted for each SNR with a 3σ envelope shown in red.

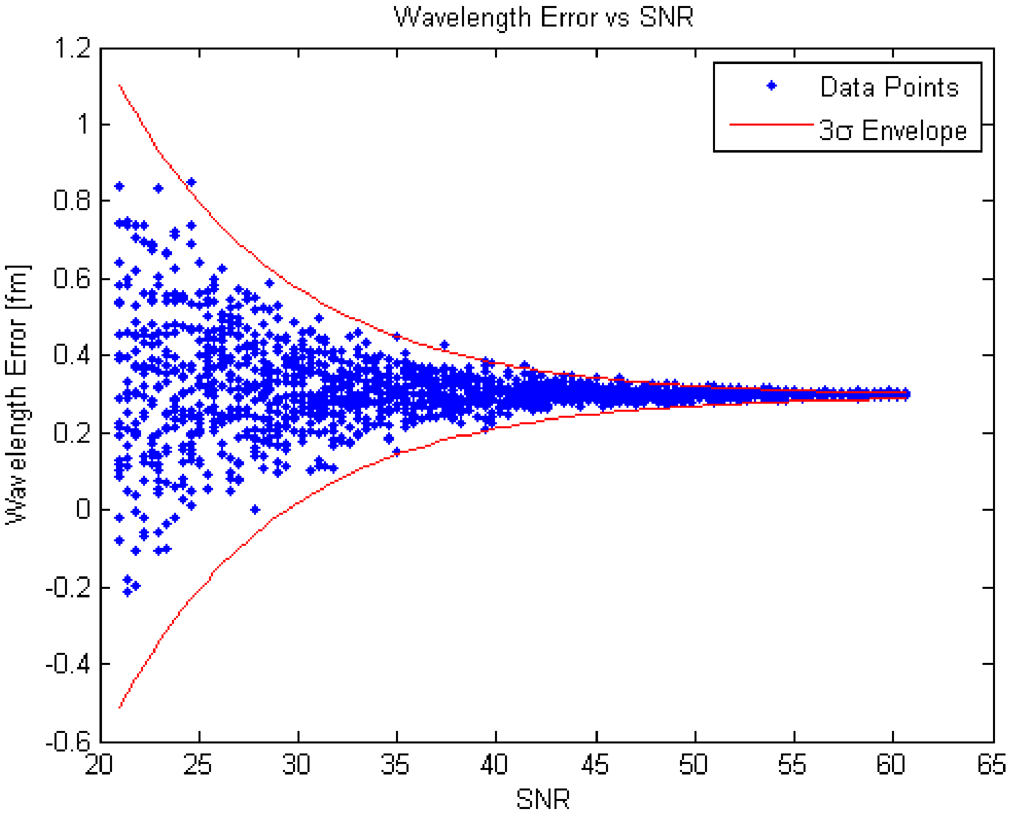

Figure 6.4: Serial MZI simulation of resonant wavelength error vs SNR.

6.1.4 Discussion

It was mentioned after the derivation of the analytical expression for the voltage transmission that there would be a loss of information if the resonant wavelength of the microcavity was in proximity to the MZI sinusoidal zero point. This problem is apparent from Figure 6.3 where there is a clear jump in the resonant wavelength error near the point $\Delta\nu = 15$MHz. This location was confirmed to be the location of the sinusoidal zero point by both plotting the phase angle corresponding to the location of the resonant dip, and plotting the simulated data at this point. Because of this zero point, the sensing limitation of the MZI for a system with physical parameters given in Table 6.1.3 is for resonant wavelength shifts that can be detected with a 0.94 fm 3σ uncertainty. In the following section the serial connected FPI is introduced. From Equation 3.20 one can see that the FPI power transmission does not have a true sinusoidal functional output, but rather is governed by an Airy function. This leads to the possible detection of smaller wavelength shifts due to the fact that the transmission of the FPI signal does not go to zero. For this reason the MZI is ruled out as a good choice for a serial connected interferometer, and attention is now shifted to the serial connected FPI.

6.2 Serial Fabry-Pérot Interferometer

6.2.1 Experimental Set-up

The serial FPI set-up is much more convenient than that of the serial or parallel MZI. A probe laser is scanned with a function generator, passes through a polarization controller, and is coupled to a microsphere. After the light has been coupled to the microsphere, it travels by fiber optic cable to the Fabry-Pérot cavity. The cavity consists of two fiber connector physical connection (FC/PC) connectors connected in-line with the optical fiber coupled from a microcavity, as seen in Figure 6.5. The connectors are not completely tightened so that there is an air interface between the interferometer and the adjacent optical fibers. Finally, the transmitted signal from the FPI is measured by a PD.

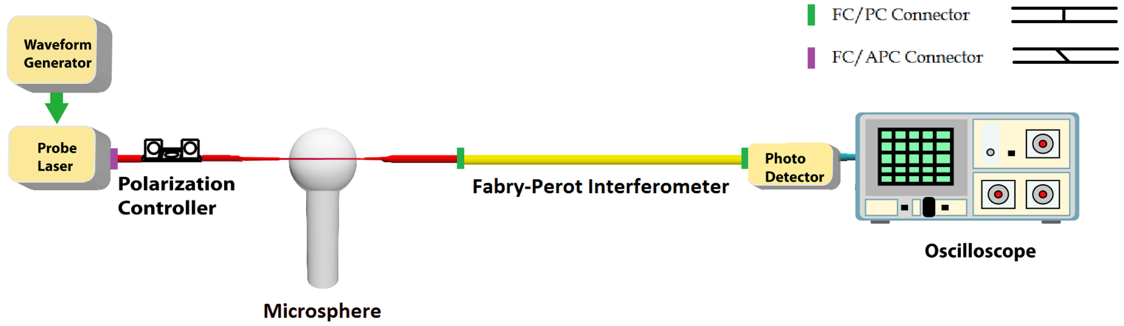

Figure 6.5: Serial FPI experimental set-up.

6.2.2 Analytic Equations of the System Output for Simulation of Experimental Data

The output electric field is first obtained by combining Equations 3.5 and 3.17. The input electric field to the interferometer is the output electric field of the coupled microcavity, such that the output field of the serial FPI system, E_{out}, in terms of the input field to the coupled microsphere, E_{in}, is:

$$E_{out}(\nu_L) = E_{in}\left(1 - \frac{2\delta_c}{\delta_0 + \delta_c + j\Delta\omega}\right)\frac{t_E t'_E e^{j\delta}}{1 - r'^2_E e^{2j\delta}}. \tag{6.14}$$

The power is obtained by multiplying the output electric field by its complex conjugate:

$$P_{out}(\nu_L) = P_{in}\left(1 - \frac{4K}{(1+K)^2 + \frac{2Q_0}{\nu_L^2}(\nu_R - \nu_L)^2}\right)\frac{1}{1 + Fsin^2(\frac{\pi\nu_L}{\Delta\nu_{FSR}} + \phi_{r'})}. \tag{6.15}$$

The equation governing the voltage photodetected from the serial Fabry-Pérot cavity with coupled microcavity is obtained with the following equation. Here G_{PD} is the transimpedance amplifier gain of the PD in volts per Ampére, $\mathscr{R}_{PD}$ is the responsivity of the PD with units of Ampéres per Watt, P_{out} is the output power coupled from the microcavity and transmitted through the Fabry-Pérot cavity.

$$V_{out}(\nu_L) = G_{PD}\mathscr{R}_{PD}P_{out}(\nu_L) \tag{6.16}$$

$$V_{out}(\nu_L) \quad = \quad V_{FPI}\left(1 - \frac{4K}{(1+K)^2 + \frac{2Q_0}{\nu_L^2}(\nu_R - \nu_L)^2}\right)\frac{1}{1 + Fsin^2(\frac{\pi\nu_L}{\Delta\nu_{FSR}} + \phi_{r'})} \tag{6.17}$$

where

$$V_{FPI} = G_{PD}\mathscr{R}_{PD}P_{in}. \tag{6.18}$$

When the transmission is measured on an oscilloscope the dependent variable is time. In order to achieve this with the analytical equations, one must again consider the intricacies of the experimental set-up. The pump laser is swept with a frequency modulating voltage signal to achieve a laser frequency that changes linearly over time. The exact conversion factor is dependent on the laser, and it will be referred to as the laser scan rate, S_ν, which has units of Hertz per second. To make Equation 6.17 into a time dependent signal, it must be made to incorporate the laser scan rate. This is done by changing the parameters involving the laser frequency, as follows: replace the laser frequency ν_L with $\nu_L = S_\nu(t - t_0) + \nu_{L0}$, where S_ν is the scan rate, t_0 is the zero point of the frequency modulation, and ν_{L0} is the central operating frequency of the laser. In the case of the serial FPI Equation 6.17 becomes:

$$\begin{aligned} V_{out}(t) &= V_{FPI}\left(1-\frac{4K}{(1+K)^2+\frac{2Q_0}{(S_\nu(t-t_0)+\nu_{L0})^2}(S_\nu(t-t_0)+\nu_{L0}-\nu_R)^2}\right)\cdots \\ &\cdots \frac{1}{1+Fsin^2\left(\frac{\pi(S_\nu(t-t_0)+\nu_{L0})}{\Delta\nu_{FSR}}+\phi_{r'}\right)}, \end{aligned} \tag{6.19}$$

This final expression is the governing equation for the trace that is obtained with an oscilloscope from a serial FPI with coupled microcavity. It is simply a Lorentzian dip multiplied with an Airy function. If the FSR of the interferometer and the Q-factor of the microcavity are sufficiently large, the Lorentzian dip should easily be resolved. See Figure 6.6 for a plot of data simulated with this expression and physical parameters given in Table 6.2.3.

6.2.3 Least Squares Fit

The task, now that the simulation equation has been outlined, is to develop a modelling equation for a LSF. The modelling equation will consist of a functional form as found in Equation 6.19, with various coefficients to be optimized by the fitting algorithm. In the following subsections there will be an outline of the modelling equation where the coefficients are introduced and written in terms of the physical properties of each system. The significance of the coefficients in terms of their impact on the fitting curve is explained, and signal processing methods are developed to automatically generate initial guess values for the coefficients. Finally some fits are performed on simulation data, and their errors are examined in order to understand the limits of the fitting procedure when it is used to measure wavelength shifts.

Modelling Equation and Coefficients

The equation used to perform the LSF on the FPI system is given by

$$V_{out}(t)=V_0\left(1-\frac{I\gamma^2}{\gamma^2+(t-d)^2}\right)\frac{1}{1+Fsin^2(b(t-c))}. \tag{6.20}$$

The coefficients, by matching Equation 6.20 to Equation 6.19, can be expressed in terms of the physical parameters as follows:

$$V_0 = V_{FPI}, \tag{6.21}$$

$$F = \frac{4R}{(1-R)^2}, \tag{6.22}$$

$$b = \frac{\pi S_\nu}{\Delta\nu_{FSR}}, \tag{6.23}$$

$$c = t_0 - \frac{\nu_{L0}}{S_\nu} - \frac{\Delta\nu_{FSR}\phi_{r'}}{\pi S_\nu}, \tag{6.24}$$

$$I = \frac{4K}{(1+K)^2}, \tag{6.25}$$

$$\gamma = \frac{\nu_{L0}(1+K)}{2Q_0 S_\nu}, \tag{6.26}$$

and

$$d = t_0 + \frac{\nu_R - \nu_{L0}}{S_\nu}. \tag{6.27}$$

How the Coefficients determine the shape of the Curve, and Signal Processing Techniques for Automatic Coefficient Guessing

By inspecting Equation 6.20, in a similar manner as was done in the previous section, one can arrive at the following conclusions about the fitting coefficients. The maximum of the Airy signal is coefficient 'V_0', and coefficient 'F' is the coefficient of finesse, which determines the Airy signal minimum. Coefficients 'b' and 'c' describe the analogues of frequency and phase of the Airy signal, respectively. Coefficient 'I' is the amplitude of the Lorentzian dip, and lastly coefficients 'γ' and 'd' determine the HWHM and location of the Lorentzian dip, again in their respective order. These coefficients are plotted in Figure 6.6 in context of simulated data.

The start point coefficients are generated in a similar manner as was done for the MZI. The amplitude, coefficient 'V_0', is taken to be the signal maximum. Coefficient 'F', the coefficient of finesse, is obtained by solving the Airy transmission function for the coefficient of finesse at the time when the sinusoidal term is at its maximum (i.e. equal to one). Approximating the signal amplitude to be the maximum of the smoothed voltage signal, and only considering the first section of the trace which is dominated by the Airy function, coefficient 'F' is the ratio of the voltage maximum minus the voltage minimum over the voltage minimum. To obtain the analogues of the frequency and phase of the Airy signal the location of the first and second peak of the Airy signal is obtained. In order to do this the difference function of the voltage signal is obtained, and then the first two crossings where the difference goes from positive to negative are found. The time between the crossings is used as half of the period, to obtain a guess of the frequency, coefficient 'b'. The phase shift normalized for frequency, coefficient 'c', is guessed to be the time to the first Airy maximum, which is the first negative crossing of the difference function delayed by half the time range. Coefficient 'I', the Lorentzian amplitude, is obtained by taking the difference between the mean and minimum of the signal, and normalizing over the mean.

In order to determine coefficient 'γ', the HWHM, a square error signal is created. This signal is generated by taking the square of the departure of the smoothed signal from an Airy signal generated from the previously obtained fit coefficients, 'V_0', 'F', 'b', and 'c'. Coefficient 'γ' is obtained by finding half of the time difference between the two points where the error signal is at a quarter of its maximum. Due to the error being squared, the quarter maximum points correspond to the points of half maximum of the unsquared signal. Lastly, to determine the time location of the Lorentzian dip, coefficient 'd', the location of the voltage signal minimum is obtained.

Again, to further enhance the accuracy of the LSF, three fits are performed. The first fit has a reduced time span focusing on the first part of the signal which consists of the Airy function dominated part. This allows for accurate Airy function amplitude, coefficient of finesse, and the frequency and phase analogues to be determined. The second fit uses the coefficients from the first fit as an initial guess, but uses a full time span to also fit the Lorentzian part of the signal. The third fit again uses a reduced time span that is centered on the time value of coefficient 'd' calculated from the second fit. The time span is chosen to adequately focus in the Lorentzian dip area so an accurate value of the resonant location, width, and amplitude can be obtained. Again, the coefficients used for calculating the resonant shift is an amalgamation of the coefficients determined from the various fits in order to obtain the most accurate result.

Simulation Results

The LSF was performed on data simulated with Equation 6.19 using the physical parameters listed in Table 6.2.3. The fit is compared to simulated data in Figure 6.6, and the resonant wavelength error is displayed in Figure 6.7

Parameter	Value
Resolution	80 ns
Total Q	5×10^7
Resonant Wavelength	635.5 nm
FSR	49.6 MHz
Signal Amplitude	1 V
Scan Rate	1.0×10^{12} Hz/s
Coefficient of Finesse	0.251
SNR	25

Table 6.2: Serial FPI simulation parameters.

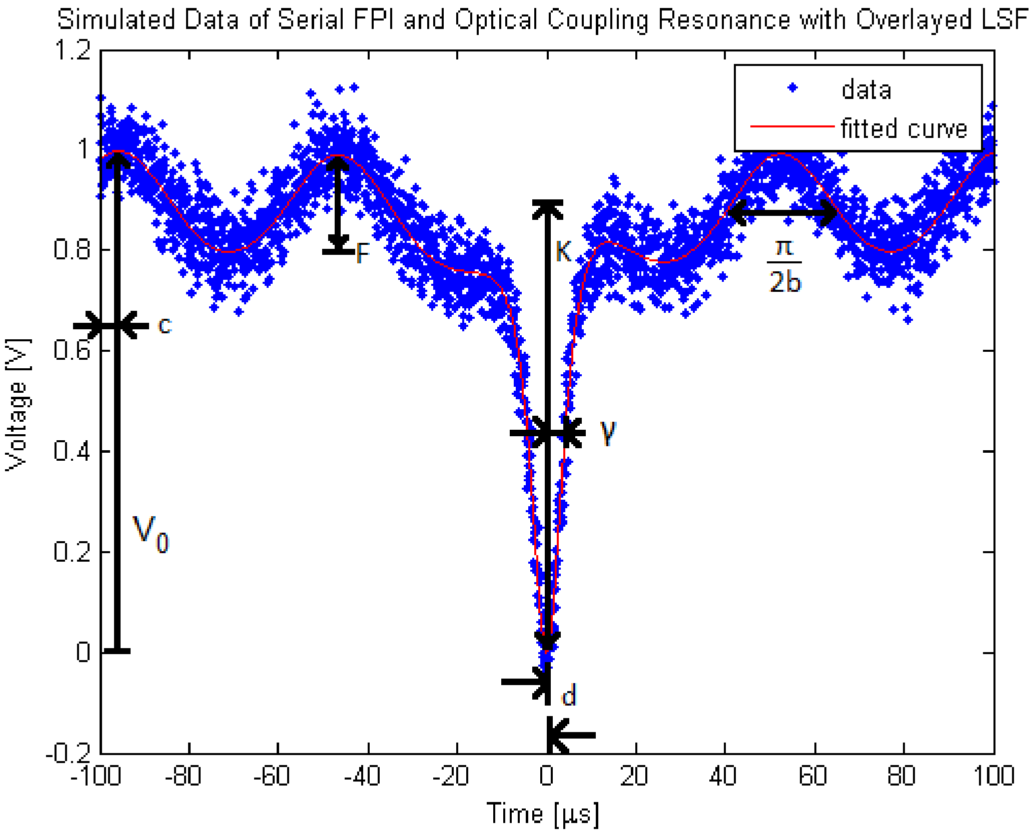

Figure 6.6: Serial FPI simulation and LSF results.

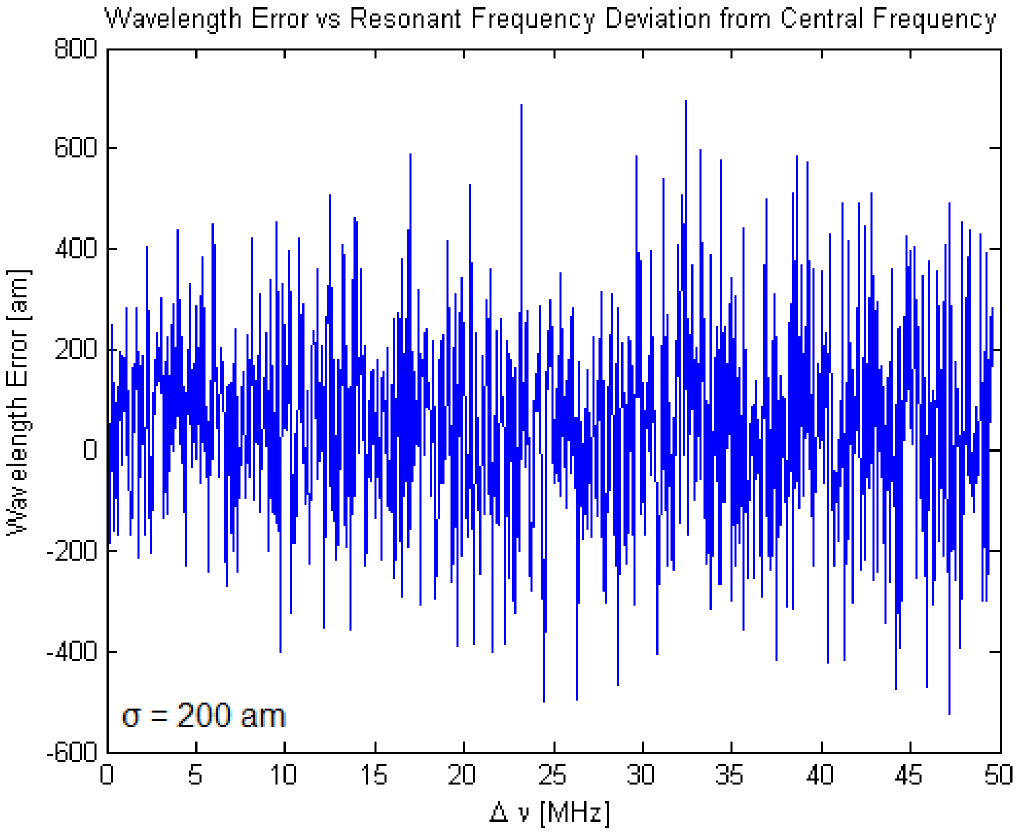

Figure 6.7: Serial FPI simulation resonant wavelength error.

To show how the SNR of the system output effects the returned wavelength error, the wavelength error is plotted as a function of SNR in Figure 6.8. Here the resonant wavelength is fixed, and the only thing that varies is the SNR. The data is generated using the physical parameters given in Table 6.2.3. Because the noise is randomly generated, 20 data points are plotted for each SNR with a 3σ envelope shown in red.

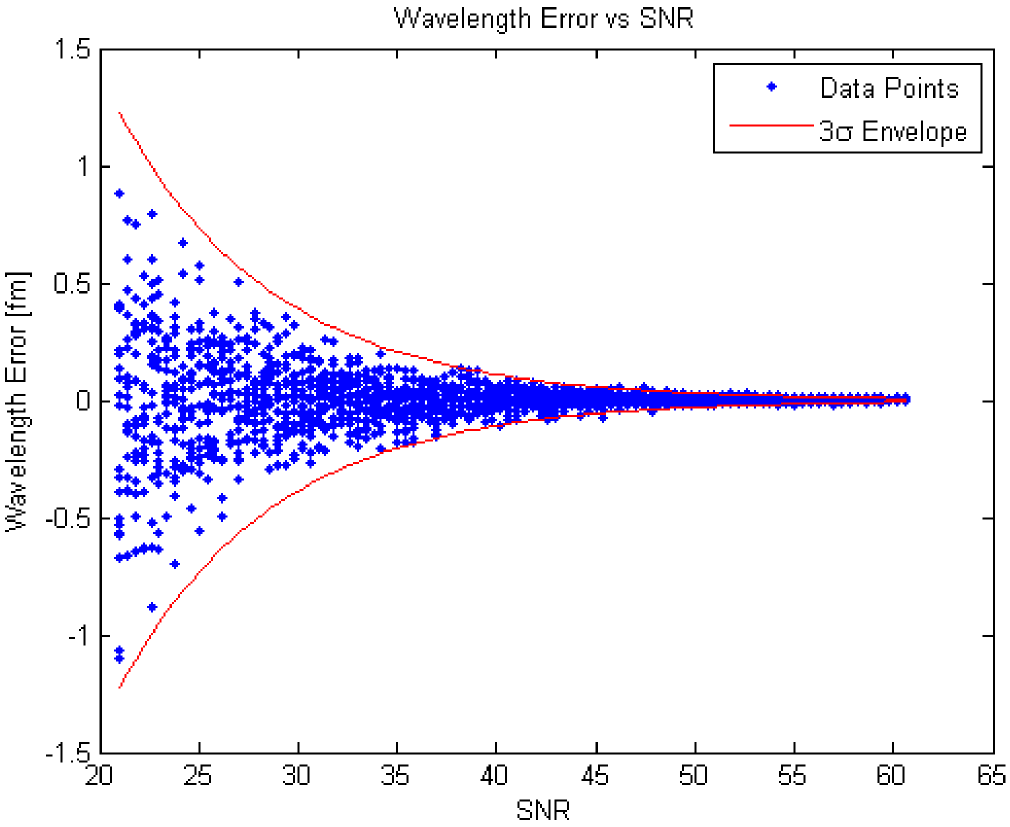

Figure 6.8: Serial FPI simulation of resonant wavelength error vs SNR.

6.2.4 Experimental Results

Experiments performed with the serial interferometers follow the same procedures listed in Section 5.2.5.

The result of the LSF performed on experimental data is plotted in Figure 6.9.

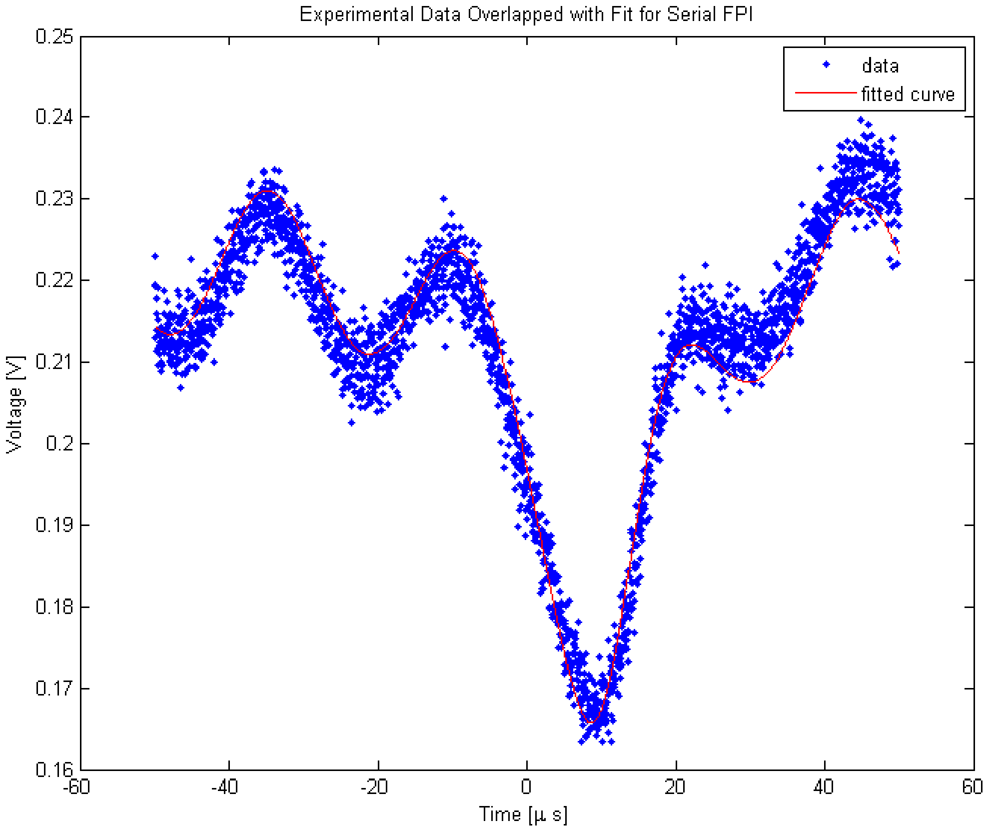

Figure 6.9: Serial FPI experimental data with fitting results.

An experiment was performed in a buffer solution to show the merits in correcting for the frequency jitter, it is displayed in Figure 6.10. Again, the blue trace corresponds to the resonant wavelength returned by the LSF after it has been corrected for laser jitter, and the grey trace indicates the resonant wavelength returned by the conventional method. In order to demonstrate the improvement on sensitivity for wavelength step detection, the variance of ten data points before and after each data point is obtained, added together, and turned into a standard deviation. This represents the uncertainty in wavelength if a step had occured at each data point. Before the variance is calculated, a three point average is taken over all the data. A plot of this experimental sensitivity is produced in Figure 6.11 for the conventional (grey) and interferometer method (blue). The experimental sensitivity of the fitted and jitter corrected resonant wavelength is 0.5 ± 0.2 fm, and the sensitivity of the resonant wavelength found with the conventional method is 11 ± 2 fm. The physical

Parameter	Value
Resolution	40 ns
Total Q	$(2.1 \pm 0.1) \times 10^7$
Resonant Wavelength	634.4±0.1nm
FSR	49.8 ± 0.2MHz
Laser Power	6.3 ± 0.1 mW
Scan Rate	$(4.0 \pm 0.1) \times 10^{12}$ Hz/s
Coefficient of Finesse	0.085±0.002
SNR	38

Table 6.3: Serial FPI experimental physical parameters.

parameters of this experiment are listed in Table 6.2.4

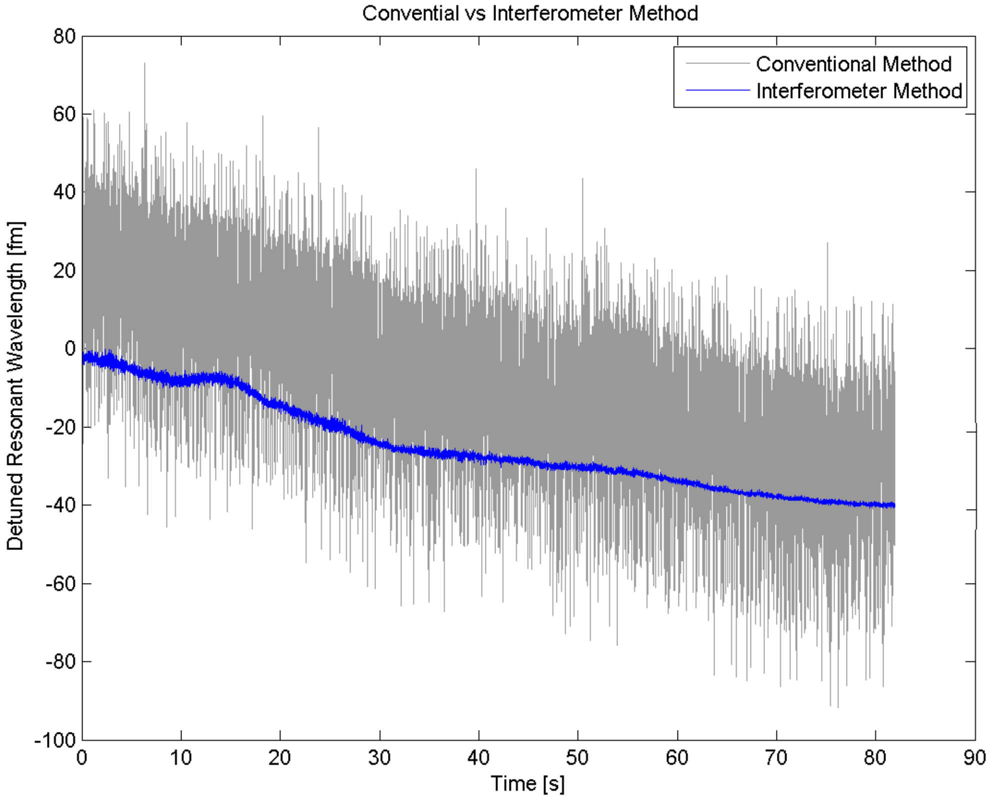

Figure 6.10: Serial FPI experimental results in buffer.

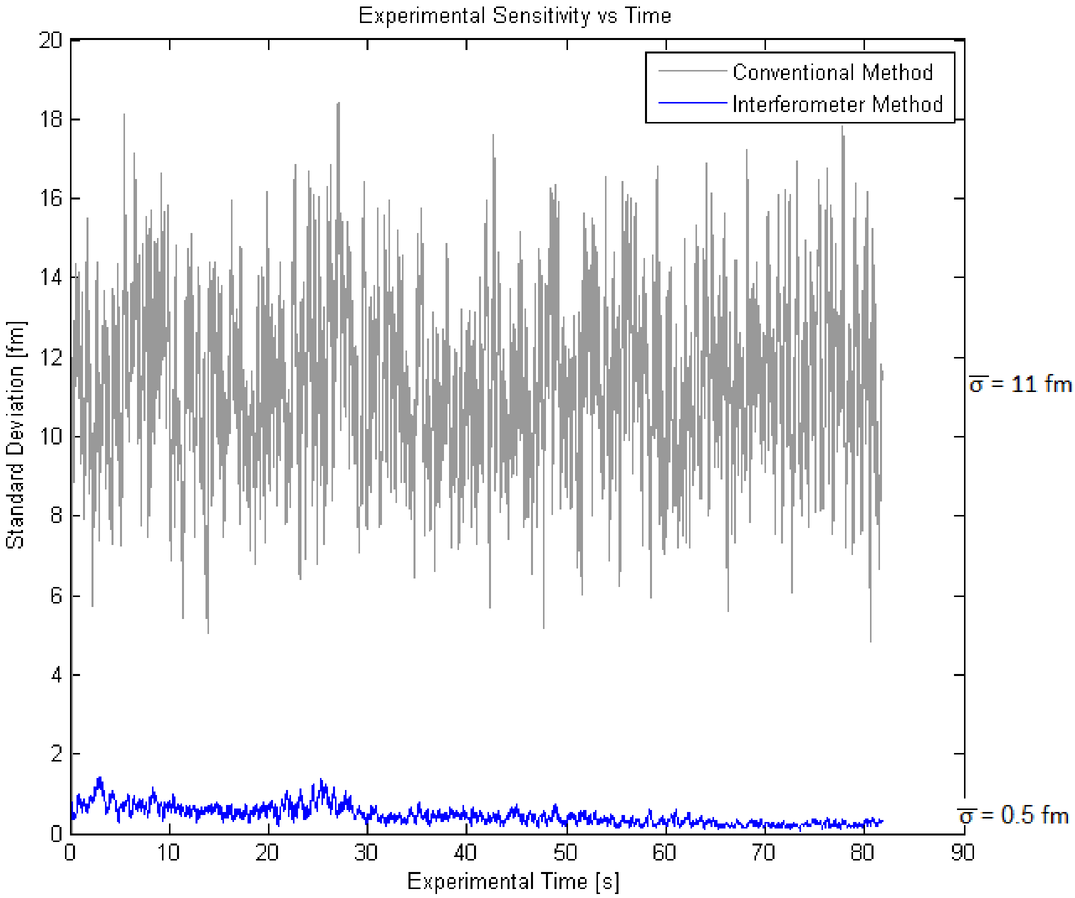

Figure 6.11: Serial FPI experimental sensitivity in buffer.

In order to demonstrate the effectiveness of the LSF performed on the buffer experiment, a comparison of the spectrograms of the experimental data and data fits is depicted in Figure 6.12. Each horizontal line in the spectrogram corresponds to one trace from the oscilloscope. Both axes correspond to time, the horizontal axis is the time corresponding to the oscilloscope trace, and the vertical axis corresponds to the experimental time, in other words, the relative time the trace was obtained. Furthermore, the effects of correcting for the laser jitter are demonstrated in Figure 6.13. In this image, each fitted data trace (or horizontal line) is shifted to keep the phase of the interferometer constant. By doing this, the jitter is effectively removed. Also included in Figure 6.14 is a spectrogram of the scanning voltage which as used to determine resonant wavelength the curve for the conventional method.

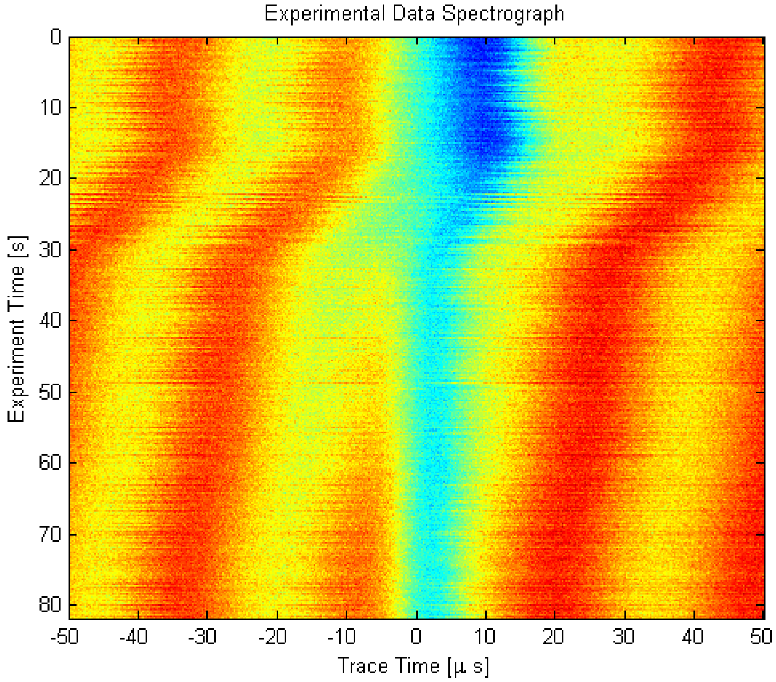

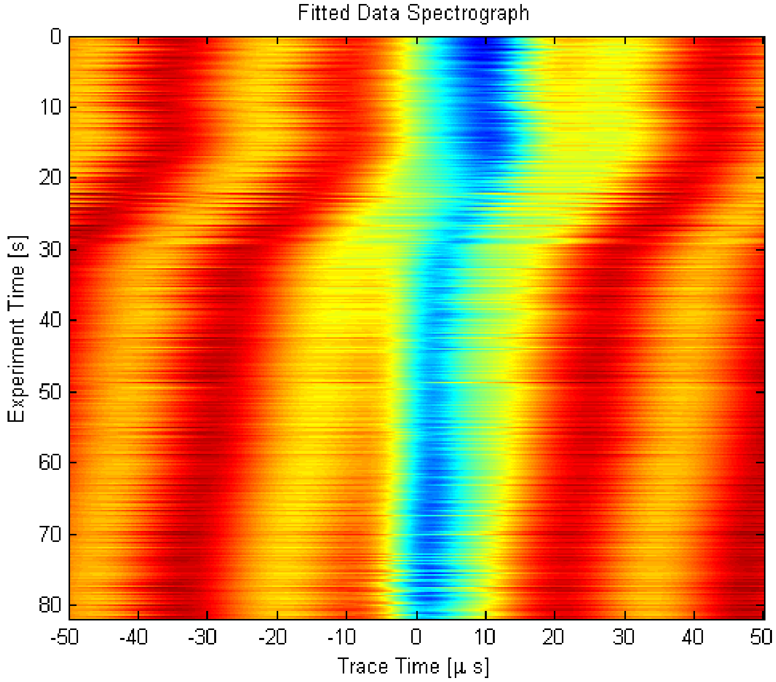

Figure 6.12: Serial FPI spectrograms of experimental data and fitting results.

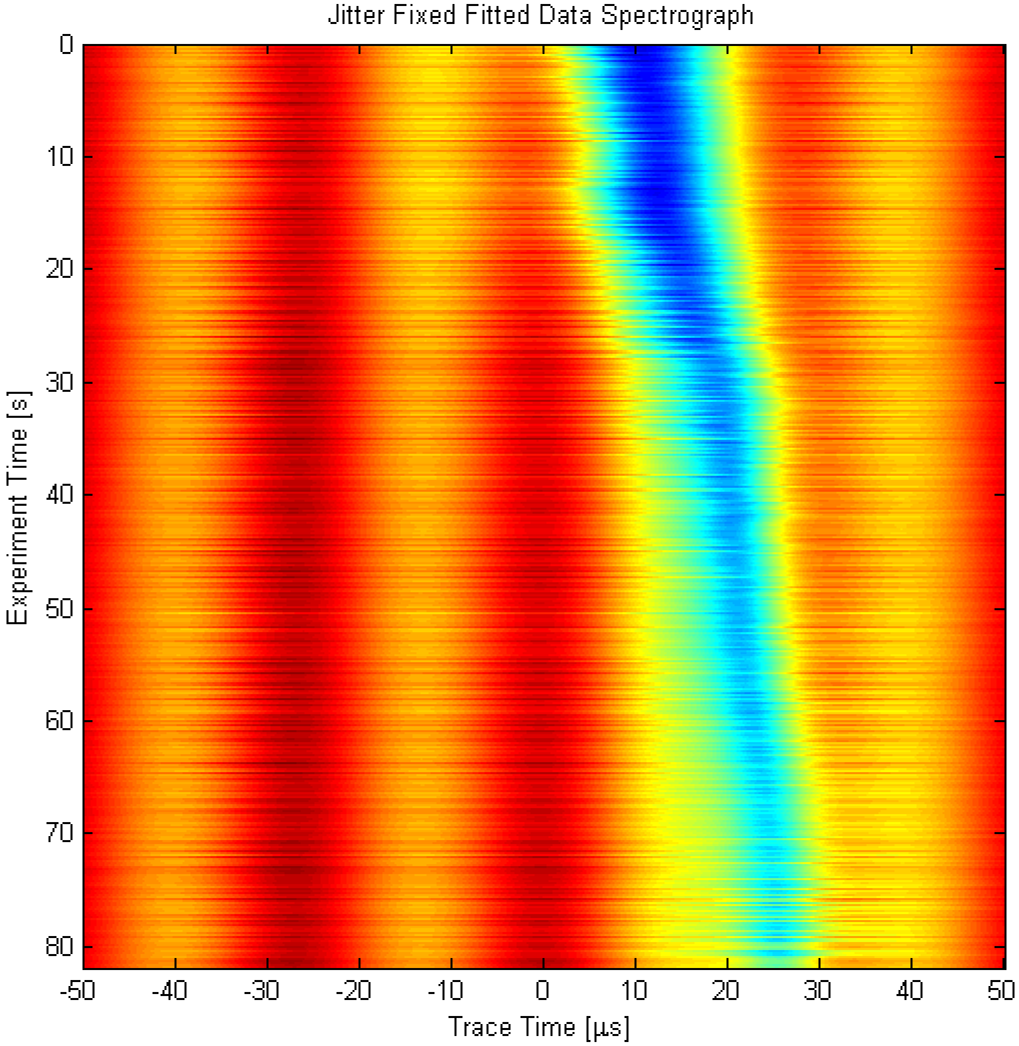

Figure 6.13: Serial FPI spectrogram of fitted experimental data corrected for laser jitter.

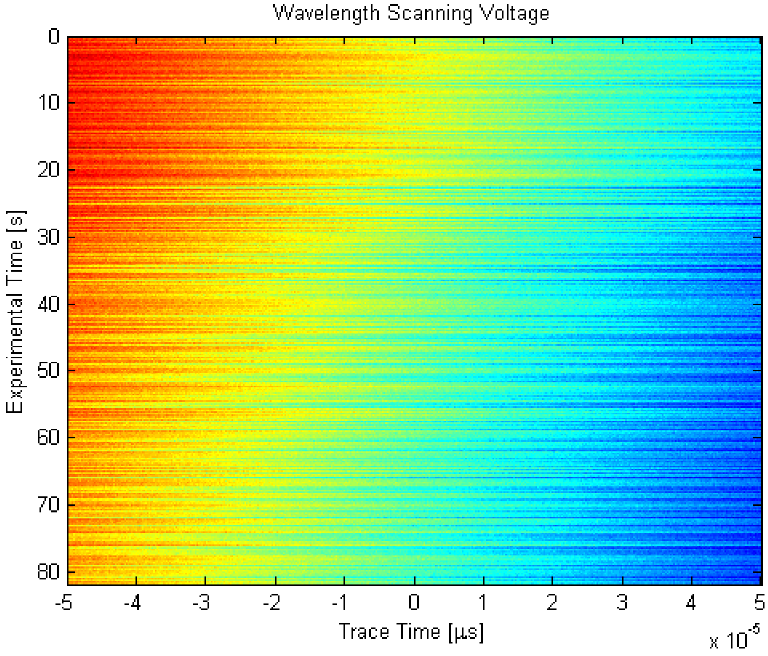

Figure 6.14: Serial FPI spectrogram of experimental data and fitting results: scanning voltage used for conventional method.

6.2.5 Discussion

As can be seen from the simulation and fitting results, the FPI is a much better choice to serve as a serial reference interferometer. The results of the serial MZI simulation and fitting yielded a measured wavelength shift error of 3.5 fm. This is much larger than the maximum wavelength shift error of 0.7 fm obtained with the serial FPI using similar physical parameters. This is nearly a five-fold reduction of error, and it is achieved with a much simpler experimental set-up. With a standard 3σ uncertainty, the serial FPI can be used with a microsphere and similar conditions to those in Table 6.2.3 to detect binding events that produce a resonant wavelength shift of 2.1 fm or larger.

To illustrate the improvement of performance, an experiment measuring the resonant wavelength of the microsphere in buffer was performed, and the results are displayed in Figure 6.10. With experimental sensitivity for the conventional method at 11 fm and the serial FPI method at 0.5 fm, the standard deviation of the resonant wavelength is reduced by over a factor of 20 by correcting for the laser frequency jitter. It is noted that this sensitivity is for an experiment performed in buffer. An experiment with the presence of nanoparticles will have a decreased sensitivity due to the binding of particles to off equator locations resulting in increased resonant wavelength noise.

Discrepancies between the resonant wavelength signal from the interferometry method and conventional method may arise due to temperature or mechanical instability of the interferometer. These instabilities are negligible because only short term resonant wavelength changes are needed for nanodetection applications.

Chapter 7

Conclusions and Future Work

7.1 Conclusions

In this thesis the versatility of reference interferometry for the determination of the laser frequency jitter corrected microcavity resonant wavelength across different platforms has been demonstrated. This was accomplished by using a parallel MZI set-up, as was done in [1] with a microtoroid, but with the use of a microsphere as the resonant cavity. It was shown that with a LSF method of fitting simulated data that nanoparticle binding induced resonant wavelength shifts of the microcavity larger than 0.3 fm can be detected with 3σ certainty, provided sufficient system stability. Furthermore, a reference interferometer has been implemented with a serial connection for the first time. It was shown that the MZI is not suitable for serial connection due to a loss of data that occurs about the interferometer's signal zero point. A serial FPI was shown to bypass this problem with an observed increase in sensitivity over the conventional resonant wavelength detection method that does not correct for laser frequency jitter. Furthermore, it was shown that a LSF method for fitting experimental data is capable of detecting nanoparticle binding induced wavelength shifts of the microcavity down to 2 fm, again with 3σ certainty.

Experimental results showed a microcavity resonant wavelength shift sensitivity of 0.14 fm for a parallel MZI set-up with a resonant cavity Q of 2.0×10^8 in a buffer solution. This represents a 15-fold reduction of uncertainty over conventional resonant wavelength determination methods. For the serial connected FPI set-up, a microcavity resonant wavelength standard deviation of 0.5 fm was recorded with a microcavity Q of 2.1×10^7. This represents a reduction of uncertainty of 20 times from the conventional resonant wavelength determination methods.

7.2 Future Work

To improve on the versatility of the LSF aspect of this work, modeling equations could be developed for experimental results obtained with a split mode. This would simply be implemented by adding a second Lorentzian dip to the functional form of the modelling equation(s), and by adding appropriate fitting coefficients.

In the future, work can be carried out to succesfully detect the binding of nanoparticles using the serial and parallel interferometry techniques discussed here. Furthermore, more complicated reference interferometer set-ups could be investigated, including the cascading of multiple interferometers with different FSRs in parallel. With this configuration, it would be possible to detect nanoparticles with different sizes. The interferometers with larger FSRs could be used to enhance detection of microcavity resonant wavelength shifts for larger amplitudes, while the interferometers would serve to enhance detection of smaller particles.

Bibliography

[1] T. Lu, H. Lee, T. Chen, S. Herchak, J-H. Kim, S. E. Fraser, R. C. Flagan, and K. Vahala. High sensitivity nanoparticle detection using optical microcavities. *Proceedings of the National Academy of Sciences*, 2011.

[2] B. Min, E. Ostby, V. Sorger, E. Ulin-Avila, L. Yang, X. Zhang, and K. Vahala. High-Q surface-plasmon-polariton whispering-gallery microcavity. *Nature*, 457:455–458, 2009.

[3] M. A. Santiago-Cordoba, S. V. Boriskina, F. Vollmer, and M. C. Demirel. Plasmonic Nanoparticle-based Protein Detection by Optical Shift of a Resonant Microcavity. *ArXiv e-prints*, August 2011.

[4] J. D. Swaim, J. Knittel, and W. P. Bowen. Detection limits in whispering gallery biosensors with plasmonic enhancement. *Applied Physics Letters*, 99:243109, 2011.

[5] S. I. Shopova, R. Rajmangal, S. Holler, and S. Arnold. Pasmonic enhancement of a whispering-gallery-mode biosensor for single nanoparticle detection. *Applied Physics Letters*, 98:243104, 2011.

[6] J. D. Swaim, J. Knittel, and W. P. Bowen. Plasmonic enhancement of whispering gallery mode biosensors. In *Proceedings of the International Quantum Electronics Conference and Conference on Lasers and Electro-Optics Pacific Rim 2011*, page J714. Optical Society of America, 2011.

[7] N. K. Hon and A. W. Poon. Surface plasmon resonance enhanced coupling to whispering-gallery modes in optical micropillar resonators. In *Conference on Lasers and Electro-Optics/Quantum Electronics and Laser Science and Photonic Applications Systems Technologies*, page QMI2. Optical Society of America, 2006.

[8] J. Knittel, J. D. Swaim and W. P. Bowen. Whispering gallery mode biosensors with plasmonic enhancement, June 2012.

[9] F. D. Stefani, K. Vasilev, N. Bocchio, N. Stoyanova, and M. Kreiter. Surface-plasmon-mediated single-molecule fluorescence through a thin metallic film. *Physical Review Letters*, 94:023005, Jan 2005.

[10] K. Kneipp, H. Kneipp, I. Itzkan, R. R. Dasari and M. S. Feld. Ultrasensitive chemical analysis by Raman spectroscopy. *ChemInform*, 30(50):no–no, 1999.

[11] S. Nie, and S. R. Emory. Probing single molecules and single nanoparticles by surface-enhanced Raman scattering. *Science*, 275(5303):1102–1106, 1997.

[12] G. Raschke, S. Kowarik, T. Franzl, C. Sonnichsen, T. A. Klar, J. Feldmann, A. Nichtl, and K. Krzinger. Biomolecular recognition based on single gold nanoparticle light scattering. *Nano Letters*, 3(7):935–938, 2003.

[13] Y. Tanaka and K. Sasaki. Optical trapping through the localized surface-plasmon resonance of engineered gold nanoblock pairs. *Optics Express*, 19(18):17462–17468, Aug 2011.

[14] S. I. Shopova, R. Rajmangal, Y. Nishida, S. Arnold. Ultrasensitive nanoparticle detection using a portable whispering gallery mode biosensor driven by a periodically poled lithium-niobate frequency doubled distributed feedback laser. *Review Of Scientific Instruments*, 81, 2010.

[15] X. Shan, S. Wang, and N. Tao. Study of single particle charge and brownian motions with surface plasmon resonance. *Applied Physics Letters*, 97:223703, 2010.

[16] G. Kozyreff, J. Martorell. Whispering gallery microresonators for second harmonic light generation from a low number of small molecules. *Nature Communications*, Online:http://dx.doi.org/10.1038/ncomms1253, 2011.

[17] H. Li, Y. Guo,Y. Sun, K. Reddy, and X. Fan. Analysis of single nanoparticle detection by using 3-dimensionally confined optofluidic ring resonators. *Optics Express*, 18(24):25081–25088, Nov 2010.

[18] I. M. White, H. Oveys, and X. D. Fan. Liquid-core optical ring-resonator sensors. *Optics Letters*, 31:1319–1321, 2006.

[19] H. Zhu, I. M. White, J. D. Suter, P. S. Dale, and X. Fan. Analysis of biomolecule detection with optofluidic ring resonator sensors. *Optics Express*, 15:9139–9146, 2007.

[20] F. Vollmer, S. Arnold. Whispering-gallery-mode biosensing: Labelfree detection down to single molecules. *Nature Methods*, 5:591–596, 2008.

[21] J. Swaim, J. Knittel, and W. P. Bowen. Enhancing the sensitivity of whispering gallery mode biosensors using plasmons. In *Frontiers in Optics*, page FTuJ4. Optical Society of America, 2011.

[22] J. Knittel, J. Swaim, and W. Bowen. A self-referencing detection technique for whispering gallery mode biosensors. In *CLEO/Europe and EQEC 2011 Conference Digest*, page JSIV25. Optical Society of America, 2011.

[23] J. Knittel, J. D. Swaim, G. Brawley, M. A. Taylor, and W. P. Bowen. Nanoparticle detection and characterization using optical microresonators. In *Proceedings of the International Quantum Electronics Conference and Conference on Lasers and Electro-Optics Pacific Rim 2011*, page C655. Optical Society of America, 2011.

[24] M. R. Lee and P. M. Fauchet. Nanoscale microcavity sensor for single particle detection. *Opt. Lett.*, 32(22):3284–3286, Nov 2007.

[25] H. Ouyang, R. Viard, and P. M. Fauchet. Label-free optical sensing of proteins with porous silicon microcavities. In *Conference on Lasers and Electro-Optics/Quantum Electronics and Laser Science and Photonic Applications Systems Technologies*, page CTuP4. Optical Society of America, 2005.

[26] H. C. Ren, F. Vollmer, S. Arnold, and A. Libchaber. High-Q microsphere biosensor - analysis for adsorption of rodlike bacteria. *Optics Express*, 15(25):17410–17423, Dec 2007.

[27] T. Lu, T-TJ Su, K.J. Vahala, S Fraser. Split frequency sensing methods and systems., 2009.

[28] P. Zijlstra, P. M. R. Paulo, and M. Orrit. Optical detection of single non-absorbing molecules using the surface plasmon of a gold nanorod. *ArXiv e-prints*, January 2012.

[29] A. Fenner. Prostate cancer: Novel inverse sensitivity enzyme-linked crystal-growth assay to detect ultralow psa levels. *Nature Review Urology*, 2012.

[30] J. C. Knight, G. Cheung, F. Jacques, and T. A. Birks. Phase-matched excitation of whispering-gallery-mode resonances by a fiber taper. *Optics Letters*, 22(15):1129–1131, Aug 1997.

[31] P. Barclay, K. Srinivasan, and O. Painter. Nonlinear response of silicon photonic crystal microresonators excited via an integrated waveguide and fiber taper. *Optics Express*, 13(3):801–820, Feb 2005.

[32] G. Brambilla and V. Finazzi and D. Richardson. Ultra-low-loss optical fiber nanotapers. *Optics Express*, 12(10):2258–2263, May 2004.

[33] M. Cai, O. Painter, K. Vahala. Observation of critical coupling in a fiber taper to a silica-microsphere whispering-gallery mode system. *Physical review letters*, 85:74–77, 2000.

[34] C. P. Michael, M. Borselli, T. J. Johnson, C. Chrystal, and O. Painter. An optical fiber-taper probe for wafer-scale microphotonic device characterization. *Optics Express*, 15(8):4745–4752, Apr 2007.

[35] V. S. Ilchenko, X. S. Yao, and L. Maleki. Pigtailing the high-Q microsphere cavity: a simple fiber coupler for optical whispering-gallery modes. *Optics Letters*, 24(11):723–725, Jun 1999.

[36] S. Yao V. Iltchenko, L. Maleki and C. Wu. Coupling system to a microsphere cavity, 2002.

[37] M. L. Gorodetsky, and V. S. Ilchenko. High-Q optical whispering-gallery microresonators: precession approach for spherical mode analysis and emission patterns with prism couplers. *Optics Communications*, 113(13):133 – 143, 1994.

[38] A. Mazzei, S. Gtzinger, L.de, S. Menezes, V. Sandoghdar, and O. Benson. Optimization of prism coupling to high-Q modes in a microsphere resonator using a near-field probe. *Optics Communications*, 250(46):428 – 433, 2005.

[39] S. Arnold, M. Khoshsima, I. Teraoka, S. Holler, and F. Vollmer. Shift of whispering-gallery modes in microspheres by protein adsorption. *Optics Letters*, 28(4):272–274, Feb 2003.

[40] A. Rahman, R. C. Eze, and S. Kumar. Novel optical sensor based on morphology-dependent resonances for measuring thermal deformation in microelectromechanical systems devices. *Journal of Micro/Nanolithography, MEMS, and MOEMS*, 8:33071–39700, 2009.

[41] V. Michaud-Belleau, J. Roy, S. Potvin, JR. Carrier, LS. Verret, M. Charlebois, J. Genest, C. N Allen. Whispering gallery mode sensing with a dual frequency comb probe. *Optics express*, 20:3066–3075, 2012.

[42] Y. Shen, and J. T.Shen. Nanoparticle sensing using whispering-gallery-mode resonators: Plasmonic and Rayleigh scatterers. *Physical Review A*, 85:013801, Jan 2012.

[43] F. Vollmer, S. Arnold, and D. Keng. Single virus detection from the reactive shift of a whispering-gallery mode. *Proceedings of the National Academy of Sciences*, 105(52):20701–20704, 2008.

[44] Y. J. Chen, and G. M. Carter. Measurement of third order nonlinear susceptibilities by surface plasmons. *Applied Physics Letters*, 41(4):307–309, 1982.

[45] P. Pattnaik. Surface plasmon resonance applications in understanding receptor-ligand interaction. *Applied Biochemistry and Biotechnology*, 126:79–92, 2005. 10.1385/ABAB:126:2:079.

[46] A. J. Haes, andR. P. Van Duyne. A nanoscale optical biosensor: Sensitivity and selectivity of an approach based on the localized surface plasmon resonance spectroscopy of triangular silver nanoparticles. *Journal of the American Chemical Society*, 124(35):10596–10604, 2002. PMID: 12197762.

[47] M. Piliarik and J. Homola. Surface plasmon resonance sensors: approaching their limits? *Optics Express*, 17(19):16505–16517, Sep 2009.

[48] X. Shan, U. Patel, S. Wang, R. Iglesias, and N. Tao. Imaging local electrochemical current via surface plasmon resonance. *Science*, 327(5971):1363–1366, 2010.

[49] P.K. Maharana, and R. Jha. Chalcogenide prism and graphene multilayer based surface plasmon resonance affinity biosensor for high performance. *Sensors and Actuators B: Chemical*, 169(0):161 – 166, 2012.

[50] Q. Min, C. Chen, P. Berini, and R. Gordon. Long range surface plasmons on asymmetric suspended thin film structures for biosensing applications. *Optics Express*, 18(18):19009–19019, Aug 2010.

[51] F. Vollmer. Taking detection to the limit. label-free, high-sensitivity detection of biomolecules using optical resonance. *Boehringer Ingelheim Fonds Futura*, 20:6 pp, 2005.

[52] M. L. Gorodetsky, A. A. Savchenkov, V. S. Ilchenko. Ultimate Q of optical microsphere resonators. *Optics Letters*, 21:453–455, 1996.

[53] M. Soltani, S. Yegnanarayanan, A. Adibi. Ultra-high-Q planar silicon microdisk resonators for chip-scale silicon photonics. *Optical Express*, 15:4694–4704, 2007.

[54] T. J. Kippenberg, S. M. Spillane, D. K. Armani, K. J. Vahala. Ultralow-threshold microcavity Raman laser on a microelectronic chip. *Optics Letters*, 29:1224–1226, 2004.

[55] T. A. Birks, J. C. Knight, and T. E. Dimmick. High-resolution measurement of the fiber diameter variations using whispering gallery modes and no optical alighment. *IEEE Photonic Technology Lettters*, 12:182–183, 2000.

[56] G. S. Murugan, J. S. Wilkinson, and M. N. Zervas. Optical excitation and probing of whispering gallery modes in bottle microresonators: potential for all fiber add-drop filters. *Optics Letters*, 35:1893–1895, 2010.

[57] A. Ashkin and J. M. Dziedzic. Observation of optical resonances of dielectric spheres by light scattering. *Applied Optics*, 20(10):1803–1814, May 1981.

[58] P. Chylek, V. Ramaswamy, A. Ashkin, and J. M. Dziedzic. Simultaneous determination of refractive index and size of spherical dielectric particles from light scattering data. *Applied Optics*, 22(15):2302–2307, Aug 1983.

[59] A. Matsko and V. Ilchenko. Optical resonators with whispering-gallery modespart i: basics. *IEEE Journal Selected Topics in Quantum Electronics*, 12:3–14, 2006.

[60] L. Andreani, G. Panzarini, and J.-M. Gerard. Strong-coupling regime for quantum boxes in pillar microcavities:theory. *Physical Review B*, 60:1327613279, 1999.

[61] M. Gorodetsky, A. Pryamikov, and V. Ilchenko. Rayleigh scattering in high-Q microspheres. *Journal of Optical Society of America B*, 17:10511057, 2000.

[62] I. S. Grudinin, V. S. Ilchenko, and L. Maleki. Ultrahigh optical Q factors of crystalline resonators in the linear regime. *Physical Review A*, 74:063806, Dec 2006.

[63] K. J. Vahala. Optical microcavities. *Nature*, 424:839–846, 2003.

[64] D. K. Armani, T. J. Kippenberg, S. M. Spillane, and K. J. Vahala. Ultra-high-Q toroid microcavity on a chip. *Nature*, 421:925–928, 2003.

[65] A. E. Siegman. *Lasers*. University Science Books, 1986.

[66] A. L. Schawlow, and C. H. Townes. Infrared and optical masers. *Physical Review*, 112:1940–1949, 1958.

[67] C. Henry. Phase noise in semiconductor lasers. *Journal of Lightwave Technology*, 4:298–311, 1986.

[68] K. Vahala, and A. Yariv. Semiclassical theory of noise in semiconductor lasers-part li. *IEEE Journal of Quantum Electronics*, 19:1102–1109, 1983.

[69] B. Moslehi. Analysis of optical phase noise in fiber-optic systems employing a laser source with arbitrary coherence time. *Journal of Lightwave Technology*, 4:1334–1351, 1986.

[70] A. A. Michelson and E. Morley. On the relative motion of the earth and the luminiferous ether. *American Journal of Science*, 34:333–345, 1887.

[71] A. Michelson, and F. Pease. Measurement of the diameter of alpha orionis with the interferometer. *Astrophysical Journal*, 53:249–259, 1921.

[72] Y. Tian, W. Wang, N. Wu, X. Zou, W. Wang. Tapered optical fiber sensor for label-free detection of biomolecules. *Sensors*, 11:3780–3790, 2011.

[73] Gerd Keiser. *Optical Fiber Communications*. McGraw-Hill Companies, 2010.

[74] T. Kariya and H. Kurata. *Generalized Least Squares*. Wiley, 2004.

[75] M. L. Gorodetsky and V. S. Ilchenko. Optical microsphere resonators: optimal coupling to high-Q whispering-gallery modes. *Journal of Optical Society of America B*, 16(1):147–154, Jan 1999.

[76] L. Zehnder. *Zeitschrift fr Instrumentenkunde*, 11, 1891.

[77] L. Zehnder. *Zeitschrift fr Instrumentenkunde*, 12, 1892.

[78] V. Sandoghdar, F. Treussart, J. Hare, V. Lefevre-Seuin, J.-M. Raimond, and S. Haroche. Very low threshold whispering-gallery-mode microsphere laser. *Physical Review A*, 54:1777–1780, 1996.

[79] M. Cai, O. Painter, K. J. Vahala, and P. C. Sercel. Fiber-coupled microsphere laser. *Optics Letters*, 25:1430–1432, 2000.

[80] F. Lissillour, P. Feron, N. Dubreuil, P. Dupriez, M. Poulain, and G. M. Stephan. Erbium-doped microspherical lasers at 1.56 μ m. *Electronics Letters*, 36:1382–1384, 2000.

[81] A. E. Fomin, M. L. Gorodetsky, I. S. Grudinin, and V. S. Ilchenko. Nonstationary nonlinear effects in optical microspheres. *Journal of Optical Society of America B*, 22:459–465, 2005.

Appendix A

Derivation of Split Frequency Shifts Caused by Surface Inhomogeneities

Consider a microsphere system used for the sensing of a nanoparticle, as depicted below in Figure A.1. The theory for this Appendix comes from the work seen in [61]. Scattering of light off the inhomogeneity will induce a coupling between the fundamental clockwise (CW) and counter-clockwise (CCW) travelling modes, denoted by $\vec{e}_+$ and $\vec{e}_-$ respectively. To find the coupling parameter between the two modes, start with the wave equation for the electric field in the microsphere and add a perturbing permittivity to represent the inhomogeneity as shown in the following equation:

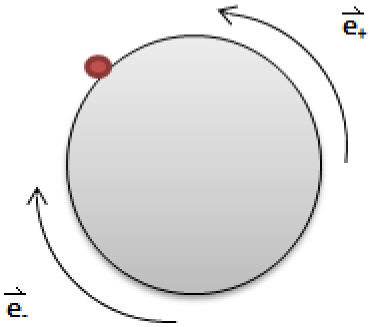

Figure A.1: Scattering off of a surface inhomogeneity.

$$\nabla^2 \vec{E}(\vec{R}, t) - \mu_0 \epsilon_0 [\epsilon_r^0(\vec{r}) + \delta\epsilon_r(\vec{r})] \frac{\partial^2}{\partial t^2} \vec{E}(\vec{r}, t) = 0. \tag{A.1}$$

Here $\vec{E}(\vec{r}, t)$ is the electric field, μ_0 and ϵ_0 are the permeability and permittivity of free space respectively, $\epsilon_r^0(\vec{r})$ is the bulk relative permittivity, and $\delta\epsilon_r(\vec{r})$ is the perturbing permittivity.

The next step is to set the solution of the resonating electric field to consist of a superposition of modes each with slowly varying amplitudes:

$$\vec{E}(\vec{r}, t) = e^{-j\omega_0 t} \sum_i A_i(t) \vec{e_i}(\vec{r}). \tag{A.2}$$

Where ω_0 represents central frequency of the resonating modes, the j index represents the different possible modes (in this case the CW and CCW modes), $A_i(t)$ is the i^{th} amplitude at time t, and $\vec{e_i}(\vec{r})$ is the i^{th} mode profile. It is also noted that the mode profiles $\vec{e_i}(\vec{r})$ satisfy the Helmholtz equation,

$$\nabla^2 \vec{e_i}(\vec{r}) + \frac{\epsilon_r^0(\vec{r})}{c^2} \omega_i^2 = 0, \tag{A.3}$$

where the speed of light, c, and the mode frequencies, ω_i, are introduced. This equation leads to the following orthogonality condition with integrals taken over all space:

$$\int \epsilon_r^0(\vec{r}) \vec{e_i}(\vec{r}) \vec{e_k}^*(\vec{r}) \, \mathrm{d}V = \delta_k^i. \tag{A.4}$$

Upon substituting Equation A.2 into Equation A.1 the following is obtained:

$$\begin{aligned} \frac{e^{-j\omega_0 t}}{c^2} [-\sum_i A_i(t) \epsilon_r^0(\vec{r}) \omega_i^2 \vec{e_i}(\vec{r}) + \sum_i A_i(t) \epsilon_r^0(\vec{r}) \omega_0^2 \vec{e_i}(\vec{r}) \quad \ldots & \\ + \sum_i A_i(t) \delta\epsilon_r(\vec{r}) \omega_0^2 \vec{e_i}(\vec{r}) + 2j\omega_0 \epsilon_r^0(\vec{r}) \sum_i \frac{\partial A_i(t)}{\partial t} \vec{e_i}(\vec{r})] &= 0. \end{aligned} \tag{A.5}$$

Note that only the first order perturbations have been considered, and because the amplitudes $A_i(t)$ are slowly varying, $\frac{\partial^2 A_i(t)}{\partial t^2}$ is negligible, as well as the product of $\delta\epsilon_r(\vec{r}) \frac{\partial A_i(t)}{\partial t}$. Next multiply Equation A.5 onto $\vec{e_k}^*(\vec{r})$ and integrate over all space while taking into account the orthogonality condition stated above. The simplified result is as follows:

$$\begin{aligned} 2j\omega_0 \frac{\partial A_k(t)}{\partial t} \int \epsilon_r^0(\vec{r})|\vec{e_k}(\vec{r})|^2 \, \mathrm{d}V & \quad ... \\ ... + \sum_i \omega_0^2 A_i(t) \int \delta\epsilon_r(\vec{r})\vec{e_i}(\vec{r})\vec{e_k}^*(\vec{r}) \, \mathrm{d}V & \quad ... \\ ... + \epsilon_r^0(\vec{r})(\omega_0^2 - \omega_k^2) A_k(t) \int \epsilon_r^0(\vec{r})|\vec{e_k}(\vec{r})|^2 \, \mathrm{d}V & = 0. \end{aligned} \tag{A.6}$$

This equation can be rewritten in the following format standard for coupled modes,

$$\frac{\partial A_k(t)}{\partial t} + j\Delta\omega A_k(t) = j\sum_k A_k(t)\beta_{ik}, \tag{A.7}$$

with

$$\beta_{ik} = \frac{\omega_0}{2} \frac{\int \delta\epsilon_r(\vec{r})\vec{e_i}(\vec{r})\vec{e_k}^*(\vec{r}) \, \mathrm{d}V}{\int \epsilon_r^0(\vec{r})|\vec{e_k}(\vec{r})|^2 \, \mathrm{d}V} \tag{A.8}$$

and

$$\Delta\omega = \frac{\omega_k^2 - \omega_0^2}{2\omega_0} \approx \omega_k - \omega_0. \tag{A.9}$$

This equation shows how the modes will couple to each other, and clearly the coupling is dependent on the perturbing permittivity, as can be seen from Equation A.8.

Equation A.7 can be expanded in terms of the modes under consideration, $\vec{e}_+$ and $\vec{e}_-$ as:

$$\frac{\partial A_+(t)}{\partial t} + j\Delta\omega A_+(t) = j[A_+(t)\beta_{++} + A_-(t)\beta_{-+}] \tag{A.10}$$

$$\frac{\partial A_-(t)}{\partial t} + j\Delta\omega A_-(t) = j[A_-(t)\beta_{--} + A_+(t)\beta_{+-}]. \tag{A.11}$$

From inspection of Equation A.8 and noting that $\vec{e}_+ = \vec{e}_-^*$ it is apparent that $\beta_{++} = \beta_{--}$ so this expression will be called α. Similarly the coupling parameter $\beta_{+-} = \beta_{-+}^*$ so β_{+-} is just written as β. Now the previous equations are rewritten using these terms:

$$\frac{\partial A_+(t)}{\partial t} + j(\Delta\omega - \alpha)A_+(t) = jA_-(t)\beta^* \tag{A.12}$$

$$\frac{\partial A_-(t)}{\partial t} + j(\Delta\omega - \alpha)A_-(t) = jA_+(t)\beta \tag{A.13}$$

.

Rewritten in matrix form these equations become:

$$\frac{\partial}{\partial t}\boldsymbol{A} = \boldsymbol{M}\boldsymbol{A}. \tag{A.14}$$

Where

$$\boldsymbol{M} = \begin{bmatrix} j(\alpha - \Delta\omega) & j\beta^* \\ j\beta & j(\alpha - \Delta\omega) \end{bmatrix}, \tag{A.15}$$

and

$$\boldsymbol{A} = \begin{bmatrix} A_+ \\ A_- \end{bmatrix}. \tag{A.16}$$

This system can be diagonalized and decoupled by choosing odd and even superpositions of CW and CCW modes, as follows:

$$\frac{\partial A_c(t)}{\partial t} + j(\Delta\omega - \alpha - |\beta|)A_c(t) = 0 \tag{A.17}$$

$$\frac{\partial A_s(t)}{\partial t} + j(\Delta\omega - \alpha + |\beta|)A_s(t) = 0 \tag{A.18}$$

where

$$A_c = \frac{1}{\sqrt{2}}A_+ + \frac{1}{\sqrt{2}}A_-, \text{and} A_s = \frac{1}{\sqrt{2}}A_+ - \frac{1}{\sqrt{2}}A_-. \tag{A.19}$$

Effectively these equations state that when there is a surface inhomogeneity the even and odd modes are both shifted together by an amount α, and also shifted relatively by an amount $|\beta|$.

Appendix B

How Temperature Change Effects Microcavity Resonant Wavelength

To consider how temperature will affect the resonant wavelength of a microcavity, first the requirements for resonance need to be laid out. The condition for resonance in an axisymmetric cavity is simply that the optical path length be equal to an integer multiple of the light wavelength. In terms of the wavelength, this condition can be expressed as:

$$\lambda_{res} = m2\pi n_s r. \tag{B.1}$$

Where λ_{res} is the resonant wavelength, m is an integer, n_s the index of refraction inside the resonator, and r is the radius of the resonator. From this equation it is apparent that the resonant wavelength directly depends upon both the index of refraction, and resonator radius. In order to determine how temperature affects the resonant wavelength the temperature effects on both the microresonator radius and index of refraction need to be considered. The change of resonant wavelength with temperature, obtained by differentiation with respect to temperature, T, is:

$$\frac{d}{dT}\lambda_{res} = \lambda_{res}\left(\frac{1}{n_s}\frac{dn_s}{dT} + \frac{1}{r}\frac{dr}{dT}\right). \tag{B.2}$$

Over a small temperature range the expression on the right is taken to be constant such that the change in the resonant wavelength is given by the simple relation:

$$\Delta\lambda_{res} = \alpha_T \Delta T, \tag{B.3}$$

Where α_T is equal to the linear rate the resonant wavelength increases with a change in temperature,

$$\alpha_T = \lambda_{res}\left(\frac{1}{n_s}\frac{dn_s}{dT} + \frac{1}{r}\frac{dr}{dT}\right). \tag{B.4}$$

Using Newton's Law of cooling, the temperature obeys the following:

$$\frac{dT}{dt} + \frac{k_{th}}{\rho C_T}(T - T_{env}) = 0. \tag{B.5}$$

Where k_{th} is the the thermal conductivity, ρ is the material density, C_T is the specific heat capacity per mass of the cavity medium, and T_{env} is the environmental temperature.

The solution to this equation in the case the cavity is cooling off takes the exponential form:

$$T(t) = T_{env} + (T_0 - T_{env})e^{-\frac{t}{\tau_T}} \tag{B.6}$$

where the time constant $\tau_T = \frac{\rho C_T}{k_{th}}$ has been introduced.

Finally, an expression for the time dependence for the resonant wavelength of a resonant cavity that is cooling off is obtained, by combining Equations B.3 and B.6, as:

$$\Delta\lambda_{res}(t) = \alpha_T(T_0 - T_{env})\left(1 - e^{-\frac{t}{\tau_T}}\right). \tag{B.7}$$